Kinetic Simulation of Rarefied and Weakly Ionized Hypersonic Flow Fields

by

Erin D. Farbar

A dissertation submitted in partial fulfillment
of the requirements for the degree of
Doctor of Philosophy
(Aerospace Engineering)
in The University of Michigan
2010

Doctoral Committee:

Professor Iain D. Boyd, Chair
Professor Alec D. Gallimore
Professor Mark J. Kushner
Professor Kenneth G. Powell

We are at the very beginning of time for the human race. It is not unreasonable that we grapple with problems. But there are tens of thousands of years in the future. Our responsibility is to do what we can, learn what we can, improve the solutions, and pass them on.

Richard Feynman, *What Do You Care What Other People Think? (1988)*

ACKNOWLEDGEMENTS

First and foremost, I must thank my advisor Professor Iain Boyd. I have conversed with many graduate students throughout my graduate career, and I must say that I invariably leave those conversations feeling very lucky that I have such an insightful, generous and knowledgeable advisor. A special thanks goes out to Professor Mark Kushner, both for teaching one of the most interesting courses I have taken during my career (EECS 517, Physical Processes in Plasmas), and for consistently making time in his busy schedule to chat about plasmas and career aspirations. I thank Professor Alec Gallimore and Professor Ken Powell, for making the time to serve on my committee. I also thank Dr. Ron Merski, the head of the Aerothermodynamics Branch at NASA Langley, and all the folks in that branch who made it possible for me to spend a summer there in 2008. Last but not least, I must express my sincere thanks to Denise Phelps, our graduate coordinator. I have not met a logistical issue yet that Denise was not willing to help me solve.

In addition to being blessed with a wonderful advisor, I feel very lucky to be a part of such a knowledgeable and selfless research group as the Nonequilibrium Gas and Plasma Dynamics *Laboratory*. Both past and present members of the group are always willing, even excited, to share their knowledge and contribute to the group dynamic. There are three people who I must acknowledge specifically. During the later portion of my stay here at Michigan, conversations (and arguments) with fellow grad student Tim Deschenes about the finer points of aerothermodynamics,

grid generation, and other miscellaneous topics were invaluable to me. During the majority of my stay, Jon Burt, a post-doc in the lab, was very generous in sharing his vast knowledge of both particle and continuum computational methods with me. Both of these people also shared their contagious enthusiasm for the field. Lastly I must thank group alumni Nick Bisek, who was a great colleague while he was here in Michigan, and continues to be a great friend.

I have met many graduate students, alumni, and partners of graduate students here in Ann Arbor whom I hope to call friends for the remainder of my life. Special thanks goes out to Pat Trizila and Eric Gustafson, the Linux gurus. I thank Allison Craddock, Sara Spangelo, Elena Spatoulas and Hyce Schumaker for the great chats, Lululemon trips, Girls on the Run events, and constant supply of dried fruit and baked goods. I am glad to have met the alumnae of the Driscoll, Dahm and Gallimore groups: Danny Micka, Adam Steinberg, Alex Schumaker, Andy Lapsa, Prashant Patel, Kristina Lemmer. These people made my time here both more enjoyable and much more interesting! I will be a Wolverines football fan for life, thanks to them.

While the people I've mentioned above played an important role in my life recently, there are a few people who have been there consistently throughout my life who I must acknowledge. Without the support of my Aunt Carol Farbar, Grandma Cora and late Grandpa George Farbar, and my "little" sister Alison, I truly would not be where I am today.

I am grateful for the financial support I received during the course of this research from the NASA Constellation University Institutes Program (CUIP grant number NCC3-989), the National Research Council of Canada Graduate Student Fellowship, and the Zonta International Organization Amelia Earhart Fellowship.

TABLE OF CONTENTS

LIST OF FIGURES

Figure

LIST OF TABLES

LIST OF APPENDICES

Appendix

LIST OF NOMENCLATURE

Physical Constants

e	Elemental charge, 1.6022×10^{-19} C
ϵ_0	Permittivity of free space, 8.85×10^{-12} $^{\mathrm{F}}/_{\mathrm{m}}$
k	Boltzmann constant, 1.3807×10^{-23} J/K
m_{e}	Electron mass, 9.11×10^{-31} kg

Acronyms

AOTV	Aero-assisted Orbital Transfer Vehicle
BQS	Boltzmann Quadratic Sheath model
CFD	Computational Fluid Dynamics
DOI	Degree of Ionization
DSMC	Direct Simulation Monte Carlo Method
FIRE	Flight Investigation of Reentry Environment
MD	Molecular Dynamics
MPI	Message Passing Interface
NASA	National Aeronautics and Space Administration
NTC	No Time Counter scheme
PIC	Particle-In-Cell
QCT	Quasi-Classical Trajectory
RAM	Radio Attentuation Measurement
TCE	Total Collision Energy model
TPS	Thermal Protection System
VFD	Vibrationally Favored Dissociation model
VHS	Variable Hard Sphere model

CHAPTER I

Introduction

Computational tools play an important role in the design of vehicles required to enter an atmosphere from space. They are used to predict the aerodynamic and heat loads that a space vehicle will experience during its flight through an atmosphere. The accurate prediction of the flight environment is necessary for the design of the vehicle, and in some cases for the design and operation of scientific instrumentation carried on board. The purpose of this thesis is to expand upon the existing body of knowledge regarding rarefied and weakly ionized flow fields, and to improve upon the tools used to simulate these flow fields in the hypersonic community. Specifically, the Direct Simulation Monte Carlo (DSMC) computational method is used, and is described in more detail in Section 2.2. While the focus of the thesis is on reentry vehicles traveling in air, portions of the work are applicable to travel in other atmospheres.

1.1 The Structure of a Hypersonic Plasma

When a vehicle is traveling through the atmosphere at very high speeds, for example those associated with lunar (11 km/s, Mach 40) or Mars (14 km/s, Mach 50) return, a strong shock is formed in front of the vehicle. Figure 1.1 shows contours

of the translational temperature distribution in the flow over a reentry capsule. The highest temperature is reached slightly downstream of the bow shock, where kinetic energy is converted into thermal and internal energy via collisions. Some of these collisions are sufficiently energetic to produce charged species, however the majority of the flow field remains neutral. A weakly ionized plasma is formed in the region between the shock front and the vehicle surface; this region is commonly referred to as the shock layer. The behavior of this plasma is coupled to the behavior of the neutral portion of the flow field, modifying its structure and contributing to the convective and radiative heat flux reaching the vehicle's surface. One of the most obvious indications of the presence of this plasma is the phenomenon commonly referred to as 'communications blackout'; the period during vehicle reentry when communication between the capsule and ground stations is lost. This phenomenon occurs because when plasma is present in sufficient densities, radio waves are attenuated and/or reflected by the plasma layer if the frequency of the signal is lower than the local plasma frequency.

In order to model a flow field where a plasma is present, many physical phenomena need to be addressed. The charges carried by ions and electrons result in Coulomb interactions occurring between those particles, the nature of which differs from interactions between neutral particles. The interaction between free electrons and the electrons in the orbitals of heavy particles during collisions are fundamentally different than those associated with neutral particle collisions, and can result in efficient vibrational and electronic mode excitation relative to that exhibited during a collision between heavy particles. The creation of charged particles via various ionization mechanisms must be addressed, as well as charge exchange reactions and recombination reactions involving charged species. Boundary conditions describing

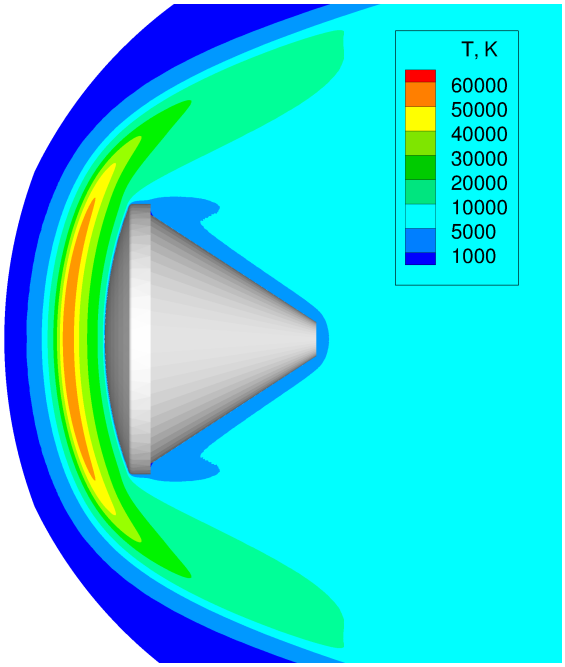

Figure 1.1: Schematic of the flow over a reentry capsule.

the behavior of charged species at the vehicle surface must be implemented, and this can involve modeling how surface charge is collected and distributed on the spacecraft structure.

The presence of charged species in the flow field necessitates the presence of a self-induced electric field, in essence, to hold the plasma together. Figure 1.2 shows the location of the plasma region with respect to the bow shock and the vehicle surface. In the bulk plasma between the shock and the vehicle surface, the so-called ambipolar electric field causes the ions and electrons to diffuse at the same average rate, and the plasma is charge quasi-neutral. The ambipolar field does not exist in the sheath region very close to the vehicle surface, nor near the interface of the bulk plasma and the ambient neutral gas upstream of the shock layer. In these regions, the ambipolar diffusion assumption is not valid and the plasma is not charge neutral. This electric field must also be accounted for in some manner in the simulation.

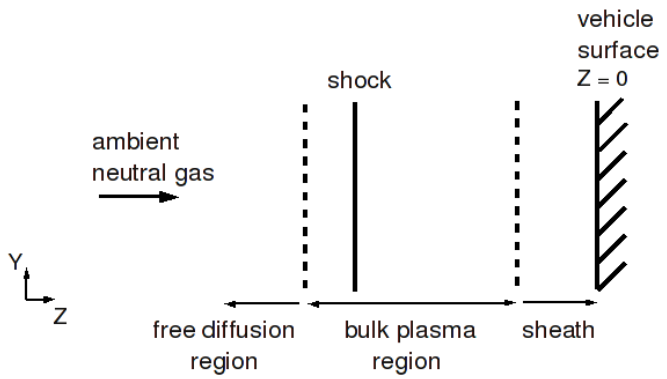

Figure 1.2: Notional schematic of the plasma generated in a hypersonic shock layer.

1.2 Objectives of this Work

Clearly, the presence of this weakly ionized plasma in a reentry flow field can significantly complicate the analysis. Efforts have been made to understand the hypersonic plasma both computationally and experimentally. Previous computational efforts will be addressed in detail in Section 2.3. One set of experimental measurements of plasma density in a hypersonic shock layer was obtained during the Radio Attenuation Measurement (RAM) experiments that took place during the late 1960s. This program involved a series of hypersonic entry flights designed to study communications blackout, and electron number density in the plasma surrounding the vehicle was measured using reflectometers and Langmuir probes[1]. However, the plasma density of $10^{15}m^{-3}$ to $10^{18}m^{-3}$ measured during these experiments was lower than the values of $10^{18}m^{-3}$ to $10^{21}m^{-3}$ expected surrounding a vehicle entering the atmosphere at a lunar or Mars return velocity. The vehicles entered at 7.8 km/s, while typical lunar and Mars return velocities are in the range of 11-14 km/s. This work focuses on modeling the denser plasmas that are created at those higher return velocities, where the plasma effects on the flow field are more pronounced. Also during the same time frame, the Flight Investigation of Reentry Environment (FIRE)

experiments were flown[2]. While these flight experiments did not provide measurements of plasma density, they did provide surface heat flux and radiative heat flux measurements at a lunar return velocity of 11.4 km/s. This data can be used to indirectly test the predictions of plasma models, and the FIRE experiment will be discussed in more detail later in the thesis. More recently in early 2006, the Stardust sample return capsule reentered the Earth's atmosphere at a velocity of 12.6 km/s, the highest energy vehicle reentry ever undertaken. During the reentry, radiation spectra were collected from a remote aircraft platform[3]. As with the heating data obtained during the reentry of the FIRE vehicles, these data can be used to indirectly test the predictions of plasma models, however they are not used here as detailed radiation modeling is not the focus of the current work. Images of each of these reentry vehicles are presented in Figure 1.3[1, 2, 4].

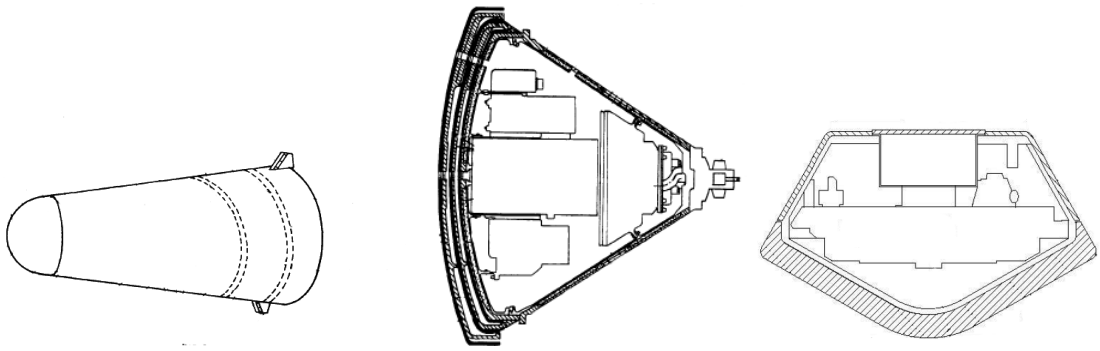

(a) RAM-C II vehicle. (b) FIRE II vehicle. (c) Stardust vehicle.

Figure 1.3: Various reentry capsules.

The sparsity of experimental measurements of reentry plasma parameters is a testament to the expense and difficulty of these types of experiments, and clearly indicates a need for an accurate modeling capability. The objective of this work is to build on the previous DSMC modeling efforts in a systematic manner, in order to produce a more rigorously tested, and well understood, set of physical models to be

used within the DSMC framework to model weakly ionized air plasma. In order to accomplish this objective, existing physical models for treating ionization phenomena using the DSMC method are implemented in the DSMC code. Next, the flow field predictions made using these baseline models for charged particle collisions and chemical reactions are compared to those made using specific collision and reaction cross section data. Limitations of the baseline ionization chemistry model are identified, and for some reaction mechanisms the use of the cross section data for future flow field modeling is recommended in lieu of the baseline model. In order to identify the limitations of the baseline electric field model, a Particle-In-Cell (PIC) module is developed and coupled to the DSMC code. The self-consistent flow field solutions produced using the coupled DSMC-PIC solver are compared to those produced using the baseline electric field model. Information from these comparisons is used to develop an improved electric field model, capable of reproducing many of the plasma phenomena not predicted by the baseline electric field model.

1.3 Outline of Thesis

The second chapter of the thesis provides an overview of the governing equations applicable to rarefied gas flow analysis and a description of the methodology and structure of the DSMC algorithm. Additionally, previously existing ionized gas models are described in this chapter. Chapter III describes the set of ionized gas models that are first implemented in this work, in order to provide a set of baseline results that will later be used to quantify model improvements. Also contained in this chapter are DSMC simulations of the FIRE II vehicle at two different altitudes in the Earth's atmosphere, performed using these baseline ionized gas models. Chapter IV discusses the use of cross section data to model particle interaction and chemical

reactions in lieu of the baseline collision and chemistry models discussed in Chapter III. Each set of cross section data is introduced in the simulation individually and the subsequent flow field predictions are compared to the baseline results presented in Chapter III. In this manner, the effect of each set of cross section data on the flow field parameters of interest is identified in a systematic fashion. Conclusions are drawn about the adequacy of the baseline collision and chemistry models.

Chapter V deals with modeling the electric field in the hypersonic plasma. A one-dimensional shock layer model is developed, and used to perform rigorous, coupled DSMC-Particle-In-Cell (PIC) simulations of the plasma. These PIC results are compared to the baseline DSMC results for both lunar and Mars return trajectories, and deficiencies of the baseline electric field model are identified. In Chapter VI, an electric field model is suggested that addresses some of the deficiencies identified by the DSMC-PIC analysis, without the need for a computationally expensive PIC calculation. Results obtained using this improved electric field model are compared directly to the rigorous DSMC-PIC results presented in the previous chapter. Finally, in Chapter VII, summaries are presented of the important results of the thesis, the specific contributions of the thesis to the state-of-the-art, and recommended future research directions.

CHAPTER II

Simulation of Rarefied and Weakly Ionized Reentry Flows

In this chapter, the governing equations used to model a gas flow from a kinetic perspective are described. A description of the Direct Simulation Monte Carlo numerical method is given next. Lastly, a review of previous research using the DSMC method to modeled ionized gases is provided.

2.1 Governing Equations

The canonical molecular (or kinetic) governing equation of dilute gas dynamics is the Boltzmann equation. In this context, the term 'dilute' identifies a gas in which the mean spacing between particles is much greater than the particle diameter. One can arrive at the Boltzmann equation through physical conservation arguments [5], or it can be obtained as a simplification of the more basic Liouville equation:

$$\frac{DF_N}{Dt} \equiv \frac{\partial F_N}{\partial t} + \sum_i c_i \frac{\partial F_N}{\partial x_i} + \sum_i a_i \frac{\partial F_N}{\partial c_i} = 0. \tag{2.1}$$

In Equation 2.1, the subscripts i refer to the three components of position, velocity and acceleration, and F_N refers to the N-particle distribution function,

$$F_N(\mathbf{X}_{\alpha\mathbf{1}},...,\mathbf{X}_{\alpha\overline{\mathbf{N}_\alpha}};\mathbf{X}_{\beta\mathbf{1}},...,\mathbf{X}_{\beta\overline{\mathbf{N}_\beta}};...,t)\mathbf{dX}_{\alpha\mathbf{1}}\mathbf{dX}_{\alpha\mathbf{2}}...\mathbf{dX}_{\alpha\overline{\mathbf{N}_\alpha}}\mathbf{dX}_{\beta\mathbf{1}}...\mathbf{dX}_{\beta\overline{\mathbf{N}_\beta}}... \quad . \tag{2.2}$$

$\mathbf{X} = (\mathbf{x}, \mathbf{c})$ is a 6 dimensional phase space variable containing the three components each of position and velocity and Greek subscripts α, β etc. refer to particle species. F_N describes the distribution of particles in an N-body system; it is the probability that at time t the coordinates and velocity of the particles have the values $\mathbf{X}_{\alpha\mathbf{1}},...,\mathbf{X}_{\alpha\overline{\mathbf{N}_\alpha}};\mathbf{X}_{\beta\mathbf{1}},...,\mathbf{X}_{\beta\overline{\mathbf{N}_\beta}};...,$ in the range $\mathbf{dX}_{\alpha\mathbf{1}}\mathbf{dX}_{\alpha\mathbf{2}}...\mathbf{dX}_{\alpha\overline{\mathbf{N}_\alpha}}\mathbf{dX}_{\beta\mathbf{1}}...\mathbf{dX}_{\beta\overline{\mathbf{N}_\beta}}...$ and that $N = \sum_\alpha \overline{N_\alpha}$ is the total number of particles in the system[6].

Equation 2.1 describes how a distribution of particles evolves in time from a given starting distribution $F_N(0)$. While it contains a complete description of a system of particles, it is far too complicated to solve for the gas flows of interest in this work.

The Boltzmann equation is obtained by repeated integration of the Liouville equation over all 6N particle coordinates $\mathbf{X} = (\mathbf{x}, \mathbf{c})$. This hierarchy of equations are known as the BBGKY equations. The last equation in the hierarchy is for the single particle distribution function, $F(\mathbf{X}_{\alpha\mathbf{1}}, t)$ and involves the two particle distribution function, $F(\mathbf{X}_{\alpha\mathbf{1}}, \mathbf{X}_{\beta\mathbf{1}}, t)$. However, it becomes a closed equation when the assumption of molecular chaos:

$$F(\mathbf{X}_{\alpha\mathbf{1}}, \mathbf{X}_{\beta\mathbf{1}}, t) = F(\mathbf{X}_{\alpha\mathbf{1}}, t)F(\mathbf{X}_{\beta\mathbf{1}}, t) \tag{2.3}$$

is made. This assumption is valid in a dilute, neutral gas where a small fraction of the occupied volume contains a particle. In this case, collisions are predominantly binary, and the probability of finding a pair of particles in a particular two-particle configuration is the product of finding the individual particles in two corresponding one particle configurations[7]. It is also valid in a dilute, ionized gas, since the single

particle behaviour in this case is predominantly influenced by long range Coulomb interactions[6]. Said another way, the distribution functions of each particle are uncorrelated. A complete derivation of the BBGKY hierarchy of equations is found in [6], Sec. 7.2 - 7.4.

At this point, the single particle distribution function $F(\mathbf{X}_{\alpha\mathbf{1}}, t)$ is redefined in the more compact notation $f_\alpha(\mathbf{x}, \mathbf{c}, t)$ using:

$$f_\alpha(\mathbf{x}, \mathbf{c}, t) = VF(\mathbf{X}_{\alpha\mathbf{1}}, t), \tag{2.4}$$

where V is the system volume. The final result of the closure of the BBGKY hierarchy using the relation stated in Equation 2.3, is the Boltzmann equation for a dilute gas, written for species α of s separate species:

$$\frac{\partial(nf_\alpha)}{\partial t} + \mathbf{c} \cdot \frac{\partial(nf_\alpha)}{\partial \mathbf{x}} + \frac{\mathbf{F}}{m} \cdot \frac{\partial(nf_\alpha)}{\partial \mathbf{c}} = \Delta[f_{\alpha,collision}]. \tag{2.5}$$

In this work we neglect the contribution of the Earth's magnetic field, which has a maximum value of 60 μT[8], and any induced magnetic field to the Lorentz force, because both are expected to be small. We also look for steady state solutions of Equation 2.5. Thus, Maxwell's equations for the evolution of the electromagnetic field reduce simply to the electrostatic Poisson equation. We write an expression for the Coulomb interaction force in terms of the average electric field produced at a point $\mathbf{x}$ by the particles for use in Equation 2.5:

$$\mathbf{F} = q_\alpha \mathbf{E} \tag{2.6}$$

$$\nabla \cdot \mathbf{E} = \frac{1}{\epsilon_o} \sum_\alpha \overline{n_\alpha} q_\alpha \int f_\alpha d\mathbf{c}. \tag{2.7}$$

In writing Equation 2.5, we have neglected all correlations between single particle distribution functions, and have expressed the macroscopic effects of charged particle Coulomb interaction as a spatially varying, average electric field. However, Coulomb interactions over length scales smaller than the Debye length are still included in the collision term on the right hand side, their interaction potentials regarded as shielded for length scales larger than the Debye length, given by

$$\lambda_D = \sqrt{\frac{\epsilon_o k T_e}{n_e e^2}}, \tag{2.8}$$

for a case where shielding results primarily from the electrons. Formally, this approximation is valid for large values of the Coulomb logarithm, which is proportional to the number of particles in a Debye sphere[9]. This assumption is applicable to the weakly ionized plasmas that will be examined in this work.

The collision term on the right hand side of Equation 2.5 describes the total rate of increase of particles of class $\mathbf{c}$ in a phase space element as a result of collisions with all other classes of particles:

$$\Delta[f_{collisions}] = \sum_{q=1}^{s} \int_{-\infty}^{+\infty} \int_{0}^{4\pi} n_\alpha n_q (f^*_\alpha f^*_{1q} - f_\alpha f_{1q}) c_{r,\alpha q} \sigma_{\alpha q} d\Omega d\mathbf{c_{1q}}. \tag{2.9}$$

In Equation 2.9 we are considering collisions of particles of species α and class $\mathbf{c}$ with all possible particles of class $\mathbf{c_1}$, such that their post-collision velocities are $\mathbf{c}^*$ and $\mathbf{c}^*_\mathbf{1}$. We are considering only non-Coulombic interactions, that is collision pairs where one of α or q species are not carrying charge. The quantity $c_{r,\alpha q}$ is the relative speed between particles and $\sigma_{\alpha q} d\Omega$ is the differential cross section of the colliding particles, a function of the relative speed and the assumed form of the interaction potential for the colliding particles [7].

The portion of the collision integral contributed by shielded Coulomb interactions is given by[9]:

$$\Delta[f_{Coulomb}] = \sum_{q=1}^{s} \int_{-\infty}^{+\infty} \int_{d\Omega} n_\alpha n_q (f_\alpha^* f_{1q}^* - f_\alpha f_{1q}) c_{r,\alpha q} \sigma_{\alpha q, Rutherford} d\Omega d\mathbf{c_{1q}}. \quad (2.10)$$

In Equation 2.10, we are considering only interactions between species α and q where both particles are carrying charge. Equations 2.9 and 2.10 differ in the limits of integration on the solid angle, Ω, and in the form of the differential cross sections. The limits of integration are now restricted to particle scattering due to impact parameters less than the Debye length. Many simplifications can be made to the form of the Coulomb collision integral as it is written here, leading to the Fokker-Planck collision term. For details, see for example Ref. [9], Sec. 7.4.

In writing both collision integrals, we have assumed that the single particle distribution function does not vary appreciably over a distance on the order of the range of the intermolecular force, nor during a collision time[5]. Additionally, we have written the collision integrals for a monotomic, non-reacting gas.

The analytical solution of Equation 2.5 is not possible for engineering flows of interest. Deterministic numerical solutions are possible, but are computationally demanding due to the high degree of dimensionality of the distribution function, f($\mathbf{x}$, $\mathbf{c}$,t). If molecules with internal structure are considered, the additional internal degrees of freedom require extended distribution functions that further complicate the solution. Equation 2.5 can be simplified considerably by assuming that the local velocity distribution function, f($\mathbf{c}$), is a slightly perturbed Maxwellian (a Chapman-Enskog velocity distribution). By taking zeroth, first and second order moments of Equation 2.5 using this assumption, one arrives at the Navier-Stokes systems

of equations. These equations are readily solvable for many problems of interest using the well-known methods of Computational Fluid Dynamics (CFD). However, in the rarefied regime where the collisionality of the gas is low, the assumption of a perturbed Maxwell velocity distribution function is not valid and the Navier-Stokes equations cannot be used to describe the flow.

2.1.1 Determining the Degree of Flow Nonequilibrium

The Navier-Stokes equations lose their validity in flow regimes where the length scale between particle collisions, the mean free path, becomes comparable to the length scales of interest in the flow field. Physically, this occurs because the assumption of a linear relationship for the transport of mass, momentum and energy no longer holds in these types of flows. One method of characterizing the applicability of the Navier-Stokes equations for a given situation is to use a non-dimensional parameter called the global Knudsen number:

$$Kn = \frac{\lambda}{L} \tag{2.11}$$

where λ is the mean free path of the flow and L is a characteristic length scale. For reentry flow analysis, the vehicle diameter or length is often used as the length scale of interest. In general, flows for which the Knudsen number is greater than 0.01 are considered to be in continuum breakdown, meaning the Navier-Stokes equations no longer hold. Additionally, one can define a local gradient length Knudsen number:

$$Kn_{gll} = \frac{\lambda}{Q}\frac{dQ}{d\mathbf{x}} \tag{2.12}$$

where Q is any local, macroscopic flow field variable of interest. The degree of continuum breakdown given by this expression is determined locally and will be high

in regions with large flow field gradients. Thus, a flow could have a global Kn<0.01, but still contain regions where the continuum assumption breaks down, and the Navier-Stokes equations are not valid.

2.2 The Direct Simulation Monte Carlo Method (DSMC)

The DSMC computational technique is used in many applications ranging from the simulation of micro-electromechanical devices (MEMs), to the simulation of reentry flow fields. It has been shown that flow field predictions produced using the DSMC technique approach solutions of the Boltzmann equation in the limit of an infinite number of simulated particles[10].

In this work, the DSMC method is used to simulate solutions to the Boltzmann equation for rarefied reentry flows in which the Navier-Stokes equations are not valid. Specifically, the code MONACO[11] is used, which was developed at the University of Michigan. The DSMC technique was first developed by Graeme Bird in the early 1960s, and a complete description of the method can be found in Ref. [7]. What follows here are the details required to discuss the treatment of ionized particles using the technique.

The fundamental assumption of the DSMC technique is that the movement and collision phases of particle behavior can be decoupled. This assumption immediately restricts the computational time step to a value less than the mean collision time everywhere in the flow field. The method requires the domain to be discretized using a computational mesh, both for selection of collision pairs and for sampling of macroscopic properties. In this work, the same mesh is used for both purposes, although this does not have to be the case. The domain is populated with simulator particles, each of which represents a large number of real particles. Events such

as collisions and chemical reactions are computed in a probabilistic, rather than deterministic manner. These properties mean that macroscopic quantities computed using the DSMC technique will necessarily contain a certain amount of statistical uncertainty.

The basic structure of the DSMC algorithm is as follows. In each computational cell, particles are chosen to collide in such a way as to reproduce the required macroscopic collision rate. The relative location of particles in the cell is not considered when selecting collision pairs. This fact restricts the size of a computational cell; it must be smaller than the local average mean free path of the flow field. Each of the colliding pairs can then chemically react or exchange internal energy. All of the colliding pairs then exchange energy elastically. Following the collision routines, each particle is moved throughout the domain for the duration of a single time step. Particles are introduced at the inflow boundaries, removed at outflow boundaries, and reflected from surfaces. If a steady state has been reached in the simulation, as indicated by constancy of particle number and total energy in the domain, the macroscopic flow variables are sampled in each cell. At this point the algorithm is repeated until a sufficient number of samples has been collected.

In this work, Bird's No Time Counter (NTC) method is used to select colliding pairs [7]. At each time step and in each computational cell, the number of particle pairs to be tested for collisions is calculated as follows:

$$N_{collide} = \frac{1}{2} n \overline{N} \left(\sigma_T c_r\right)_{max} \Delta t \tag{2.13}$$

where n is the number density of gas particles in the cell, $\overline{N}$ is the average number of simulator particles in the cell, Δt is the simulation time step, c_r is the relative velocity of a colliding pair of particles, and σ_T is the total collision cross section of

the colliding pair. The value of $(\sigma_T c_r)_{max}$ is stored on a per cell basis. Each of these $N_{collide}$ pairs are then selected to collide if the probability given by

$$P_{collide} = \frac{(\sigma_T c_r)}{(\sigma_T c_r)_{max}} \tag{2.14}$$

is greater than a randomly selected number. In neutral particle DSMC, σ_T is usually calculated using the phenomenological Variable Hard Sphere (VHS) model[7]. In order to reproduce the observed temperature dependence of neutral gases of various species, the particle diameter and thus the collision cross section is assumed to vary with the relative velocity of the colliding species as follows:

$$\sigma_{VHS} = \sigma_{ref} \left(\frac{c_r}{c_{r,ref}} \right)^{-2\omega}. \tag{2.15}$$

The exponent, ω, is obtained by fitting experimentally measured viscosity data to the following temperature dependent form:

$$\mu = \mu_{ref} \left(\frac{T}{T_{ref}} \right)^{\omega+0.5}. \tag{2.16}$$

The relationship between the reference parameters μ_{ref}, σ_{ref}, T_{ref}, ω and $c_{r,ref}$ is given in more detail in [7]. The intermolecular potential described by the VHS model is of the power law form

$$F \sim \frac{1}{r^{\frac{2+\omega}{\omega}}}, \tag{2.17}$$

where only the repulsive portion of the potential is modeled. When particles collide, their post-collision velocities are determined by enforcing conservation of momentum and energy, and their scattering angles are randomly chosen from within the unit sphere. This isotropic scattering angle has proved sufficiently accurate for high speed

flows. Other molecular models exist to model scattering angle dependence during collisions, for example the Variable Soft Sphere model[7].

Once collision partners have been selected using the NTC scheme with the VHS model, they are tested for the occurrence of chemical reactions. Chemical rate information in an Arrhenius form with threshold energy E_a:

$$\kappa = aT^b e^{\left(-\frac{E_a}{kT}\right)} \tag{2.18}$$

is used to determine the reaction probability using the phenomenological Total Collisional Energy (TCE) model[7]:

$$P_{TCE} = A\frac{\left(E_{tot} - E_a\right)^{b+\zeta+0.5}}{E_{tot}^{\zeta+1-\omega}}. \tag{2.19}$$

In the last equation, E_{tot} is the total collision energy including translational energy and the internal energy of all modes, A is dependent on both the constants in Equation 2.18 and molecular constants, and ζ is the average number of internal degrees of freedom of the colliding particles. The dissociation of molecular nitrogen and oxygen can be modeled using the Vibrationally Favored Dissociation (VFD) chemistry model, which involves modifying Equation 2.19 to allow for preferential dissociation from the higher vibrational levels[12]. Collision pairs that do not react are tested for internal energy exchange using the phenomenological schemes of [13] for vibrational energy exchange and [14] for rotational energy exchange. Following selection for internal energy exchange, the energy of the particle pair is redistributed using the phenomenological Borgnakke-Larsen model[15]. The excitation of the electronic mode of atoms and molecules is not modeled explicitly. It is assumed that the transfer of energy into the electronic mode from the translational and internal modes of the gas does not play a large role in determining the aerothermal character of the

flow field for the range of collision energies investigated in this thesis.

For the simulation results presented in this work, neutral particles accommodate fully to the specified surface temperature, and diffusely reflect from surfaces. Complete details of the DSMC method are found in [7] and the previously stated references. Additionally, a review of code validation for the DSMC technique is found in [16].

2.3 Overview of Existing Ionized Gas Models

During the late 1980s and early 1990s, interest in aero-braking concepts such as the Aeroassisted Orbital Transfer Vehicle (AOTV) sparked research into computational techniques for partially ionized rarefied flows. The AOTV was a hypothetical vehicle that would return to the Earth from Mars and use one or more passes through the rarefied portion of the Earth's atmosphere to decelerate and eventually place the vehicle into a target Earth orbit. In the present day, the design of the Orion crew capsule as a Space Shuttle replacement, as well as sample return missions from Mars and elsewhere, has generated renewed interest in this area. The details of the physical models that were developed previously to model weakly ionized plasmas using the DSMC technique are discussed here.

2.3.1 Collisions

This section describes the modeling of interactions between particles in a single computational cell.

There are five classes of collisions involving charged particles: electrons with neutrals, ions with neutrals, electrons with ions, ions with ions, and electrons with electrons. The interactions of the latter three classes obey the Coulomb force law

$$F = \frac{1}{4\pi\epsilon_o}\frac{q_1 q_2}{r^2}. \tag{2.20}$$

The interaction of ions or electrons with neutrals is a function of a higher power of r, the distance between the particles, due to the polarization of the neutral particle as the charged particle approaches [9].

Bird[17] and Taylor et al.[18] used the VHS model to describe the first four classes of collisions, by setting the diameter of the heavy ions equal to the diameter of their neutral counterparts, and setting the reference diameter of electrons equal to $1 \times 10^{-10}m$, orders of magnitude larger than the classical value of $6 \times 10^{-15}m$. The latter choice was somewhat arbitrary, although Bird does mention that the electron diameter was varied in his simulations by a factor of three with no significant effect on the flow field parameters. Neither researcher modeled electron-electron collisions.

In the DSMC computations of the flow field around the Stardust reentry capsule performed by Ozawa et al.[19], electron-neutral scattering cross sections from the literature were implemented by fitting the cross section data to the VHS form. Unfortunately, the effects of these modifications on the flow field parameters of interest were not quantified for that case.

The only attempt to model Coulomb interactions in a DSMC computation was made by Gallis et al.[20] using the 'Collision Field' method of Jones et al.[21]. This method has the property that the number of computations required to evaluate the Coulomb interactions in a given cell scales proportionally to the number of simulator particles, making it much more computationally efficient than other Coulomb collision algorithms that typically scale with the square of the number of particles. Here, again, the effect of the more physical collision model on flow field parameters was not quantified for the hypersonic, helium flow fields that were simulated in the

work.

2.3.2 Chemistry

In order to model chemical reactions involving charged species, a standard chemical reaction set for air has been adopted in the reentry simulation community for the majority of the reaction mechanisms. It is an assembly of the partial sets given in Refs. [22] and [23], both of which are a result of a literature review of available experimental rate measurements and quasi-classical trajectory calculations. These rates have been used as inputs to the phenomenological TCE chemistry model to produce energy dependent steric factors for each reaction, in the same manner as they are applied to reactions involving neutral species.

The electron impact ionization of neutral oxygen and nitrogen atoms

$$N + e \rightarrow N^+ + e + e \tag{2.21}$$

$$O + e \rightarrow O^+ + e + e \tag{2.22}$$

is one mechanism that has been modeled differently than the others, likely predominantly because the rates specified for this reaction for use with the CFD method are incompatible with the mathematical limitations of the TCE model. In their model of the Stardust reentry flow field, Boyd et al.[4, 24] used the rates of Wilson[25] with the TCE model to simulate these reactions. The rates due to Wilson were obtained for the ionization of atoms in the first excited electronic state. In a model of the same flow field, Ozawa et al. [26] instead used a curve fit with modified parameters b and E_a in Equation 2.18 to cast the rates for the electron impact ionization reactions from Ref. [22] in a form compatible with the TCE model. However, when using the TCE model, the activation energy must be equal to the energy removed during a

reaction, and this condition was not enforced in their approach.

Carlson and Hassan[27] used a two step ionization model to simulate the electron impact ionization reactions in a flow field representing a 10 km/s shock at an altitude of 65 km in the Earth's atmosphere. The fundamental assumption of their model was that the atoms are excited to the first electronic level and then ionized in a chain process. Upon a collision of an electron with a nitrogen or oxygen atom, the cross sections due to Stone and Zipf[28, 29] were used to form an excitation probability

$$P_{excite} = \frac{\sigma_{excite}}{\sigma_{VHS}} \tag{2.23}$$

to determine if the electronic state of the atom was excited. If excitation was found to occur, the average radiative lifetime of the excited state was compared to the average collision rate of atoms at that point in the flow. If the radiative lifetime was less than the collision time, the atom was assumed to have radiated to the ground electronic state and the ionization process was bypassed. Otherwise, for ionization from the excited state, the quantum defect method[30] and the Lotz[31] cross sections were used. The physical ionization mechanism simulated by Carlson and Hassan's model is the same as that simulated by Boyd et al., however the method in which it was implemented in the calculation differed. Unfortunately, due to the limited computer resources available at the time those simulations were carried out, there is significant scatter in the numerical results and the results of the study were not conclusive.

2.3.3 Electric field

Several different researchers have modeled the electric field structure in a hypersonic shock layer in the past, however, none have done so in a manner that was truly self-consistent.

The first such calculation was by Bird[32]. In his work, the electrons were moved through the grid with the ions that they were created with. No explicit electric field calculation was made, so the ions and electrons were not accelerated. The simulation time step was that of the heavy particles. Later, Bird modified this method[33] to include a calculation of the ambipolar electric field using a form of the equation originally due to Langmuir and Tonks[34]:

$$E_{ambipolar} = -\frac{kT_e}{e}\frac{d\left[ln(n_e)\right]}{dx}. \tag{2.24}$$

In Equation 2.24, T_e and n_e are the average electron translational temperature and density, macroscopic quantities derived from the DSMC solution. This equation can be derived from the macroscopic equation of momentum conservation for the electron species using the assumption of negligible inertial effects, negligible friction due to collisions, zero magnetic field and constant translational temperature. In his work, Bird calculated E_a using the results from a previously converged calculation. He then re-converged the DSMC calculation, applying the prescribed acceleration to the charged particles at each time step due to E_a. The field E_a was calculated from the re-converged DSMC solution, and the entire process repeated until there was no change in the resulting flow field parameters. The movement of the electrons was still tied to that of the ions in this method. The limitations of this approach are threefold: the assumption of isothermal electrons may not be justified, the use of macroscopic quantities T_e and n_e in a kinetic, nonequilibrium flow solution is questionable, and the assumption of charge neutrality and ambipolar diffusion is not applicable everywhere in the shock layer (see Figure 1.2).

In work by Gallis and Harvey[35], the electrons and ions were again moved together, and the electric field was calculated in a similar manner to Equation 2.24.

Here, however, the assumption of isothermal electrons was not made

$$E_{ambipolar} = -\frac{kT_e}{e}\frac{d\left[ln(p_e)\right]}{dx}, \tag{2.25}$$

and the gradient of the electron pressure was instead used to calculate the ambipolar electric field. Gallis and Harvey used a simulation time step corresponding to the cell crossing time of the heavy particles, and accelerated the heavy particles according to the field E_a. They then computed the average ion velocity in a given cell, and adjusted the average electron velocity in the same cell to match. In this way, the electron energies were affected by the electric field in an average sense. Other than the allowance for a variable electron translational temperature, this method suffers from the same limitations as that presented by Bird.

Carlson, Hassan and Taylor[18, 27] devised a method in which assumptions of zero net current and charge neutrality were used to calculate the electric field without the use of any macroscopic quantities. They wrote down Newton's law for a charged particle of species s moving under the influence of an electric field:

$$m_s\frac{d\mathbf{v}}{dt} = q_s\mathbf{E}, \tag{2.26}$$

and thus the expressions for average electron and ion velocity by summing over individual particles:

$$\overline{\mathbf{v_e}} = \frac{\sum \mathbf{v_{e,o}}}{N_e} - \frac{e\overline{\mathbf{E}}\Delta t}{2m_e} \tag{2.27}$$

$$\overline{\mathbf{v_i}} = \frac{\sum \mathbf{v_{i,o}}}{N_i} + \frac{e\overline{\mathbf{E}}\Delta t}{2m_i}. \tag{2.28}$$

In the previous equation, $\overline{\mathbf{E}}$ is the average electric field over a simulation time step Δt, N is the number of simulator particles, $\mathbf{v_o}$ is a velocity vector at the start of

a simulation iteration, and the subscripts e and i refer to electron and ion species, respectively. By enforcing charge neutrality, $N_e = N_i$, they then solved for the ambipolar electric field, $\mathbf{E}$, required to make the average ion and electron velocities equal, $\overline{\mathbf{v_e}} = \overline{\mathbf{v_i}}$, while enforcing the assumption of zero net current:

$$\frac{e\overline{\mathbf{E}}\Delta t}{2} = \frac{(\sum \mathbf{v_{e,o}} - \sum \mathbf{v_{i,o}})}{N_e \left(\sum \frac{1}{m_i} - \sum \frac{1}{m_e}\right)}. \tag{2.29}$$

The electric field given by Equation 2.29 was used to accelerate the charged particles during the move portion of the DSMC algorithm. Additionally, a simple model of the particle acceleration in the plasma sheath at the vehicle surface was implemented. The electrons were reflected specularly from the vehicle surface to simulate their reflection in the strong negative potential gradient that would exist in the plasma sheath. An additional energy increment, $e\phi$, was added to the surface heat transfer measurement for each ion impacting the surface. The expected potential drop across the sheath, ϕ, was calculated from one-dimensional collisionless sheath theory. While this method of accounting for the self-induced electric field removes the first two deficiencies associated with Bird's methods, the third deficiency remains: the assumption of charge neutrality is not applicable everywhere in shock layer, and the assumption of zero net current is not justified.

Boyd[36] developed a model for the electric field of a weakly ionized plasma that is similar to the first model of Bird. The model was first implemented in a simulation of the plasma flow through an arcjet type thruster. Each electron is moved with the velocity of an ion throughout the domain, and the charged particles do not receive any velocity increment due to their response to an electric field. However, in this model, the average ion velocity of the cell in which the electron is located is used to move the electron particle, and it is not associated with a specific ion particle. This

model maintains charge neutrality in an approximate sense, and results in lower computational overhead than the first model proposed by Bird. The model also suffers from all of the limitations of the first Bird model.

In order to calculate the self-induced electric field without any assumption of charge neutrality, zero net current, or ambipolar diffusion, the electrostatic Poisson equation must be solved. This was carried out for very rarefied flows surrounding spacecraft in low Earth orbit by two groups of researchers[37, 38]. While interesting, the preliminary results presented by these researchers in the cited references are for flow fields of significantly different structure than the shock layers being considered in this work. Gallis et al.[20] presented preliminary results in which they solved the electrostatic Poisson equation in conjunction with the DSMC method for a hypersonic helium flow field. Unfortunately, the results presented in this work were sparse, the physical processes associated with reacting air were not included in the analysis, and a systematic study of the effect of rigorously including the electric field in the computation on the flow field parameters was not presented.

CHAPTER III

Baseline Ionized Gas Models

This chapter describes the baseline physical models that are implemented in MONACO to simulate weakly ionized flow fields. These models existed in the literature when this work began. Results from simulations of the FIRE II 85 km and 76 km flight conditions using these models, and comparisons to results obtained without the inclusion of ionization physics, are presented here. In the subsequent chapters, the validity of these models is assessed and improvements made.

3.1 The FIRE Flight Experiment

Project FIRE was an Apollo-era flight experiment to measure the radiative and convective heating during atmospheric entry at lunar return speeds[2]. An image of the second vehicle in the campaign, FIRE II, was given in Figure 1.3(b) of Section 1.2. The geometry and dimensions of the outer mold line of the vehicle are shown in Figure 3.1. The fore body of the FIRE II reentry vehicle consisted of three phenolic-asbestos heat shields sandwiched between beryllium calorimeters. The first two heat shield and calorimeter packages were designed to be ejected after the onset of melting, yielded heating data free of the effects of ablation and three separate data gathering periods. Calorimeter plugs and radiometers were located at various positions on the

heat shields[2]. Both of the flight conditions examined in this study occurred during the first data collection period.

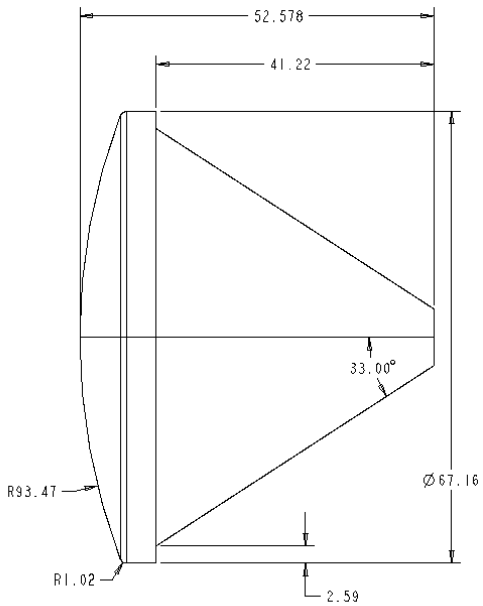

Figure 3.1: Geometry of the FIRE II reentry vehicle. Dimensions are in cm.

3.2 Collision Modeling

The baseline charged particle collision model implemented in MONACO is the one originally published by Bird[17], in which all particle interactions are treated using the VHS collision model. The reference diameters of the heavy ions N_2^+, O_2^+, NO^+, N^+ and O^+ are set equal to the diameters of their neutral particle counterparts, and the reference diameter of the electrons is set to $d_e = 1 \times 10^{-10} m$. This value of the electron reference diameter is much larger than the classical value of $6 \times 10^{-15} m$, and is used to produce electron collision cross sections of the required magnitude within the mathematical framework of the VHS collision model. A complete list of the VHS reference diameters for all species and the parameters T_{ref} and ω is given in Table A.1.

3.3 Chemistry Modeling

The baseline charged particle chemistry model implemented in MONACO is to treat the reactions involving charged particles using the TCE chemistry model, as previous researchers have done. The reaction rate coefficients used as inputs to the TCE model for the baseline FIRE II studies are given in Tables A.2 and A.3. These rates are compiled using References [22], [23], [25] and [39]. Additionally, the Vibrationally Favored Dissociation (VFD) chemistry model[12] is used to model the preferential dissociation of N_2 and O_2 molecules from higher vibrational states. The reaction probability for those reactions is given as follows:

$$P_{VFD} = A\frac{\left(E_{tot} - E_a\right)^{b+\zeta+0.5}}{E_{tot}^{\zeta+1-\omega}}\left(E_{vib}\right)^{\phi}, \tag{3.1}$$

where the parameter ϕ that operates on the vibrational energy of the colliding particles is set to 2.0 for the dissociation of N_2 and 0.5 for the dissociation of O_2.

Noticeably absent from the list of ionization mechanisms in Table A.3 is the electron impact ionization of N_2 to form N_2^+, and mechanisms involving the production of doubly ionized particles. A conservative estimate of the expected collision energy between a heavy particle and an electron at a Mars return velocity of 14 km/s is given as follows. Consider the collision of a heavy particle traveling at the free stream velocity with an electron traveling in the opposite direction that possesses a velocity from the tail of the velocity distribution function, $u_e = 3\sqrt{kT_e/m_e}$ at $T_e = 30\,000$ K (the validity of this value for T_e will become apparent later in this Chapter). This calculation yields a collision energy for the heavy particle - electron system of approximately 12 eV. The first ionization energy of N_2 is 15.6 eV[5]. Since, at this high reentry velocity, the majority of the nitrogen in the flow will be dissociated

downstream of the shock wave where the bulk of the electron particles are located, the ionization of N_2 by electron impact is not expected to occur with any significant frequency. The second ionization energy of nitrogen is 29.6 eV, and that of oxygen is 35 eV[40], well above the expected collision energy of these species with electron particles. Thus, the production of doubly ionized particles is not considered in this work.

3.4 Electric Field Modeling

The baseline electric field model implemented in MONACO is that of Boyd[36]. Specifically, the mass-averaged ion velocity components are calculated in each computational cell, and the electron particles are moved with those velocities during the movement portion of the DSMC algorithm. The electrons retain their individual velocity components, however, and in this way they are constrained in an average sense to move with the ions and charge neutrality is approximately preserved in the entire simulation domain. Neither the electrons nor ions 'feel' the electric field, in that their velocity components are not adjusted to account for an electric field as one is not computed.

The averaging of an ion velocity component in a computational cell is accomplished using a sub-relaxation technique[41] and proceeds as follows:

$$\overline{u_j} = (1-\theta)\,\overline{u_{j-1}} + \theta u_j, \tag{3.2}$$

where $\overline{u_{j-1}}$ is the average velocity component of the ions at the previous time step in a given cell, and the result $\overline{u_j}$ is the average ion velocity at the current time step that is used to move the electrons through the cell. The sub-relaxation parameter θ is a constant less than one, and is used to increase the sample size for the average

$\overline{u_j}$. An instantaneous ion velocity component in a cell at the current time step, u_j, is calculated by averaging over s ion species

$$u_j = \sum_{k=1}^{s} \left(Y_k \frac{1}{N_k} \sum_{l=1}^{N_k} u_{l,k} \right), \tag{3.3}$$

where Y_k represents the ion mass fraction of species k in the cell, N_k is the number of particles of species k in the cell, and $u_{l,k}$ are each of those particles' individual velocities. This technique significantly reduces the statistical scatter in the average velocity components used to move the electrons, however the process introduces a lag in the ion velocity value relative to the instantaneous value. This lag is removed periodically using the following correction[41] to produce an updated average velocity $\overline{u_j'}$ by neglecting the information collected prior to time step i as follows

$$\overline{u_j'} = \overline{u_j} + \frac{(1-\theta)^{j-i}}{1-(1-\theta)^{j-i}} \left(\overline{u_j} - \overline{u_i} \right). \tag{3.4}$$

Thus, every $(j-i)$ time steps, the velocity information from time steps prior to time step i is removed from the running average.

3.4.1 Parameter sensitivity study

In order to select the optimal parameters θ and $(j-i)$ for use in these simulations, a sensitivity study is performed in which the parameters are varied and the degree of non-neutrality of the resulting flow field solution is used to determine the merit of the particular parameter combination. The flow field used for this study is the FIRE II, 85 km case. Figure 3.2 gives a selection of results from this study, showing the number density of ions and electrons along the stagnation streamline for various parameter combinations. The ion number density is only shown for one set of parameters as the result was nearly identical for all simulations considered. While all sets of parameters

perform well in the central region of the flow, the performance of the baseline electric field model degrades near the vehicle surface at z=0 m, and near the free stream boundary z=0.2 m. This occurs because the number of ion particles decreases in both of these regions, leading to a poor approximation of the average ion velocity. The sharp peak at z=-0.14 m in the electron density obtained using the parameters $\theta = 0.0001$ and $(j - i) = 10000$ results from electrons being transported upstream of the shock region and becoming 'stuck' there as the average ion velocity goes to zero. Based on the results of the sensitivity study, the parameters $\theta = 0.001$ and $(j - i) = 10000$ are used throughout the remainder of this thesis. These parameters provide the best overall accuracy in both the near wall and free stream boundary regions.

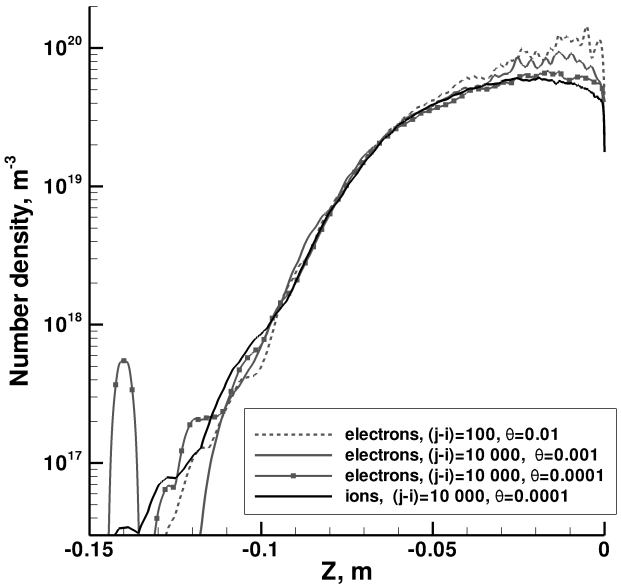

Figure 3.2: Effect of varying sub-relaxation parameters θ and $(j - i)$ on the degree of non-neutrality in the FIRE II 85 km flow field solution.

3.5 Other Models

The small mass and correspondingly high thermal velocities of the electrons result in relatively high electron-heavy particle collision rates. However, since the electrons are *moving* with the slower heavy particles, the global simulation time step is dictated by the velocity of the heavy particles, and the collision algorithm is sub-cycled within each simulation time step. This allows the high electron collision rate to be accommodated in the DSMC algorithm, while avoiding the use of unnecessarily small simulation time steps.

Collisions of electrons with other electrons are not modeled in this work because they serve only to equilibrate the electron energy distribution function, which is assumed to be nearly Maxwellian due to the high rate of collisions of electrons with other particles. The validity of this assumption is demonstrated in Section 6.1 of this thesis.

The interaction of particles with the vehicle surface is managed by allowing heavy particles to reflect diffusely from the surface, after thermally accommodating to the specified wall temperature. The surface is assumed to be fully catalytic to ion recombination, and not catalytic to recombination of neutrals. Electrons that reach the surface are removed from the simulation, as they are assumed to recombine with the ions at the surface.

The molecular ions are assumed to exchange rotational and vibrational energy during collisions in the same manner as their neutral counterparts. In general, excitation of the internal energy modes of some molecular species can occur with a high degree of efficiency during collisions with electrons. For example, the resonant vibrational excitation of N_2 proceeds via a temporary N_2^- state for collision energies

in the 2-3 eV range[42]. This process transfers vibrational energy to the nitrogen molecule very effectively, resulting in a short vibrational relaxation time that has been computed by Lee[43] for the temperatures of interest in this work. Lee's data is used in lieu of the standard vibrational relaxation model for e-N_2 collisions in an additional computation of the FIRE II 85 km fore body case that will be presented in Section 3.6.1. There was no appreciable change noted in the flow field parameters for this case, likely due to the low concentration of electrons in the flow field. Thus, the modeling of the resonant translational-vibrational energy exchange of the e-N_2 system is not pursued further in this work. Such a resonant mechanism is not known to exist for the e-O_2 system.

Line-of-sight radiation results contained in this work are obtained by post-processing the converged flow field results using the NEQAIR code[44] developed by NASA.

3.6 FIRE II Simulations

A number of simulations of the flow field around the FIRE II vehicle during its reentry into the Earth's atmosphere are completed using the ionization models described above. All are run on the University of Michigan 'nyx' supercomputing cluster with AMD Opteron processors unless otherwise stated. The simulations run with the ionized gas models are about seven times slower than those run with neutral particles. The slowdown is due primarily to the sub-cycling routine used to account for rapid electron collisions, but is also affected by the use of additional species and more than twice the number of chemical reactions in the simulations with charged particles. In each simulation, the computational grid is refined to the local mean free path in all directions except where noted otherwise, and the simulation time step is less than the local mean collision time. The computational

grids are all composed of quadrilateral cells, or hexahedral cells in three dimensions. In addition to simulations using the 11 species ionized gas model, 5 species neutral gas simulations are completed in some cases. Doing so clarifies the effects of accounting for plasma formation on the flow field structure.

3.6.1 Forebody at 85 km

The free stream conditions for this flight condition are given in Table 3.1[2], where the free stream Knudsen number is based on the capsule forebody diameter. At this very rarefied flight condition, the entire flow field is in continuum breakdown. The simulation is of the forebody region of the flow field, and the grid is refined to the local mean free path in the axial direction only. This is permissible because the flow field gradients are predominantly in the axial direction due to the nature of the capsule geometry. The first row of computational cells along the axis of symmetry is stretched in the radial direction to twice the height of the subsequent cells since by definition, the radial flow field gradients are zero along the symmetry axis. This increases the number of particles in the cells along the axis and reduces statistical scatter in the results. Radial weight bands are used to decrease the number of simulator particles in the radial direction, since in an axisymmetric simulation the cell volume scales proportionally to the distance of the cell center from the symmetry axis. Sampling is begun after 60 000 time steps, and 50 000 sampling iterations are performed. The simulation has 19 million particles, runs on 20 processors, and requires about 48 wall hours to complete. There is a maximum of 10 electron particles in the cells along the axis. Due to the low degree of ionization in the flow field, this means that there are hundreds of neutral particles in those cells.

Contours of translational temperature are shown in Fig. 3.3(a), in order to give a

Table 3.1: Flow conditions for Project FIRE II at 85 km.

Free Stream Condition	Value
Altitude	84.6 km
ρ_∞	9.15×10^{-6}kg/m^3
U_∞	11.37 km/s
M_∞	39
T_∞	212 K
T_{wall}	460 K
Kn_∞	0.01

general impression of the flow field structure at this altitude. The peak temperature of just over 50 000 K occurs slightly downstream of the bow shock at approximately z=-0.1 m. Figure 3.3(b) shows the temperatures of the rotational, vibrational, translational and electron translational modes along the stagnation streamline obtained using both the 5 species and 11 species chemistry models. The addition of ionization chemistry to the model narrows the translational temperature profile, and the rotational temperature is decreased significantly in the 11 species case. This is likely due to an increased level of dissociation in the 11 species simulation. These trends were also observed in previously performed computations of this FIRE II flight condition reported in Ref. [45]. Figures 3.4(a) and 3.4(b) give the mole fractions of the neutral and charged species along the stagnation line. The electron mole fraction peaks at a value of approximately 0.02, again in agreement with the results presented in Ref. [45]. Figure 3.5(a) shows the number density of electrons, total number density of ions, and the degree of ionization along the stagnation line. Charge neutrality is reasonably enforced in the flow field using the baseline electric field model, and the degree of ionization (DOI) peaks at approximately 2%.

Figure 3.5(b) shows the heat flux profiles along the vehicle surface for both the 11

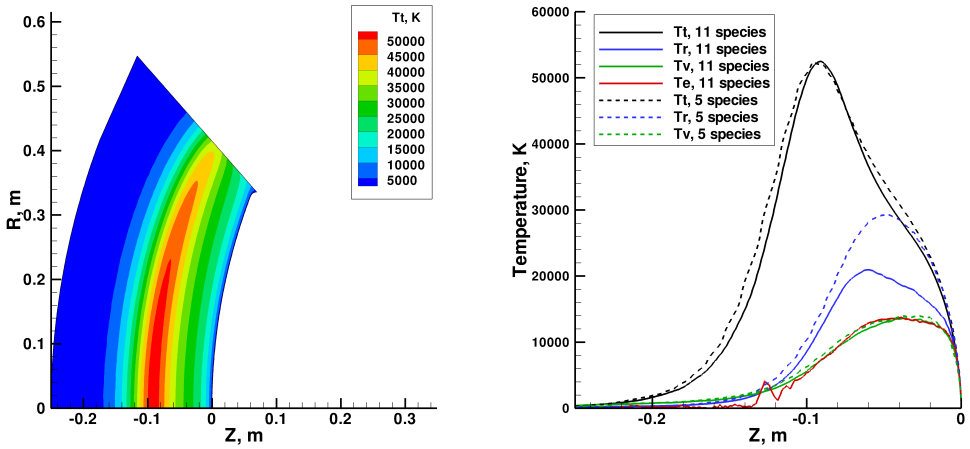

(a) Contours of translational temperature for the 11 species case.

(b) Temperatures along the stagnation streamline for both the 11 species and 5 species cases.

Figure 3.3: Flow field temperatures from the FIRE II 85 km fore body simulation.

species and 5 species simulations, along with the calorimeter results from the FIRE II experiment. The reported error on the measured data was ±5%[2]. The simulation incorporating ionization effects yields a slightly lower convective heat flux than the neutral gas simulation. It is likely that this is due to an increased amount of nitrogen dissociation, due to the inclusion of the mechanism of electron impact dissociation, Reaction 1e in Table A.2. This rate is two orders of magnitude higher than the rates for dissociation of nitrogen due to collisions with atoms and molecules. This hypothesis is supported by the profiles of mole fraction shown along the stagnation streamline in Fig. 3.4(a), where it is evident that there is a larger fraction of atomic nitrogen and a smaller fraction of molecular nitrogen downstream of the shock in the 11 species simulation. It should be noted that the results of Taylor et al.[45], which are also shown in Figure 3.5(b), indicated that the addition of ionization chemistry resulted in a net increase in the heat flux to the vehicle surface. However, it is likely that the finite catalycity of the wall to oxygen atoms in that simulation negated the

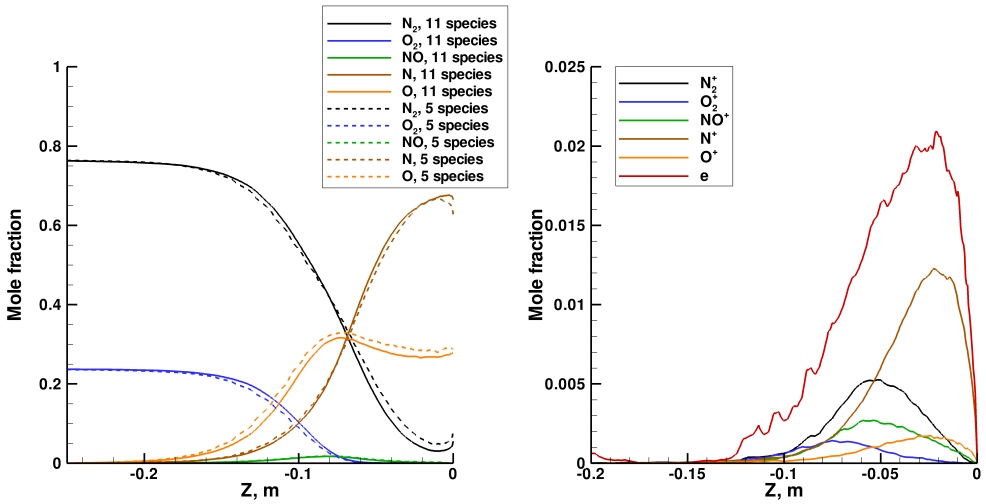

(a) Neutral species for both 11 and 5 species cases.

(b) Charged species.

Figure 3.4: Mole fractions along the stagnation streamline from the FIRE II 85 km fore body simulation.

effect described here. A data point representing the summation of the computed radiative and convective heat flux is shown on Fig. 3.5(b). The contribution of absorbed radiation to the measured heat flux at this flight condition is small.

3.6.2 Forebody at 76 km

The free stream conditions for this flight condition are given in Table 3.2[2]. The same gridding methodologies discussed in the previous section are used for this simulation. This flight condition is considered to be at the lower end of the transitional flow regime, and there are regions of the flow field that are in translational equilibrium where the Navier-Stokes equations are valid. The relatively low Knudsen number of this case makes it a computationally expensive simulation to complete using the DSMC technique. Sampling is begun after 300 000 time steps, and 50 000 sampling iterations are performed. The simulation has 36 million particles, runs on 120 processors on the NASA Columbia supercomputer, and requires about 58 wall hours to complete. There is a maximum of 4 electron particles in the cells along the

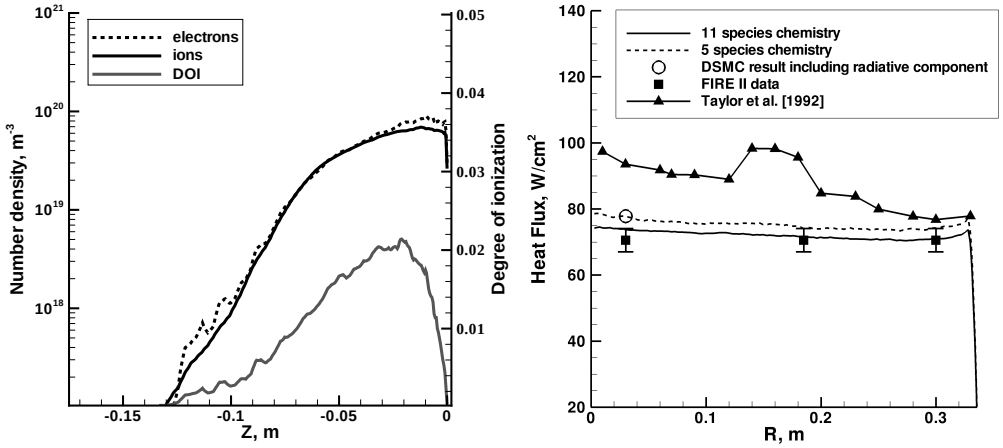

(a) Degree of ionization along the stagnation streamline.

(b) Surface heat flux for both 11 and 5 species cases.

Figure 3.5: Results from the FIRE II fore body simulation at 85 km.

axis in this simulation.

Table 3.2: Flow conditions for Project FIRE II at 76 km.

Free Stream Condition	Value
Altitude	76.4 km
ρ_∞	3.72×10^{-5}kg/m^3
U_∞	11.36 km/s
M_∞	41
T_∞	195 K
T_{wall}	615 K
Kn_∞	0.003

The temperature profiles along the stagnation streamline are shown in Fig. 3.6 for both the 11 species and 5 species chemistry models. At this altitude, the addition of ionization physics has a much more pronounced effect on the flow field, causing a relatively large movement of the shock towards the vehicle surface, and significantly reducing the rotational temperature. These trends are also reported in Ref. [18]

for a simulation of the same flight condition. There is more scatter present in the data for both the rotational and vibrational temperatures produced using the 5 species chemistry model because the exclusion of ionization chemistry results in a lower number density of molecular species in the flow field. The number density of electrons and ions, and the degree of ionization along the stagnation streamline are presented in Fig. 3.7(a). Again, charge neutrality is enforced in the flow field using the baseline electric field model. The degree of ionization peaks at approximately 7% downstream of the shock in this case, similar to the value reported in Ref. [18].

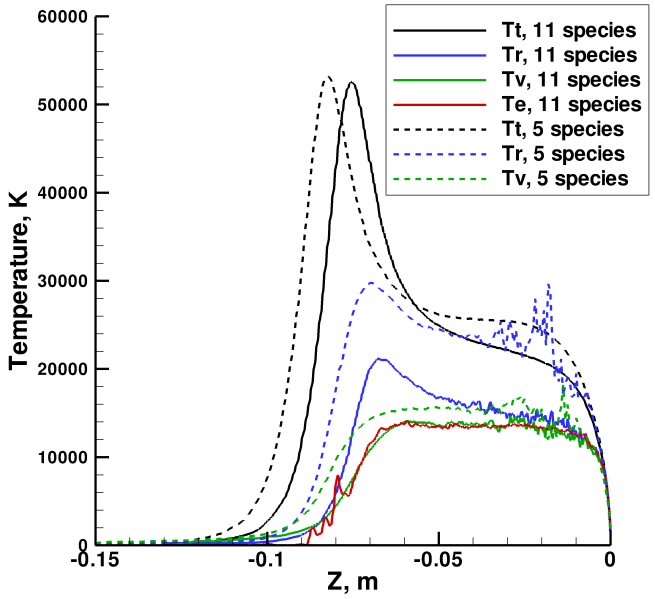

Figure 3.6: Temperatures along the stagnation streamline for both the 11 species and 5 species cases, FIRE II at 76 km.

Figure 3.7(b) shows the computed heat flux at the capsule surface for both chemistry sets along with the FIRE II experimental data. The 11 species simulation under-predicts the measured heat transfer by approximately 20% without the radiative component included. The predicted radiative component of the heat flux is 28.6 W/cm^2 at this altitude. A data point representing the summation of the computed

radiative and convective heat flux is shown in Fig. 3.7(b), and this result under-predicts the measured heat transfer at this flight condition by approximately 8%. By comparison, Taylor et al.[18] reported results that over-predicted the total heat transfer by 20%-30% in the stagnation region at this flight condition; these results are also shown in Fig. 3.7(b). They did not include radiant heat absorbed by the calorimeter in their calculation; including that would increase the level of disagreement of the Taylor et al. results with the experimental data, and bring their results at the R = 0.185 m location out of agreement with the data.

Again, a portion of the difference between the convective heating results predicted by this thesis and the Taylor et al. results is likely due to the treatment of the catalycity of the surface to oxygen atom recombination included in the latter simulation. At this flight condition, the results in Figure 3.7(b) indicate that some level of surface catalycity would have to be assumed to bring the surface heating predictions into better agreement with the experimental data. It is likely that some amount of BeO was formed on the surface of the heat shield during vehicle reentry, rendering the surface catalytic to oxygen atom recombination. However, it is not possible to determine the precise value of the surface recombination coefficient, due to the complex chemical nature of the gas-surface interaction, as well as the unknown composition and roughness of the vehicle's surface during reentry. For this reason, surface catalycity was not modeled in this thesis, and instead a lower bound was placed on the predicted convective heat flux to the vehicle surface.

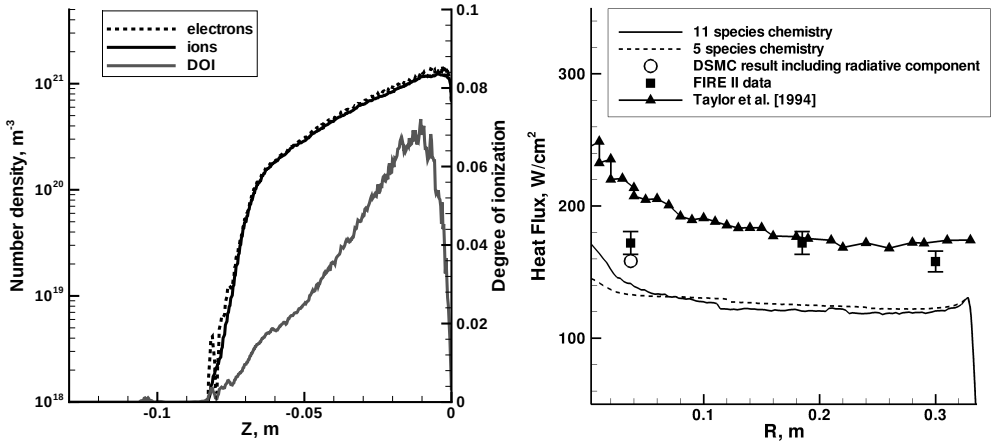

(a) Degree of ionization along the stagnation streamline.

(b) Surface heat flux for both 11 and 5 species cases.

Figure 3.7: Results from the FIRE II fore body simulation at 76 km.

3.6.3 Full vehicle simulation at 85 km

A simulation of the entire flow field at the 85 km flight condition is carried out using a completely quadrilateral mesh. Again, the meshing strategy described above is used in the fore body region. In the aft body region, the cell lengths are less than the local mean free path everywhere. Sampling is commenced after 100 000 time steps, and a total of 100 000 sampling iterations are performed in order to reduce the level of statistical scatter in the solution of the region along the conical frustum. The simulation has 36 million particles, runs on 36 processors, and requires about 110 wall hours to complete. There is a maximum of 10 electron particles in the cells in front of the vehicle along the symmetry axis. Many cells along the conical frustum have fewer than one electron particle.

Figure 3.8 shows contours of translational temperature throughout the simulation domain, showing the flow expansion around the shoulder of the vehicle where the temperature drops, and subsequent recompression of the wake near the rear of the

vehicle where the temperature increases.

Figure 3.9 shows contours of charged particle number density, where the flood corresponds to electron number density, and the lines to ion number density. The flow is approximately charge neutral in the fore body region, and remains so around the shoulder of the vehicle and over the surface of conical frustum. However, in the rear portion of the wake, down stream of the base of the vehicle, the baseline electric field model fails to maintain charge neutrality. Figure 3.10(a) shows ion and electron number density extracted along a ray extending from the vehicle surface at the midpoint of the conical frustum to the top boundary of the flow domain. Despite the large amount of scatter in the results near the surface, due to very low number density along the surface, charge neutrality is well maintained in this region. Figure 3.10(b) shows the same flow field variables along the rear centerline of the domain, along a ray extending from the base of the vehicle to the edge of the flow domain. In this region, the ion and electron number densities differ by an order of magnitude. This break down of the baseline electric field model occurs because in the rear center line region of the flow, the ions have a very large average axial velocity and very small radial velocities. Since the electrons are transported with the cell-based average ion velocity in the baseline model, they cannot diffuse into the rear center line region. This limitation of the approximate electric field model must be taken into account when using the resulting plasma density predictions to predict the attenuation of electromagnetic waves in the wake region of the flow field.

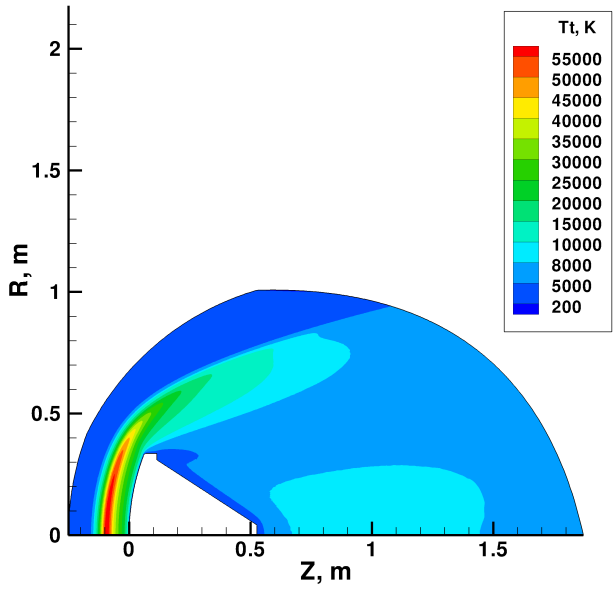

Figure 3.8: Contours of translational temperature for FIRE II at 85 km.

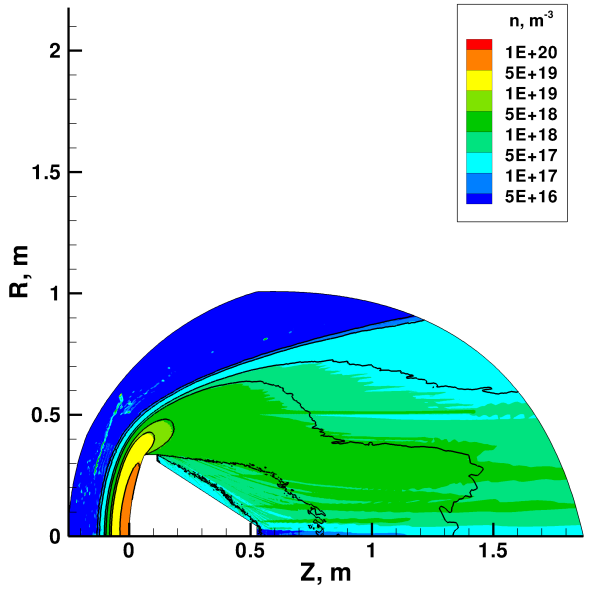

Figure 3.9: Contours of number density for FIRE II at 85 km. Lines correspond to ions, the flood corresponds to electrons.

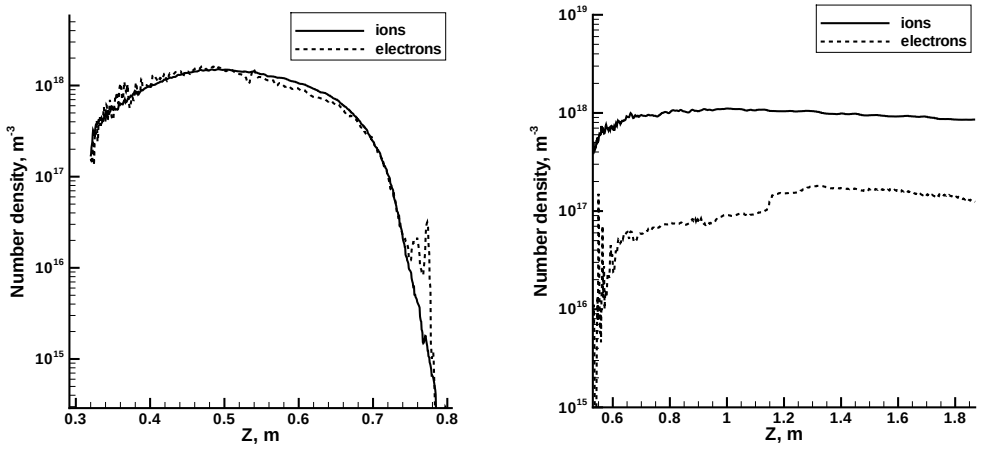

(a) Mid-point of conical frustum.

(b) Rear center line.

Figure 3.10: Number densities of charged species from the full body FIRE II result at 85 km.

3.6.4 3D simulation at 85 km

A simulation of the 85 km flight condition is carried out to test the implementation of the baseline electric field model in three dimensions. The symmetry of the flow field is invoked to use a computational grid that is a slice of the fore body domain, as shown in Figure 3.11(a), with symmetry boundary conditions imposed on the sides in the azimuthal direction. Figure 3.11(b) shows the ion and electron number densities from the three dimensional result, as well as those from the previous axisymmetric simulation. The results are nearly identical except for statistical scatter. Comparisons of the other flow field parameters from the two simulations yield the same result, and it is concluded that the baseline electric field model is operating as expected in three dimensional MONACO.

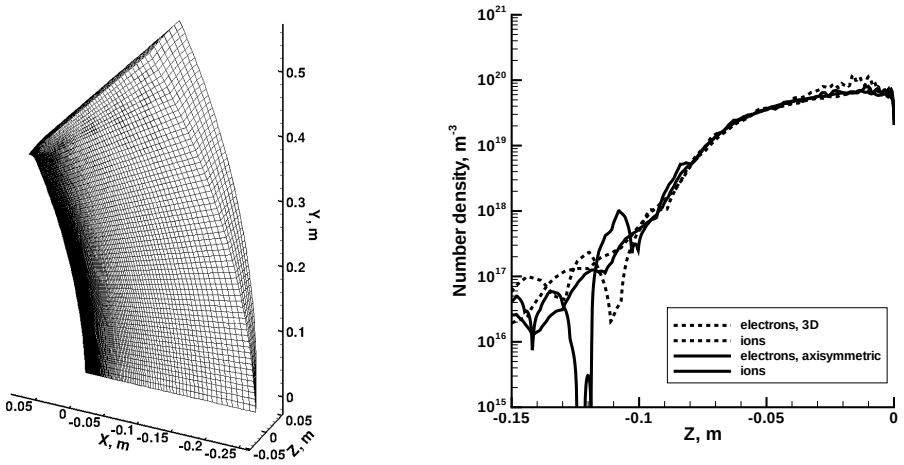

(a) Computational grid used for the 3D simulation.

(b) Charged species number densities along the stagnation streamline of both the 3D and axisymmetric fore body solutions.

Figure 3.11: Computational grid and number density results from the 3D simulation of FIRE II at 85 km.

CHAPTER IV

Cross Section Data for Modeling Particle Interaction and Chemistry

This chapter addresses the accuracy of both the cross sections used to model charged particle collisions in the VHS model, and the reaction rate coefficients used in the baseline TCE chemistry model. An additional goal of this chapter is to determine the sensitivity of the flow field results presented in Section 3.6 to the way in which collisions and chemical reactions involving charged species are modeled. Due to the kinetic nature of the DSMC method, in principle, cross section data for all types of particle interactions can be used in the algorithm, in lieu of the phenomenological models presented in Chapter III. However, this data is not available for collisions between all species, transitions between all rotational and vibrational energy levels, nor for all reaction mechanisms. Thus, phenomenological modeling techniques are commonly used. In this chapter, cross section data from the literature are used in lieu of the VHS parameters for electron-neutral collisions, and in lieu of the TCE model for electron impact ionization, electron impact dissociation, and associative ionization reactions. The FIRE II 85 km flight condition is used as a representative test case to identify the impact of these modeling changes on the flow field parameters.

4.1 The Use of Cross Section Data with the DSMC method

In principle, the collision cross section that is used to select colliding pairs in the NTC method can be replaced with cross section data for collisions between specific species pairs that is obtained experimentally, from theoretical considerations, or using computational chemistry techniques. In this case, the data is used in the NTC collision selection scheme by modifying Equation 2.14:

$$P_{c_{ab}} = \frac{(\sigma_{T_{ab}}\, c_r)}{(\sigma_{T_{ab}}\, c_r)_{max}} \tag{4.1}$$

for a collision between species a and b, if data for the total collision cross section $\sigma_{T_{ab}}$ is available.

In the TCE chemistry model, the probability of two particles reacting once they have been selected for a collision is derived such that the total reaction rate coefficient produced at equilibrium matches an experimentally determined or recommended reaction rate of Arrhenius form. The shape of the reaction cross section is chosen solely to satisfy this constraint, and may not compare well with actual reaction cross section data. Similar to the collision model, the TCE chemistry model can be replaced with a probability formed from available reaction cross section data:

$$P_{r_{ab,1\to 2}} = \frac{\sigma_{r_{ab,1\to 2}}}{\sigma_{T_{ab}}}, \tag{4.2}$$

if both total collision cross section data and reaction cross section data is available for the species of interest. This data is obtained from experiments or using computational chemistry techniques. Equation 4.2 is complicated by the fact that the reaction cross sections are a function not only of the relative energy of the colliding pair, but of the electronic and internal energy states:

$$\sigma_{r_{ab,1\to2}} = \sigma_{r_{ab,1\to2}}\left(c_r, E_{int_a}, E_{elec_a}, E_{int_b}, E_{elec_b}\right). \tag{4.3}$$

In the rest of this work, the subscript ab is dropped for clarity as the species under consideration will be clear from the context, and the notation for transition between initial and final states, 1→2, is truncated to 12.

When using cross section data in a DSMC simulation, one must be careful to identify the initial and final states of the particles involved in the reaction that the data pertains too. A reaction rate for a specific transition is found by integrating the reaction cross section over all possible initial relative momenta of the reacting particles, p_1[46]:

$$k_{12} = \int_{p_{r_1}} c_{r_1}\sigma_{r_{12}} f(p_{r_1}) d^3 p_{r_1}. \tag{4.4}$$

Additionally, it must be ensured that the data fulfills the principle of detailed balance. In translational equilibrium, the forward and reverse reaction rates governing the transition between specific states given by Equation 4.4 must satisfy the detailed balance relation[46]

$$k_{12} = k_{21}\left(\frac{\mu_2}{\mu_1}\right)^{3/2} e^{-\Delta E_{21}/kT}, \tag{4.5}$$

where μ is the reduced mass of the system and ΔE_{21} is the change in translational energy of the system.

When the distribution of internal energy states of the reactants and products is the Boltzmann distribution (that is, the internal energy states are populated according to their distributions at thermal equilibrium) then the weighted sum of all reaction rates from all possible reactant states ‘i’ to all possible product states ‘f’ is

$$k_f = \sum_i \sum_f k_{if} x_i, \tag{4.6}$$

with x_i given by

$$x_i = \frac{1}{Q_{r_{int}}} e^{-\frac{E_i}{kT}}, \tag{4.7}$$

which is the Boltzmann distribution of internal energy states of the reactants. The total forward reaction rate at equilibrium, k_f, and the similarly computed reverse reaction rate, k_b, will satisfy the Law of Mass Action[46]

$$\frac{k_f}{k_b} = \frac{Q_p}{Q_r} e^{-\Delta E_o/kT} = K_{eqm}(T), \tag{4.8}$$

where the values Q_r and Q_p refer to the total internal and translational partition functions of the reactants and products, and E_o is the difference in the lowest energy states of reactants and products. It is the total, average forward (k_f) and reverse (k_b) reaction rate coefficients from Equation 4.8 that are used as inputs to the TCE chemistry model, so when the TCE model is used, the threshold energy in Equation 2.18 is $E_a = E_o$. The equilibrium constant, K_{eqm}, that appears in Equation 4.8 has been computed and tabulated using the known energy levels of air species[47].

4.2 Collisions Between Electrons and Neutrals

In the baseline fore body simulation of the 85 km FIRE II case presented in Section 3.6.1, the fourth, sixth and seventh most frequent collisions are those between nitrogen atoms and electrons, oxygen atoms and electrons, and nitrogen molecules and electrons. This is not surprising since the small mass of the electrons leads to a large relative velocity and large collision rate. For collisions of electrons with neutral particles, the relative velocity dependence of the cross sections produced using the

standard VHS model with $0 \leq \omega \leq 0.5$ does not agree with the data obtained both experimentally and computationally. In this work, total cross section data from the literature for collisions of electrons with molecular nitrogen[48, 49], oxygen[50, 51] and atomic nitrogen[52] are fit using the VHS form of the collision cross section

$$\sigma_{VHS} = \frac{\sigma_{ref}}{\Gamma(2-\omega)} \left(\frac{2kT_{ref}}{\mu} \right)^{\omega} c_r^{-2\omega} \tag{4.9}$$

to produce more accurate modeling parameters. The new modeling parameters are given in Table 4.1 and are very similar to those presented in Ref. [19]. In addition, the collision cross section of electrons with molecular nitrogen shows a shape resonance feature in the energy range of 1.5 eV - 4.0 eV. This feature is included in the model for e-N_2 collisions using the following expressions[19]

$$\begin{aligned} \sigma_T &= \sigma_{VHS} + \frac{22}{0.7}\left(\varepsilon - 1.5\right), 1.5 \leq \varepsilon \leq 2.2, \mathring{A}^2 \\ \sigma_T &= \sigma_{VHS} - \frac{22}{1.8}\left(\varepsilon - 4.0\right), 2.2 < \varepsilon \leq 4.0, \mathring{A}^2 \end{aligned} \tag{4.10}$$

where relative collision energy (ε) is given in eV.

Table 4.1: New VHS model parameters for collisions of electrons with neutral species.

Colliding pair	σ_{ref}	T_{ref}	ω
N_2 - e	7.0×10^{-20}m^2	288 K	-0.10
N - e	2.7×10^{-19}m^2	288 K	0.19
O - e	6.0×10^{-20}m^2	288 K	-0.05

Figures 4.1, 4.2 and 4.3 show the total collision cross sections as a function of relative collision energy for each colliding pair. Shown on each figure are the cross sections computed using the original (baseline) VHS parameters, the fits to the data, and

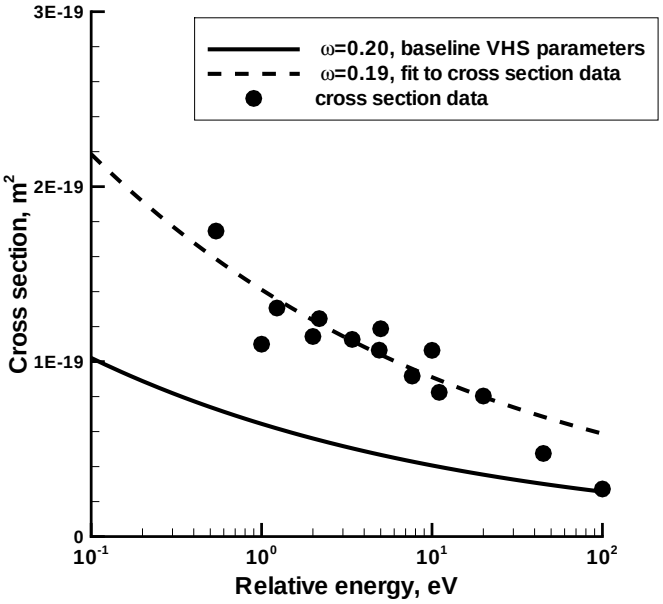

Figure 4.1: Cross section data for e - N collisions.

the relevant data sets from the literature. Error bars are not included on the data for e-N collisions, as computational tools were used to obtain the values and no uncertainty on the estimates is given in Refs. [48, 49]. The data for e-N_2 collisions is compiled from a variety of experimental sources using weighted averages, and the total uncertainty is estimated in Ref. [52] only for collision energies less than 1 eV. From these comparisons it is clear that the addition of the collision cross section data will result in an increase in the collision rate of electrons with N, O and N_2, except at collision energies below approximately 1 eV in the case of e-O and e-N_2 collisions.

4.2.1 Comparison to baseline collision model

Three fore body simulations at the 85 km flight condition are conducted in which the baseline VHS model parameters are replaced by the new VHS model parameters in a systematic fashion. No appreciable change is observed in the temperature profiles along the stagnation streamline, nor in the heat transfer to the vehicle surface. Since

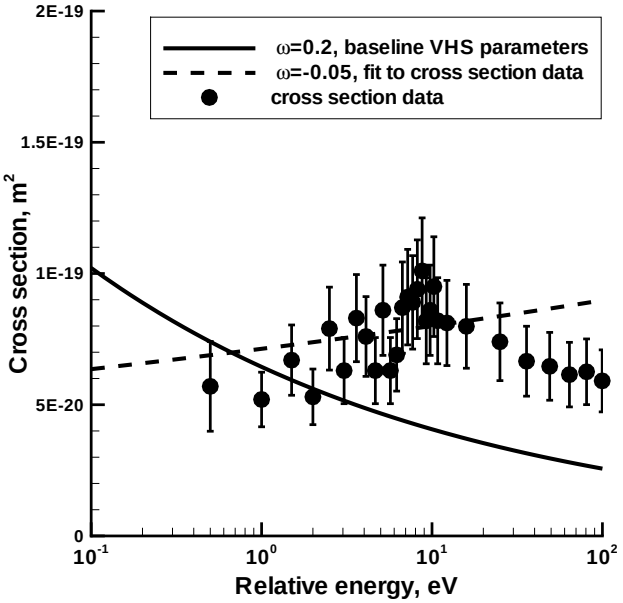

Figure 4.2: Cross section data for e - O collisions.

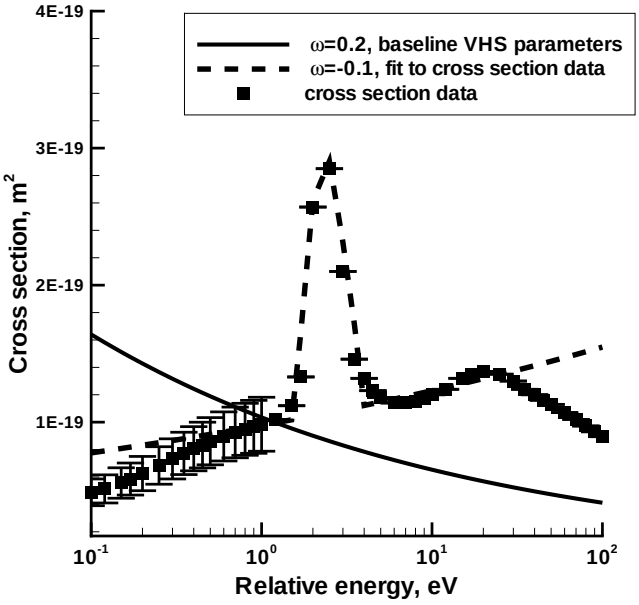

Figure 4.3: Cross section data for e - N_2 collisions.

the energy transferred in an elastic collision from particles 2 to 1 is proportional the mass ratio $\Delta E_1 \sim m_1/m_2$, the increased collision rate predicted by the new modeling parameters does not result in the transfer of an appreciable amount of energy from the heavy species to the electrons.

The remaining three classes of interactions involving charged particles: ion-neutral, ion-ion, and ion-electron are not considered further in this work. The long range nature of the latter two classes, ion-electron and ion-ion, is accounted for by the macroscopic electric field model. Short range interactions between ions and electrons will be unimportant in the flow fields of interest due to the same mass ratio considerations discussed above. Short range interactions between ions, while efficient at transferring energy, are unlikely to affect the structure of the flow field due to the low degree of ionization in the flow fields of interest here. The same can be said for interactions of ions with neutrals, so the baseline VHS model is deemed sufficient to treat the remaining three classes of charged particle interactions in the flow fields of interest to this thesis.

4.3 Electron Impact Dissociation of N_2

The electron impact dissociation of molecular nitrogen is assumed to proceed via predissociation of an electronically excited N_2^* state as follows:

$$N_2 + e \rightarrow N_2^* + e \rightarrow N + N + e. \tag{4.11}$$

Cross sections for this reaction are presented by Cosby[53]. They were obtained using a crossed beam experiment and two different nitrogen ion sources that were neutralized by near-resonant charge transfer. The experiment yielded cross section measurements for electron-impact energies between 10 and 200 eV. The vibrational

and electronic state populations of the N_2 were not measured but it was estimated that in the hollow cathode ion source, more than 90% of the N_2^+ population was in the ground electronic and vibrational state. In the N_2 beam produced using the electron impact ion source, it was estimated that no more than 24% of the nitrogen was vibrationally excited, and again that it was in the ground electronic level. Both of these estimates were based on a comparison of the partial cross sections, for specific values of vibrational level ν, for neutralization of the N_2^+ produced in each ion source by the symmetric charge exchange reaction given by

$$N_2^+(X,\nu') + N_2(X,\nu=0) \rightarrow N_2(X,\nu'') + N_2^+(X,\nu). \tag{4.12}$$

Cosby's analysis of the translational energy distributions of the product particles did indeed indicate that the predissociation from bound, electronically excited N_2^* states makes the dominant contribution to the electron impact dissociation of N_2, as indicated in Equation 4.11, rather than the excitation of the molecule to, and subsequent dissociation from, a dissociative continuum as described by Equation 4.13.

$$N_2 + e \rightarrow N + N + e. \tag{4.13}$$

His comparison of the cross section data obtained from the two different ion sources did not yield any systematic differences, despite their different vibrational populations.

It is assumed in the following analysis that the cross sections for dissociation are equal for all vibrational and rotational levels of the N_2 molecule in the ground electronic state. Because in general the probability of a termolecular collision is extremely low in the rarefied gas regime, recombination is not considered. In the

reaction mechanics of the DSMC code, the colliding nitrogen molecule is in the ground electronic state, and the resulting nitrogen atoms are also in their ground states yielding a dissociation energy of 9.75 eV[53]. Due to the nature of the reaction mechanism given in Equation 4.11, it is assumed that the internal energy of the nitrogen molecule does not contribute to the threshold energy required for a reaction to occur.

Figure 4.4(a) shows the measured reaction cross section data and that computed using the TCE model with the rate coefficient given in Table A.2. The reaction cross section predicted by the TCE model is computed as follows

$$\sigma_{r,TCE} = P_{TCE}\left(E_{tot}\right) \times \sigma_{VHS}\left(E_{tot} - 0.5\,\overline{\zeta_{int}}\,kT\right), \tag{4.14}$$

where P_{TCE} is the reaction probability computed using the TCE model, which is formulated assuming that $\overline{\zeta_{int}}$ internal degrees of freedom contribute energy to the reaction[7]. In this thesis, $\zeta_{rot} = 2$ and $\zeta_{vib} = 1.8$, making $\overline{\zeta_{int}} = 1.9$ since electrons do not possess rotational or vibrational structure. It is also instructive to compare the reaction rate coefficient produced by the cross section data at equilibrium using Equations 4.4 and 4.6, to that used in the TCE model given in Table A.2. Figure 4.4(b) shows the variation of both rate coefficients with temperature. It is clear that the rate coefficient produced by the Cosby data is lower than that used in the TCE model at all temperatures. The TCE rate coefficient was originally estimated based on the requirement that existing radiation data from shock tubes be reproduced[54].

4.3.1 Comparison to baseline chemistry model

A simulation of the FIRE II 85 km flight condition is performed, in which the reaction cross section data and collision cross section data is used, along with Equa-

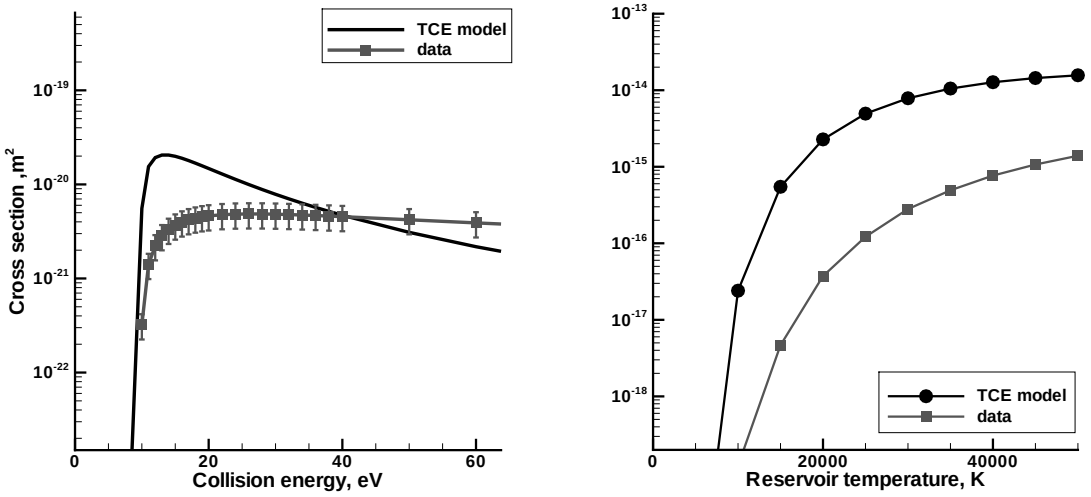

(a) Reaction cross section data.

(b) Reaction rates.

Figure 4.4: Comparison of cross section data to TCE model predictions for electron impact dissociation of N_2.

tion 4.2, to replace the TCE model. Figure 4.5(a) shows the temperatures along the stagnation streamline obtained from this simulation, along with the result presented previously that utilized the baseline TCE model to compute this reaction. Due to the reduced reaction probability associated with the cross section data, there are fewer dissociation events and the internal mode temperatures and the electron translational temperature are increased. Figure 4.5(b) shows that the mole fractions of charged species along the stagnation line have significantly increased due to the high energy electrons now present in the flow. Specifically, the mole fractions of O^+ and N^+ have increased significantly, presumably due to the increased importance of the electron impact ionization reactions in the presence of the higher energy electrons. The maximum local degree of ionization in the flow field has increased by over 50% to slightly greater than 0.03 in the post-shock region. Lastly, Fig. 4.6 shows that the heat flux along the capsule surface is slightly increased with the use of the

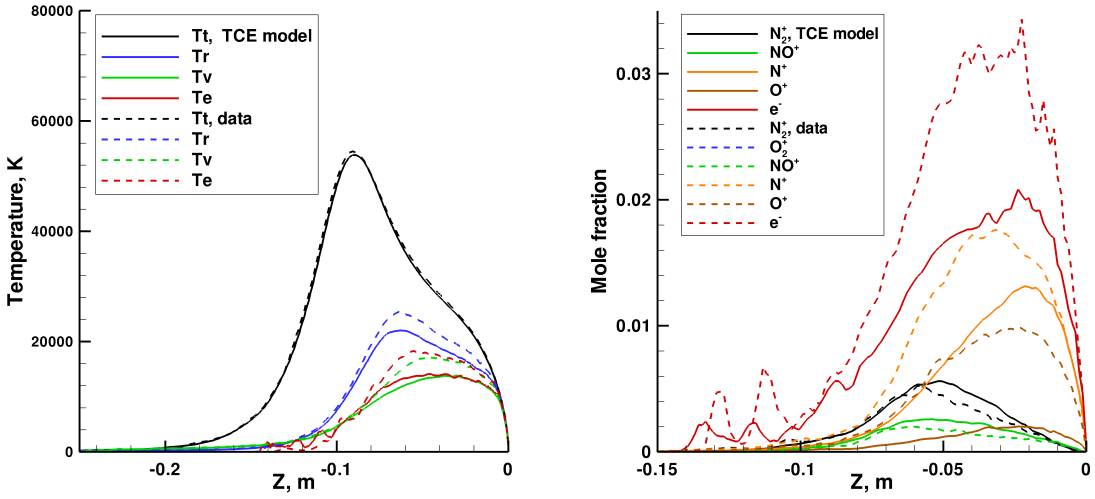

(a) Temperatures along the stagnation streamline.

(b) Mole fractions of charged species.

Figure 4.5: FIRE II fore body simulation at 85 km using cross section data to model dissociation of N_2 by electron impact.

Cosby data, due to the reduced level of nitrogen dissociation in the flow field. A data point from one of the calorimeters on the FIRE II heat shield is also shown in this figure. The addition of the cross section data results in slightly worse agreement with the experimental data, however this is hardly a conclusive result because there are many other sources of uncertainty in the physical and chemical data used in these types of simulations.

Although the use of the cross section data has a relatively small effect on the convective heat transfer shown in Fig. 4.6, it plays a large role in the prediction of the radiative portion of the heat flux. This is due to the increase of the electron translational temperature in the flow field, as the finite rates of electronic excitation increase with an increase in the electron translational temperature. An uncoupled calculation of the total radiative heat flux to the capsule surface yields a value of 8 W/cm^2 using the flow field results computed using the TCE model as input, while

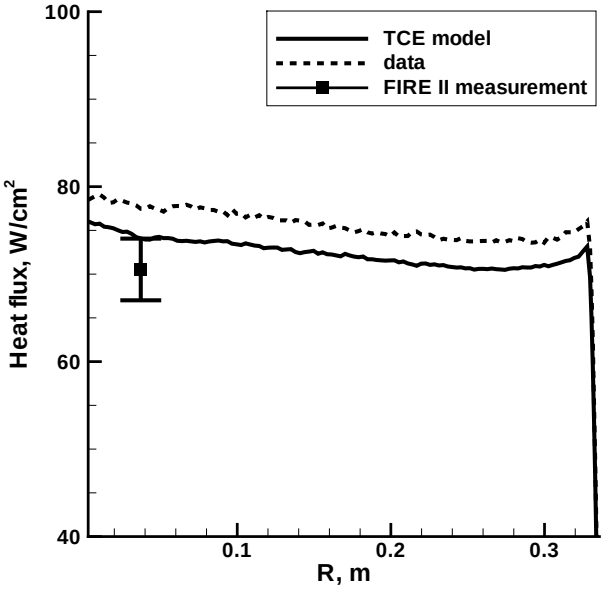

Figure 4.6: Convective heat flux from FIRE II fore body simulation at 85 km using cross section data to model dissociation of N_2 by electron impact.

this value increases to 24 W/cm^2 for the flow field computed using the Cosby dissociation data.

4.4 Electron Impact Ionization of N and O

Experimental and theoretical cross section data for the electron impact ionization of oxygen and nitrogen were compiled by Bell et al.[55]. It is important to note that the baseline rate coefficients due to Wilson that are used in the TCE model correspond to ionization of nitrogen and oxygen from their first excited states[25], N(^{2}D) and O(^{1}D), while the cross section data taken from Ref. [55] corresponds to ionization from the ground electronic states, N(^{4}S) and O(^{3}P), of both atoms. In practice, this means that when the rates of Wilson are used in the DSMC method, the threshold energy is equal to that required to ionize the atoms from their first excited electronic states, whereas when the cross section data is used, the threshold

energy is equal to that required to ionize the atoms from their ground electronic states. Table 4.2 summarizes the threshold energy for each reaction. One of the limitations of the TCE chemistry model is that the threshold energy, E_a, has to be equal to the energy removed from the reacting particles (and converted to chemical potential energy) during a reaction event. Because the excitation of the electronic mode is not explicitly modeled in the thesis, using the cross section data for these reactions in lieu of the baseline TCE model results in the removal of more energy from the flow field each time an ionization event occurs by this mechanism. Again, due to the low probability of a termolecular collision in the rarefied gas regime, the recombination reactions are not considered.

Table 4.2: Threshold energies for electron impact ionization of N and O.

Reaction	Threshold energy, eV
$N(^4S) + e \rightarrow N^+ + 2e$	14.5
$N(^2D) + e \rightarrow N^+ + 2e$	10.4
$O(^3P) + e \rightarrow O^+ + 2e$	13.6
$O(^1D) + e \rightarrow O^+ + 2e$	9.2

Figures 4.7(a) and 4.7(b) show comparisons of the recommended cross sections from Ref. [55] to the reaction cross sections obtained with the TCE model using the rate coefficients given in Table A.3. For both reaction mechanisms it is clear that in the energy range of interest (10-15 eV), the TCE model yields reaction cross sections that are larger than the cross section data.

The cross section data are converted to equilibrium reaction rates using Equation 4.4, and compared to the reaction rates used in the TCE model in Figures 4.8(a) and 4.8(b). The rate coefficients used in the TCE model are again larger than those obtained from the cross section data at all temperatures.

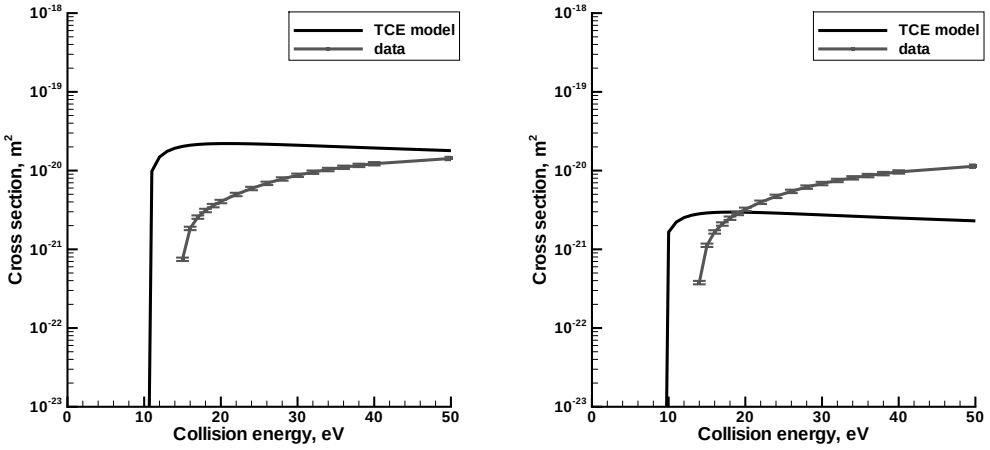

(a) e - N. (b) e - O.

Figure 4.7: Comparison of cross section data to TCE model predictions for electron impact ionization of N and O.

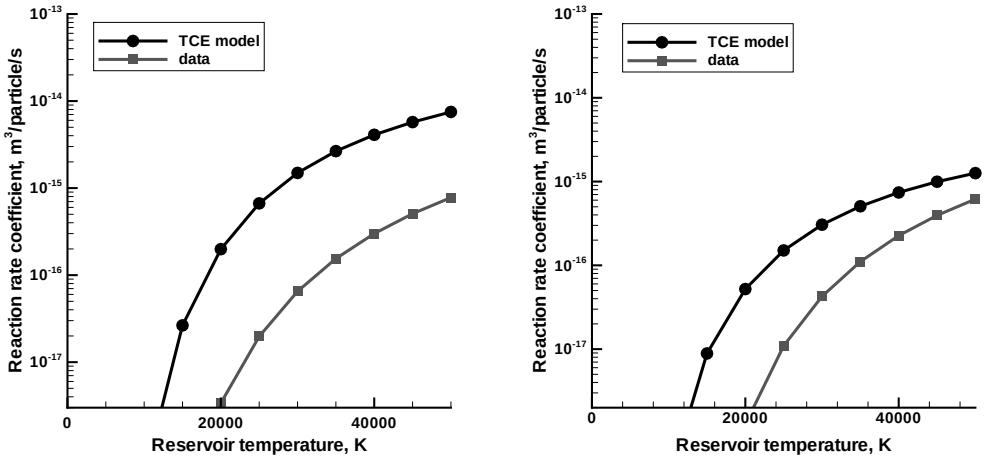

(a) e - N. (b) e - O.

Figure 4.8: Comparison of reaction rates derived from cross section data to the reaction rate used in the TCE model for electron impact ionization of N and O.

4.4.1 Comparison to baseline chemistry model

Another simulation of the FIRE II 85 km flight condition is performed, in which the reaction cross section data and collision cross section data is used along with Equation 4.2 to replace the TCE model. In this simulation, all three reactions involving electron impact that are listed in Tables A.2 and A.3: 1e) $N_2 + e \rightarrow N + N + e$, 20) $N + e \rightarrow N^+ + 2e$ and 21) $O + e \rightarrow O^+ + 2e$, are modeled using the relevant cross section data.

In the previous section, it is shown that the use of the cross section data for reaction 1E results in a higher electron temperature, which in turn means that the electron impact ionization reactions play a larger role in determining the flow field character. As such, the DOI increases in those simulations relative to the baseline results. With the addition of the cross section data for reactions 20 and 21, Figure 4.9(b) shows that the mole fractions of charged species along the stagnation streamline are reduced to very near the values obtained using the baseline chemistry set. A reduction in the level of ionization is expected as the ionization cross sections from the ground electronic level given by Bell et al. are lower, in the temperature range of interest, than those predicted using the equilibrium rates from the baseline chemistry set. However, the fact that the mole fractions have returned to nearly their baseline values is coincidence. The mode temperatures along the stagnation streamline are shown in Fig. 4.9(a). The mode temperatures are almost completely unchanged from the previous result computed using only the data for e-N_2 dissociation. This is likely due to the fact that the threshold energies used in the TCE model for reactions 20 and 21 are substantially lower than those associated with the cross section data. Thus, even though fewer electron impact ionization events are taking place, the net energy loss in the bulk flow region is approximately the same. The heat transfer at

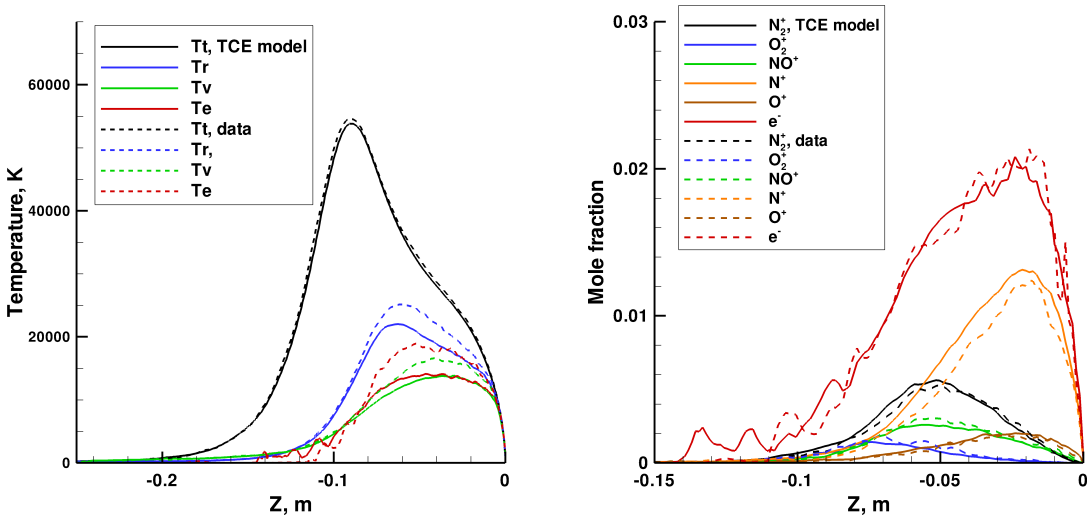

(a) Temperatures along the stagnation streamline.

(b) Mole fractions of charged species.

Figure 4.9: FIRE II fore body simulation at 85 km using cross section data to model electron impact dissociation of N_2 and electron impact ionization of N and O.

the probe surface is unchanged from the values shown in Figure 4.6 that are obtained using only the N_2 + e dissociation data.

4.5 Associative Ionization of N with O

Due to their low threshold energies, associative ionization (AI) reactions play an important role in determining the level of ionization and structure of the flow field at the flight conditions considered in this work. There exists very little experimental or computational data in the literature regarding the associative ionization reactions in air. The associative ionization reaction of N + O $\leftrightarrow$ NO^+ + e has the lowest energy threshold, and this is the reaction that is considered in this work. Although the associative ionization of N + N $\leftrightarrow$ N_2^+ + e may have the most influence on the flow field structure at this flight condition, cross section data for this reaction could not be located in the literature for use in this analysis. In this case, both

the forward associative ionization reaction (14f in Table A.3) and the backward dissociative recombination (DR) reaction (14b in Table A.3) must be modeled.

4.5.1 Associative ionization

The AI process involves the capture of two neutral atoms into an electronically bound, discrete state (NO^*), and subsequent transition to the unbound NO^+ + e state with which it is degenerate[56]. Padellec[57] computed the partial reaction cross sections in the vicinity of the threshold energies for the associative ionization of N + O to form $NO^+(\nu = 0$, ground electronic state) + e by invoking the principle of microscopic reversibility[46], and they are a function of the electronic state of the colliding atoms. The three sets of electronic states of the colliding atoms considered by Padellec that yielded useful data sets are listed below along with the corresponding threshold energies for each reaction.

$$\begin{aligned} E1 &: N(^4S) + O(^3P), E_a = 2.77eV \\ E2 &: N(^4S) + O(^1D), E_a = 0.80eV \\ E3 &: N(^2D) + O(^3P), E_a = 0.38eV \end{aligned} \tag{4.15}$$

Additionally, Ringer and Gentry measured the absolute cross section for the AI reaction of atoms in state E3 in a merged molecular beam experiment[58].

In order to cast these sets of cross section data in a form useful in the DSMC algorithm, one has to have some information about the shape and magnitude of the cross sections away from the threshold energy for reactants in states E1 and E2. This requires including the additional partial cross sections for ionization resulting in vibrationally and possibly electronically excited states of the NO^+ ion. Ringer and Gentry were able to place an upper limit on the magnitude of the cross section for

reactants in state E1 of 15% of that corresponding to E3[58]. Consistent with this limit, it is assumed in this work that the absolute cross section for ionization from the first two reactant states (E1, E2) is of the same shape and relative magnitude as that measured by Ringer and Gentry for the electronic state, E3. The cross section data constructed using this assumption are shown in Figure 4.10(a), along with the original data sets due to Padellec and Ringer and Gentry. Also shown on Figure 4.10(a) are the reaction cross sections computed using the TCE chemistry model with the rate coefficient given in Table A.3. The rate coefficient that is used with the TCE model was deduced from measured rates for the dissociative recombination reaction of NO^++e and the appropriate equilibrium constant[54].

4.5.2 Dissociative recombination

Vejby-Christensen et al.[59] measured the total cross sections for DR of NO^+ + e in the vibrational and electronic ground state, as well as the branching ratios for the product N + O atoms. This data was used by Padellec in the computation of the forward AI reaction cross sections. The Vejby-Christensen data is compared to the cross sections computed using the TCE chemistry model with the rate coefficient listed in Table A.3 in Fig. 4.10(b). Also shown on this plot is the curve-fit used to implement the cross section data in the code. Note that the set of data produced using the TCE chemistry model utilizes a reaction probability that is a function of total collision energy, and the relation given in Equation 4.14 has been used to create Figure 4.10(b). In order to use the Vejby-Christensen cross section data in a DSMC calculation, some assumption has to be made about the cross sections for DR from vibrational states other than ν=0. In this work it is assumed that the reaction cross sections from states with ν >0 are equal to those with ν=0.

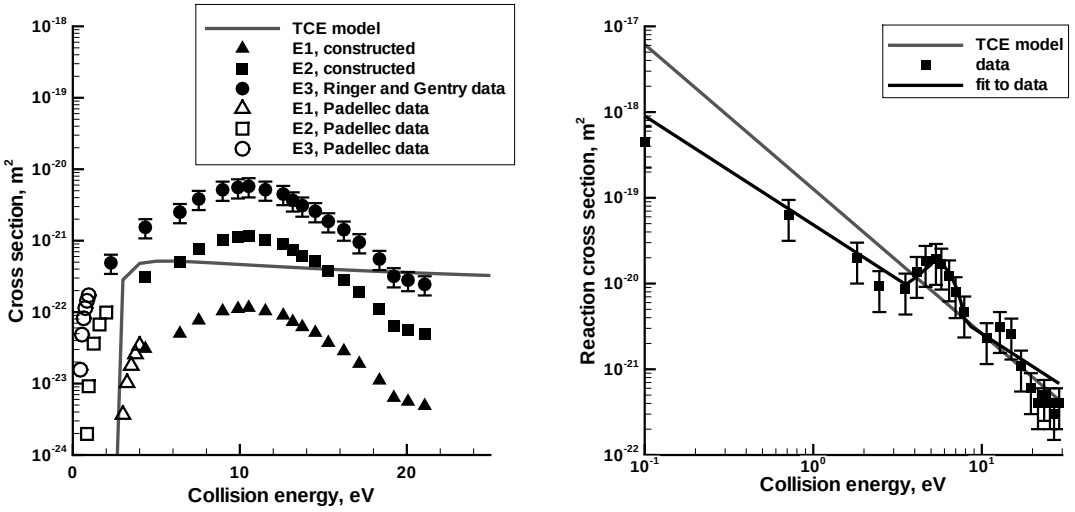

(a) Associative ionization.

(b) Dissociative recombination.

Figure 4.10: Comparison of cross section data to TCE model predictions for associative ionization of N and O. Only every fourth data point is shown for clarity.

In DSMC, particles are first selected for a collision and then each pair is tested for subsequent energy exchange and reactions using computed probabilities for each possible event. Due to the long range nature of the Coulomb interaction, the cross section for collisions between charged particles is much larger than that for collisions of charged particles with neutrals and between neutral particles. To employ such a high collision rate in a DSMC solution of an entire reentry flow field would be prohibitively expensive. Instead, the reaction cross sections for the dissociative recombination (DR) reaction are inserted directly into the collision selection algorithm in the DSMC code, and the corresponding reaction probability is then set equal to unity in the reaction selection algorithm. This means that all collisions of NO^++e will react, and none will involve only elastic or inelastic energy transfer. Although from a microscopic point of view this is unphysical behavior, it should produce the correct level of ionization in the flow field without requiring the computation of very

large numbers of collisions between charged particles.

4.5.3 Equilibrium reservoir calculation

An equilibrium reservoir simulation is performed to calculate the total forward and reverse reaction rate coefficients to compare with the rates used in the TCE model. The electronic state populations of the nitrogen and oxygen atoms are calculated using the Boltzmann distribution given in Equation 4.16 with the electronic temperature of the flow which, in this case, is the reservoir temperature.

$$F_i = \frac{g_i e^{-E_i/kT_e}}{\sum g_i e^{-E_i/kT_e}} \tag{4.16}$$

Information about the electronic levels of nitrogen and oxygen is obtained from the NIST online database[40]. Using these electronic state populations, the joint probability of occurrence for each set of electronic states listed in Equation 4.15 is formed, referred to from here on as an electronic co-state. In doing so, it is assumed that the cross sections for reactions from electronic co-states at higher energies than those given by the E3 electronic state are equal to those for the E3 electronic state. Figure 4.11 shows the distribution of each co-state given in Equation 4.15 as a function of reservoir temperature. The quantity labeled "1 - P(E1) - P(E2)" on this figure is the probability that is used to identify collisions that proceed using the E3 threshold data. The quantity labeled "P(E1)+P(E2)+P(E3)" corresponds to the fraction of possible electronic co-states of the N and O atoms that are described by the available cross section data at a given electronic temperature. For example, at a temperature of 20 000 K, approximately 75% of the possible electronic co-states are described by the available cross section data. When a nitrogen atom is selected to collide with an oxygen atom in the simulation, a random number is generated and

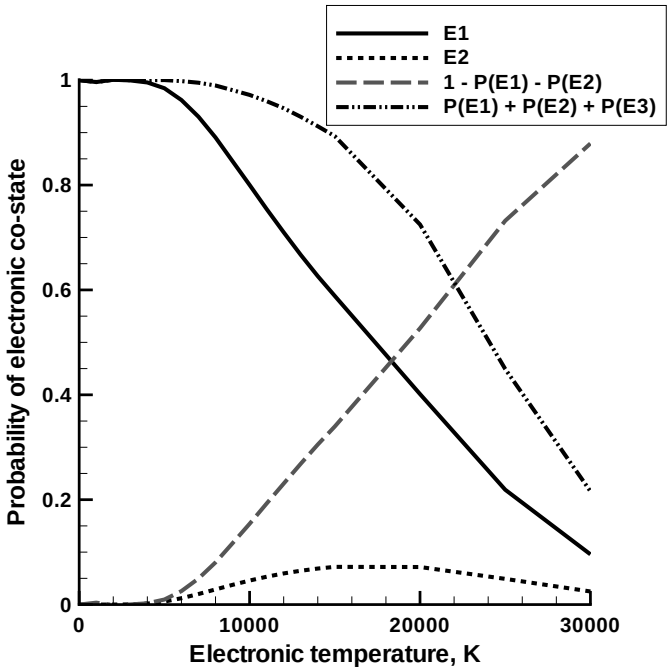

Figure 4.11: Distribution of electronic co-states used to apply cross section data for associative ionization of N, O.

used to determine the appropriate electronic co-state of the pair. The probability of a reaction is then computed using Equation 4.2 with the appropriate cross section data for that electronic co-state, and the total collision cross section computed using the VHS model.

Figure 4.12(a) shows the rate coefficient for associative ionization that is obtained from the cross section data, and the rate used in the TCE model. At temperatures greater than approximately 10 000 K, the forward rate coefficient calculated using the cross section data is greater than that predicted by the TCE model. Figure 4.12(b) shows the dissociative recombination rate obtained from the cross section data, and the rate used in the TCE model. The rate coefficient produced by the cross section data is greater than that used in the TCE model at all reservoir temperatures. The scatter in the reaction rate at the lower reservoir temperatures is due to the small number of particle collisions at those conditions.

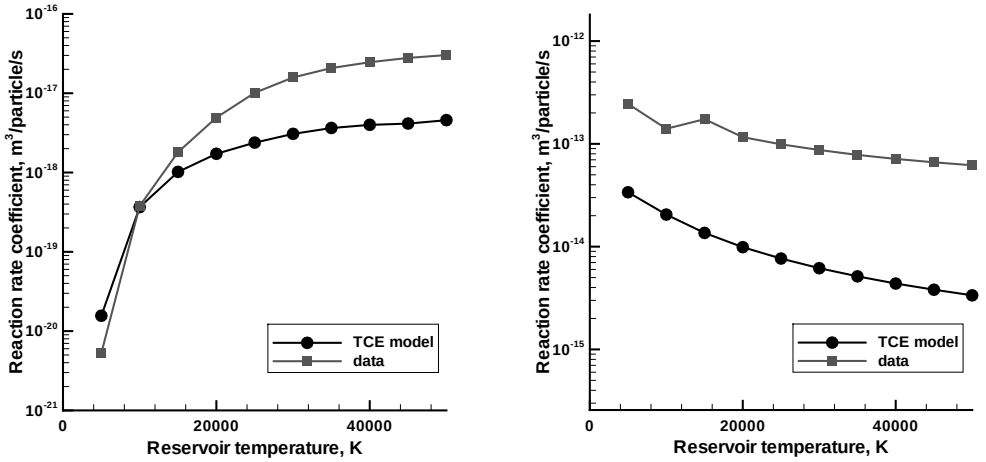

(a) Associative ionization. (b) Dissociative recombination.

Figure 4.12: Comparison of reaction rates derived from cross section data to the reaction rate used in the TCE model for associative ionization of N and O.

Equation 4.8 is used to determine the equilibrium constant given by the cross section data. Figure 4.13 shows these results, along with the value of the equilibrium constant used in the TCE model and the curve given by Park[47]. The agreement between the equilibrium constant used by the TCE model and that given by Park is fairly good at temperatures less than 30 000 K. This is expected since the equilibrium constant used in the TCE model was fit over this finite temperature range to be cast in a form usable in the model. Further discussion of this point is found in Ref. [60]. The equilibrium constant computed using the cross section data agrees with that given by Park over a smaller temperature range, but agrees much better at lower reservoir temperatures. A major source of the disagreement between the equilibrium constant computed using the AI and DR cross section data and the Park value is due to the fact that AI cross sections have been inferred for the higher electronic states of N and O, and the DR cross sections have been inferred for the higher vibrational states of NO^+. At an equilibrium temperature of 15 000 K, 10% of the atoms

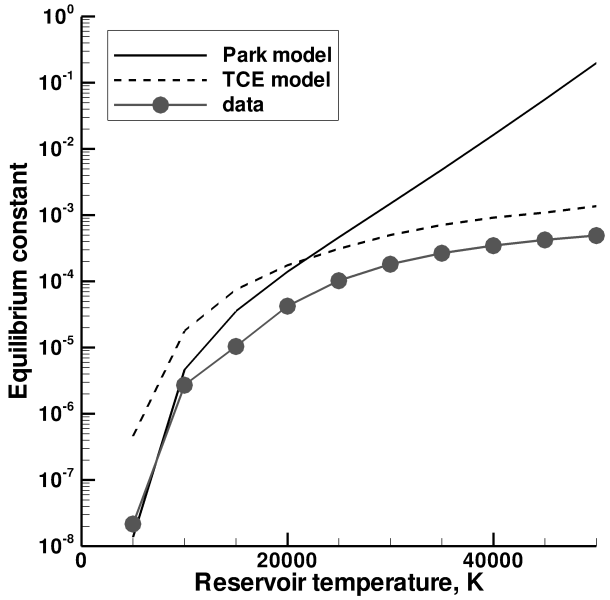

Figure 4.13: Equilibrium constants for associative ionization of N and O.

are in electronic states higher than those accounted for in the Padellec data and that percentage increases rapidly above 15 000 K. The cross sections for ionization from these states are set equal to those for the E3 threshold. At an equilibrium temperature of 15 000 K, almost all NO^+ ions are in vibrational states higher than ν=0, and the cross sections for dissociative recombination from these states are set equal to those measured for the ν=0 state.

4.5.4 Implementation in the DSMC algorithm

In order to use this cross section data in the DSMC algorithm, the electronic co-state of the reacting particles needs to be determined in some manner. Of course, the most robust (and computationally expensive) options are to directly model the electronic excitation of the atoms in the DSMC algorithm[18], or to employ a quasi-steady state approximation to compute the population of the electronic states as is typically done in codes designed to compute flow field radiation in an uncoupled

manner[44, 61]. In order to obtain a first approximation as to how much of an effect the use of the AI cross section data in lieu of the TCE model will have on the computed flow field, the electronic energy levels of both the nitrogen and oxygen atoms are assumed to be populated according to the equilibrium distribution at the local electron translational temperature of the flow field. The electronic mode temperature is assumed equal to the electron translational temperature in the simulation due to the high efficiency of energy exchange between free and bound electrons, and the procedure for co-state selection described in Section 4.5.3 is used. As shown in Chapter 3.6.1, the electron translational temperature is between 10 000 K and 20 000 K in the simulations of the FIRE II 1631 s flight condition, so at minimum 75% of the possible electronic co-states are described by the available cross-section data using this method.

4.5.5 Comparison to baseline chemistry model

Figure 4.14(a) shows that the mode temperatures are not affected by the addition of the cross section data to the simulation. This figure also shows that once an appreciable degree of ionization has occurred in the flow field, the electron temperature rises to approximately 14 000 K. The mole fractions of charged species along the stagnation streamline are shown in Fig. 4.14(b). On that figure, species are omitted whose concentration did not change with the addition of the cross section data to the simulation. The concentration of the product NO^+ has increased in the region of the flow where $T_e > 10\ 000$ K, and the overall degree of ionization has increased slightly from the baseline solution. The increase in $[NO^+]$ is consistent with the behavior of the reaction rate coefficients shown in Fig. 4.12(a), where the reaction rate coefficient predicted by the data is higher than that predicted by the TCE model for

temperatures greater than 10 000 K. The convective heat flux to the vehicle surface is not affected by the addition of the cross section data.

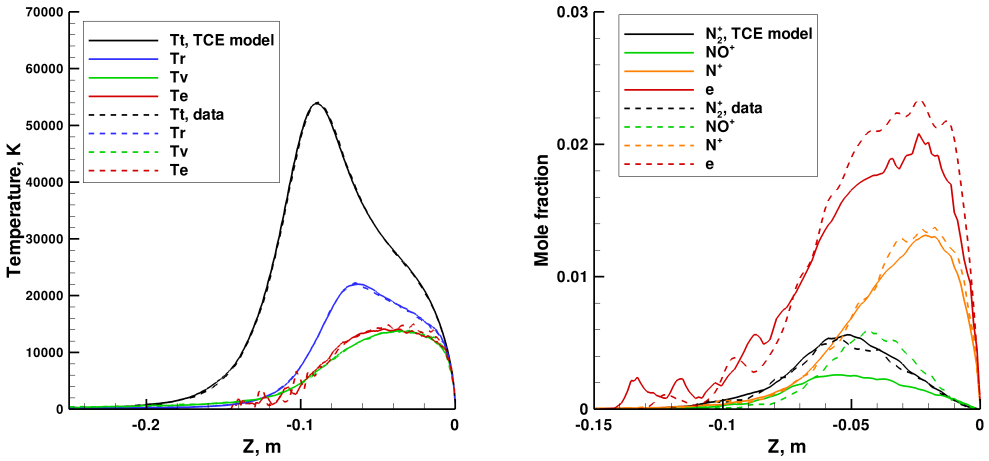

(a) Temperatures along the stagnation streamline.

(b) Mole fractions of charged species.

Figure 4.14: FIRE II fore body simulation at 85 km using cross section data to model associative ionization of N and O.

CHAPTER V

Particle-In-Cell Shock Layer Simulations

In this chapter, self-consistent, coupled DSMC-Particle-In-Cell (PIC) simulations are used to identify the limitations of the baseline electric field model, which is based on the ambipolar diffusion assumption. A simplified, one-dimensional model of the shock layer is used to produce the results presented in this chapter. The use of a simplified model is necessary to reduce the computational expense of the PIC calculations and allow DSMC-PIC solutions to be obtained.

5.1 Difficulties Associated with the use of PIC for Reentry Simulations

The use of the PIC[62] method to model a hypersonic shock layer poses a number of challenges. Because of their low mass, for a given temperature, electrons possess a thermal velocity that is two to three orders of magnitude larger than their heavy particle counterparts. This means that particle simulations in which the electrons are allowed to move freely require very small computational time steps and long simulation times to complete. Additionally, the distance between nodes in the computational mesh must be some fraction of the Debye length,

$$\lambda_D = \sqrt{\frac{\varepsilon_o k T_e}{n_e e^2}}, \tag{5.1}$$

in order for a stable solution to be obtained. Stability of the algorithm also dictates that the number of simulator particles within a Debye sphere be large. In a PIC simulation utilizing a mesh scaled on a fraction of the Debye length, this places a lower limit on the number of simulated ions and electrons in one computational cell. In this work, experimentation with mesh spacing and particle weighting led to the required values of $\Delta x \sim \lambda_D/5$ and $N_p \sim 10$ for cell width and the minimum number of charged particles per cell to ensure algorithm stability.

In a rarefied hypersonic shock layer, the Debye length is typically at least an order of magnitude smaller than the mean free path, and the degree of ionization is only a few percent. Figure 5.1(a) shows the mean free path and Debye lengths along the stagnation streamline of the FIRE II 85 km fore body simulation presented in Section 3.6.1. Also shown on this figure is the ratio of the mean free path to the Debye length. It is clear that the mean free path is two to three orders of magnitude larger than the Debye length throughout the shock layer. While the PIC method has been used to model atmospheric pressure discharges (see, for example, Ref. [63]), in those types of simulations the heavier neutral particles are not modeled explicitly, rather they are treated as a background gas. In contrast, in a coupled DSMC-PIC simulation a large number of neutral particles must be simulated in order to have enough charged particles in the domain to satisfy the stability requirements. The simulation time step is limited by the minimum cell crossing time of the fast electrons. Figure 5.1(b) shows the mean cell crossing time of the electrons and the mean collision time from the FIRE II 85 km fore body simulation presented in Section 3.6.1. The mean electron cell crossing time is many orders of magnitude smaller than the mean collision time

on which the time step utilized in DSMC calculations is based. These factors combine to make the coupled DSMC-PIC method much more computationally expensive than the DSMC method for simulating reentry flow fields.

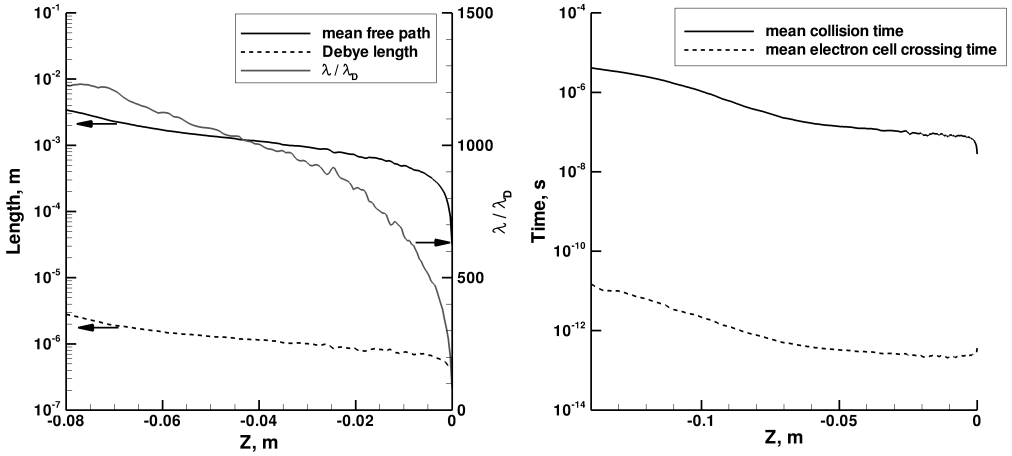

(a) Mean free path and Debye lengths.

(b) Mean collision and electron cell crossing times.

Figure 5.1: Length and time scales for the FIRE II, 85 km fore body simulation.

5.2 The Simplified Shock Layer Model

The method developed by Bird[7] for performing a one-dimensional DSMC simulation of the stagnation streamline of an axisymmetric blunt body flow is used in this study. The method exploits the fact that along the stagnation streamline of such flows only gradients in the axial direction exist. Particles can thus be removed from random locations downstream of the shock to produce a one-dimensional simulation of the steady state flow along the stagnation streamline. A complete derivation of the selection criteria for particle removal is given in Appendix B.

A calculation of the FIRE II flow field at 85 km that utilized the properties of the atmosphere directly would be intractable with the DSMC-PIC method. For this reason, the free stream density used in the shock layer model is decreased from

the value of $2 \times 10^{20} m^{-3}$ found at an altitude of 85 km in the Earth's atmosphere. The reaction rates and particle diameters are scaled so that the mean free path, and thus the shock stand off distance and boundary layer thickness, are similar to those experienced by the FIRE II vehicle at 85 km. A similar approach has been used previously[64] to model a plasma reactor using the PIC - Monte Carlo Collision method.

Two conditions are considered: Case 1 with a free stream number density of $n_\infty = 2 \times 10^{14} m^{-3}$ and Case 2 with a free stream number density of $n_\infty = 2 \times 10^{17} m^{-3}$. In order to maintain a constant ambient mean free path of approximately 0.01 m at these densities, the reference diameters of the simulator particles used in the VHS molecular model are increased from the baseline values given in Table A.1 by a factor of $\sqrt{1 \times 10^6}$ in Case 1 and a factor of $\sqrt{1000}$ in Case 2. This modification is made in order to maintain a shock layer structure similar to that produced by the FIRE II vehicle at 85 km. The constancy of the mean free path in the two shock layer cases presented here means that the ratio of Debye length to mean free path of the plasma, λ_D/λ is lower in Case 2 relative to Case 1.

The chemical reaction rates used in the TCE chemistry model are increased from the baseline values given in Tables A.2 and A.3 by a factor of 5×10^5 in Case 1 and a factor of 5×10^2 in Case 2, to yield a degree of ionization close to that computed for the FIRE II 85 km trajectory point. In Case 2, the electron mass is increased by three orders of magnitude to yield a mass ratio of nitrogen ions to electrons, $\mathrm{m}_{N^+}/\mathrm{m}_e$, of 25.

Both Case 1 and Case 2 are computed using the reentry velocity of FIRE II of 11.37 km/s, labeled '1a,2a', as well as for a reentry velocity typical of a return trajectory from Mars, 13 km/s, labeled '1b, 2b'. The input parameters for all four

cases presented in this chapter are summarized in Table 5.1.

Table 5.1: Summary of simplified shock layer model parameters.

Property	Case 1a	Case 2a	Case 1b	Case 2b
Free stream number density	$2\times10^{14}m^{-3}$	$2\times10^{17}m^{-3}$	$2\times10^{14}m^{-3}$	$2\times10^{17}m^{-3}$
Free stream velocity	11.37 km/s	11.37 km/s	13 km/s	13 km/s
Free stream temperature	212 K	212 K	212 K	212 K
Free stream Mach number	39	39	45	45
Vehicle surface temperature	460 K	460 K	460 K	460 K
VHS d_{ref} multiplier	$\sqrt{1\times10^6}$	$\sqrt{1000}$	$\sqrt{1\times10^6}$	$\sqrt{1000}$
TCE reaction rate multiplier	5×10^5	5×10^2	5×10^5	5×10^2
m_{N^+}/m_e	unchanged	25	unchanged	25

5.3 Implementation of the One-Dimensional DSMC Method

The stagnation streamline of the flow is modeled as a constant area flow with one inlet boundary and a diffusely reflecting surface at the other boundary. Initially, an unsteady shock wave propagates from the inflow surface of the domain. At some point, the removal of particles commences from the sides of a region extending from the surface to a specified location, x_{remove}, such that the inlet and outlet mass fluxes are equal. In this way, a stationary shock is created in the simulation domain. The removal methodology described in Appendix B ensures that mass, momentum, and energy are conserved along the flow.

The one-dimensional DSMC method is implemented in MONACO as follows. The number density at which the removal will start, n_{shock} is specified for a cell in the computational domain, with its center located at x_{remove}, through an input file. The number density n_{shock} is one half the density rise across the shock being simulated, and the location x_{remove} is the center of the shock. These values are obtained from

an axisymmetric flow field calculation. At every iteration of the DSMC algorithm, the number density is computed in that cell and checked against the specified value. When the computed value exceeds the specified value, the particle removal procedure starts. However, the number density in the specified cell is still computed at each iteration. If it falls below the specified value, the particle removal is halted until it rises again.

Mass conservation is enforced on the basis of number flux of each type of atom that comprise the molecules, since the gas composition changes throughout the shock layer[7]. At each iteration of the simulation, the particle selection routine is repeated until the number of particles of a given species that have been removed from the domain is equal to the number that were introduced at the inlet boundary during that iteration of the simulation. This is done without regard to particle charge, that is, if two nitrogen particles are introduced into the domain at a given iteration in the form of a nitrogen molecule, then two nitrogen atoms, two nitrogen atomic ions, a nitrogen molecule, or a nitrogen molecular ion will be removed during the particle selection routine to conserve mass at that iteration of the simulation. Ambipolar diffusion is enforced in the direction normal to the stagnation streamline by requiring that an electron be selected for removal from the same cell each time an ion is removed from a given cell.

At each iteration, a particle is picked independently of location, from the cells downstream of x_{remove}. Since particle coordinates in MONACO are stored on a per cell basis, and the computational grids used in these simulations are not uniform, care must be taken to ensure that the particle is selected at random with respect to axial location in the grid. This is accomplished by first randomly selecting a cell downstream of x_{remove}, then using the acceptance-rejection technique[7] to keep the

cell based on the ratio of cell lengths $\Delta x_{selected}/\Delta x_{remove}$. The length of the selected cell, $\Delta x_{selected}$ will always be less than that of the cell at the start of the particle removal region, Δx_{remove}. This procedure accounts for the variation of particle number in the cells along the simulation domain and results in random selection of particles with respect to location. Next, a particle is chosen at random from the selected cell, and the acceptance-rejection technique is used again to remove the particle or keep it based on the square of its velocity component normal to the axial direction:

$$P_{remove} = \frac{\left(\sqrt{v^2 + w^2}\right)^2}{\left(V_{n,max}\right)^2}. \tag{5.2}$$

In Equation 5.2, v and w are the normal velocity components of the particle in question, and $V_{n,max}$ is a maximum normal velocity in the simulation that is stored on a per species basis. The maximum normal velocity is updated with the new largest value whenever $P_{remove} > 1$.

The particle removal routine is parallelized using the Open MPI libraries.

5.3.1 Method verification

In order to verify that the procedure for particle removal is performing as expected, the flow along the stagnation streamline of the FIRE II vehicle at the 85 km flight condition was simulated using the one-dimensional DSMC method. Figure 5.2 shows both the streamwise velocity and density distributions predicted using the 1D DSMC method, along with the results from the axisymmetric simulation presented in Section 3.6.1. The results agree quite well. Similarly good agreement is seen between the two results for other flow field parameters.

Figure 5.3 shows the total number of simulator particles in the domain during the one-dimensional simulation, as well as the total energy in the domain per kilomole.

Both parameters reach a steady state value, indicating that the particle removal procedure used in the one-dimensional DSMC method is conserving both particle number and energy as required.

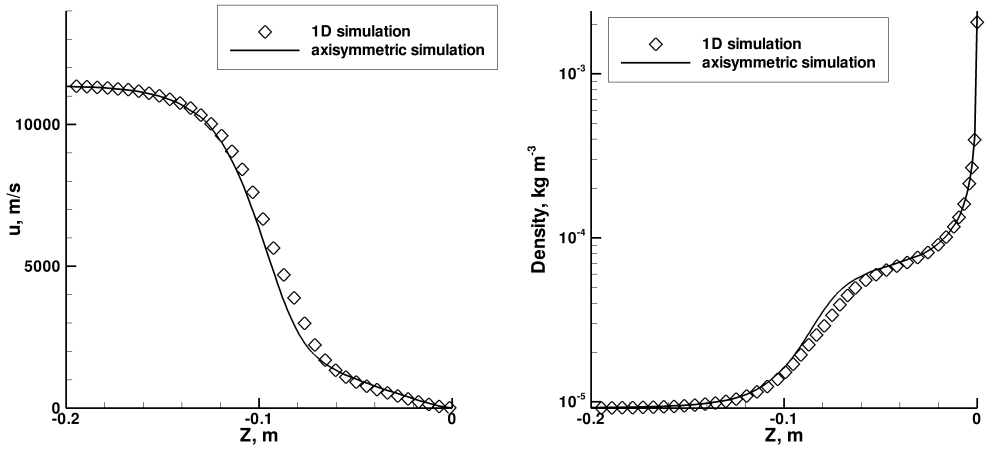

(a) Streamwise velocity component. (b) Density.

Figure 5.2: Comparison of 1D DSMC results to axisymmetric results for the FIRE II, 85 km fore body case.

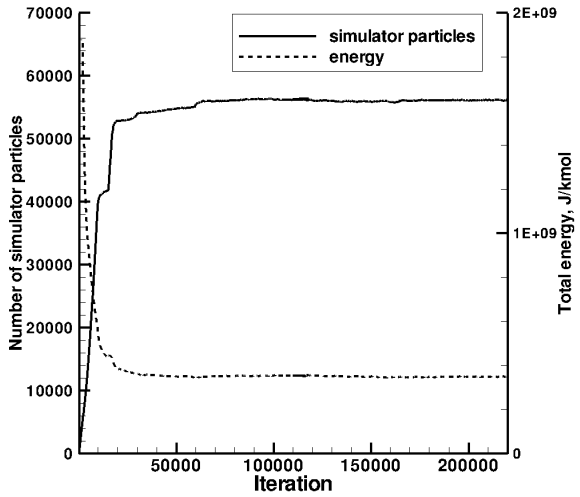

Figure 5.3: Total number of simulator particles and energy in the domain during the 1D DSMC calculation of the FIRE II, 85 km case..

5.4 Implementation of the Particle in Cell Method

The electrostatic Poisson equation governs the distribution of plasma potential in the shock layer,

$$\frac{d^2\phi}{dz^2} = -\frac{e}{\epsilon_o}\left(n_i - n_e\right), \tag{5.3}$$

where ϕ is the plasma potential, z is the coordinate in the free stream flow direction, n_i and n_e are the ion and electron number densities, e is the elementary charge, and ϵ_o is the permittivity of free space. This equation describes the potential distribution of a plasma in which the magnetic field does not vary with time. It is valid in these simulations because the shock layer flow field is analyzed as a steady-state phenomenon. The solution of Equation 5.3 is found on the same spatial grid used for the DSMC procedures. Equation 5.3 is discretized using the three point, central difference formula [65]

$$\frac{2}{\Delta z_{n+1} + \Delta z_n}\left[\frac{(\phi_{n+1} - \phi_n)}{\Delta z_{n+1}} - \frac{(\phi_n - \phi_{n-1})}{\Delta z_n}\right] = -\frac{e}{\epsilon_o}\Delta n_n. \tag{5.4}$$

This formula is second order accurate on a uniform grid, and the accuracy degrades as the disparity in adjacent cell lengths, Δz_{n+1} and Δz_n, increases. The resulting system of equations is solved using the Thomas Tridiagonal Matrix algorithm [66].

The number density of ions and electrons are resolved at each grid node using the Charge-in-Cloud (CIC) interpolation method[62]. The contribution of an ion particle m at location z_m, to the charge separation $\Delta n = n_i - n_e$ at node n with location z_n is given by:

$$\Delta n_n = +\frac{W_p}{V_{cell}}\frac{|z_m - z_n|}{\Delta z}. \tag{5.5}$$

Here Δz is the length of the cell that the particle is located in, V_{cell} is the cell volume, and W_p is the numerical weight of the particle. If the particle m is an electron, a negative contribution to Δn_n is made instead. Equation 5.5 is summed over all charged particles in the two cells adjacent to node n to compute the total charge separation at node n. This procedure is carried out for each node in the computational mesh.

The electric potential is differentiated to obtain the electric field at each node, again using a three point central difference formula

$$E_z = -\frac{1}{2}\left[\frac{\phi_{n+1} - \phi_n}{\Delta z_{n+1}} + \frac{\phi_n - \phi_{n-1}}{\Delta z_n}\right], \tag{5.6}$$

at the interior grid nodes. At the free stream boundary an upwind difference formula is used,

$$E_z = -\frac{\phi_{n+1} - \phi_n}{\Delta z_{n+1}}, \tag{5.7}$$

and at the boundary at the vehicle surface a downwind difference formula is used

$$E_z = -\frac{\phi_n - \phi_{n-1}}{\Delta z_n}. \tag{5.8}$$

The former is second order accurate on a uniform grid, and again the accuracy approaches first order as the disparity in adjacent cell lengths increases. Since the computational grid is strongly non-uniform in the near wall region of the domain, the accuracy of Equation 5.6 is not second order in that region, and the first order accuracy of the difference formulas used at the domain boundaries was deemed sufficient.

The value of electric field is interpolated to the locations of the individual particles

using the CIC method. The instantaneous electric field is assumed to remain constant during a simulation time step so that the average velocity of a charged particle during one iteration of the simulation is

$$u_p^{'} = u_p + \frac{1}{2}\Delta u_p \tag{5.9}$$

where u_p is the velocity of each simulator particle and a prime denotes the velocity used during the movement phase of the DSMC algorithm. At each time step, the velocity increment imposed on a particle due to its acceleration in the electric field is given by

$$\Delta u_p = \frac{q}{m} E_z \Delta t \tag{5.10}$$

where m is the particle mass, q is the particle's charge and Δt is the simulation time step. The velocity increment is added to the axial velocity component of each charged particle.

The DSMC and PIC modules are tightly coupled so that the PIC module is used to compute the electric field at each iteration of the DSMC module, and the PIC routines are parallelized using the Open MPI libraries. At the inlet boundary, a field-free boundary condition of $\frac{d\phi}{dz} = 0$ is imposed. The boundary condition for the solution of the potential field at the vehicle surface is fixed at $\phi = 0$ V, and current is permitted to flow to the surface.

5.4.1 Parameter sensitivity study

Many simulations of Case 1a are carried out to determine the sensitivity of the results to a number of computational parameters. Figure 5.4(a) shows the predicted electric field along the stagnation streamline for four different values of $\lambda_D/\Delta x$. A

magnified view of the sheath region is shown as the results do not vary appreciably in the bulk plasma region. A value of $\lambda_D/\Delta x = 5$ yields a grid independent solution. Note that for this low density Case, stable simulation results are obtainable with values of $\lambda_D/\Delta x < 5$, although this is found not to hold true for the conditions of Case 2.

Figure 5.4(b) shows the sensitivity of the predicted electric field results to the length of the transient period of the simulation. The transient period refers to the number of DSMC-PIC iterations performed before sampling of the flow field is started. It is measured here in terms of ion transit time, the amount of time it takes the average ion particle to traverse the length of the simulation domain. Based on these results, a value of seven ion transit times is used for the minimum length of the transient period in DSMC-PIC simulations carried out in this thesis.

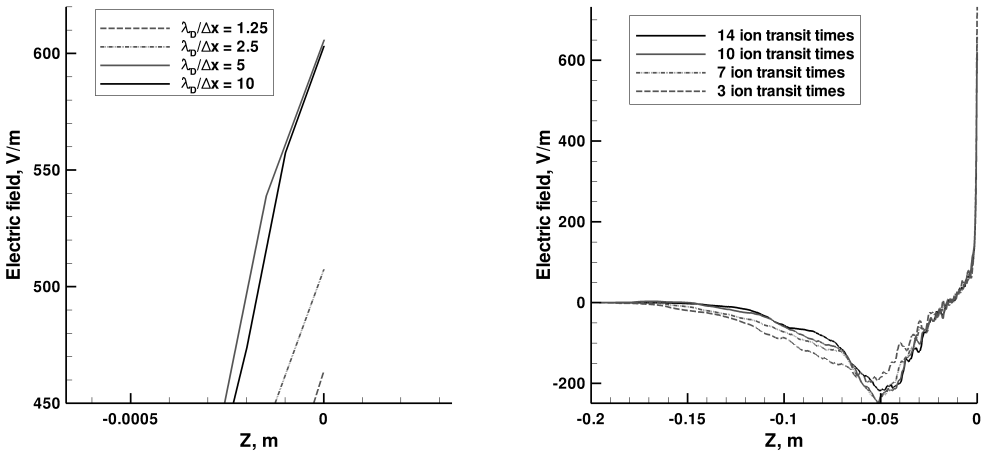

(a) $\lambda_D/\Delta x$. (b) Length of simulation transient period.

Figure 5.4: Sensitivity of Case 1a DSMC-PIC simulation results to various computational parameters.

Figure 5.5 shows the predicted electric field along the stagnation streamline for four different values of N_p. The value N_p refers to the maximum number of simulated

electron particles in the shock layer, and occurs in the bulk plasma region, between the vehicle surface and the shock front. A value of $N_p = 20$ is chosen to provide a compromise between computational expense and simulation accuracy.

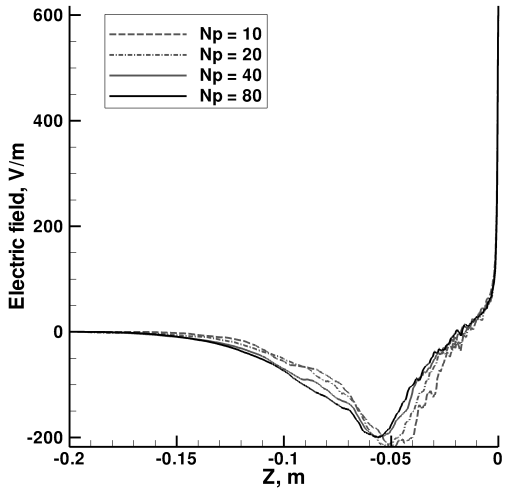

Figure 5.5: Sensitivity of Case 1a DSMC-PIC simulation results to number of simulated electron particles.

5.5 Results

The computational grids used for Case 1 and Case 2 have 500 and 16 000 cells, respectively. Each grid is constructed in such a way that a ratio of approximately $\lambda_D/\Delta \mathrm{x} = 5$ is satisfied at each cell in the domain. In some regions of the domain the cells are much smaller than a mean free path due to this requirement. This is illustrated in Figure 5.6, which shows the Debye length and mean free path along the stagnation streamline for both Case 1a and Case 2a. The character of the Debye length near the vehicle surface differs significantly between the two Cases, a direct result of the variations in electron number density and translational temperature in this region between the two Cases. Profiles of these variables are shown in Sections

5.5.1 and 5.5.2. The time step is dictated by the minimum cell crossing time of the electron particles, which is much less than the plasma period. This is illustrated in Figure 5.7, which shows the plasma period and the mean collision time along the stagnation streamline for Case 1a and Case 2a, as well as the time step used for each simulation. The mean cell crossing time of the electrons shown on these figures is computed using the root-mean-square speed of the electrons, $\sqrt{3kT_e/m_e}$, and is the limiting factor in determining the time step. However, to ensure stability, the actual simulation time step must be smaller than this time due to the presence of faster electrons at the tail of the electron velocity distribution function. Thus, simulation time step is on the order of 1×10^{-11} seconds for the simulations presented here and is the same for the electrons and heavy particles.

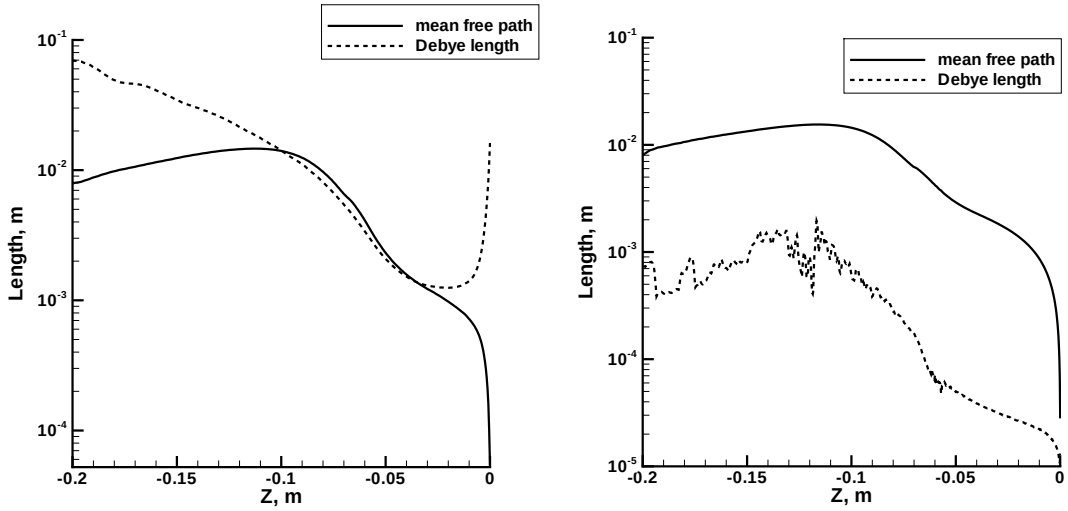

(a) Case 1a.

(b) Case 2a.

Figure 5.6: Debye length and mean free path along the stagnation streamline for Case 1a and Case 2a.

The weight factor of the simulator particles is selected to yield approximately 20 charged particles per cell in the peak plasma density region. The total number of simulated particles varies from 300 000 to 3 000 000 in these simulations. The

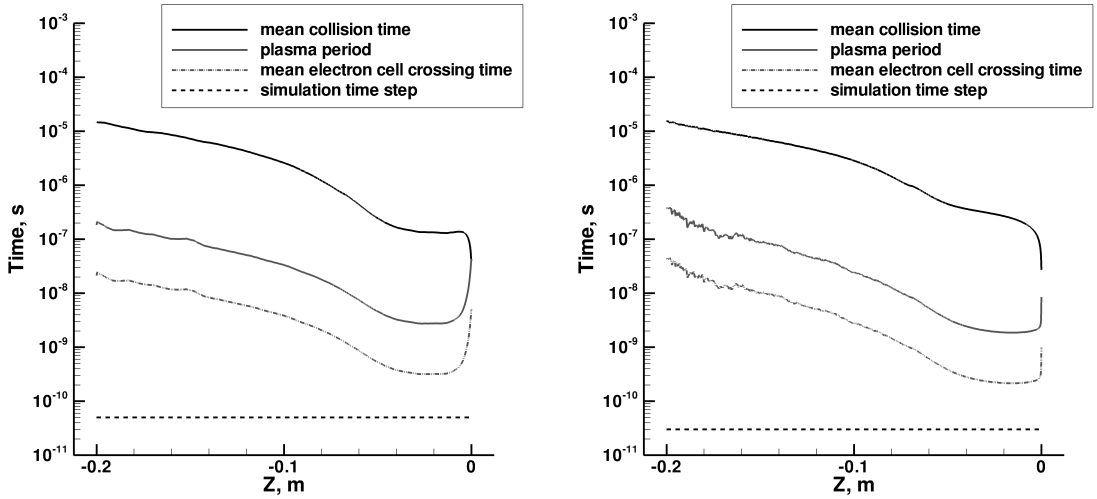

(a) Case 1a.

(b) Case 2a.

Figure 5.7: Characteristic time scales along the stagnation streamline for Case 1a and Case 2a.

simulation has converged when the number of simulator particles in the domain and the total energy in the domain reach a steady state. An example of one such convergence history is shown in Figure 5.8(a). The current flowing to the wall was also monitored during the simulations to ensure that it had reached a steady value before the sampling interval was started. This was an approximate assessment of simulation convergence due to the large amount of scatter in the instantaneous current result, as shown in Figure 5.8(b). The simulations for Cases 1 and 2 require 6 000 000 and 18 000 000 time steps to reach steady state, respectively. Once a steady state is reached, a minimum of 100 000 sampling iterations are performed. The total simulation time for the DSMC-PIC simulations ranges from approximately 60 wall hours to 400 wall hours.

Simulations 1a and 1b are run on 4 processors, and simulations 2a and 2b are run on 15 processors. Figure 5.9 illustrates the computational performance of the 1D DSMC and DSMC-PIC methods. Shown on this figure is the speed up relative

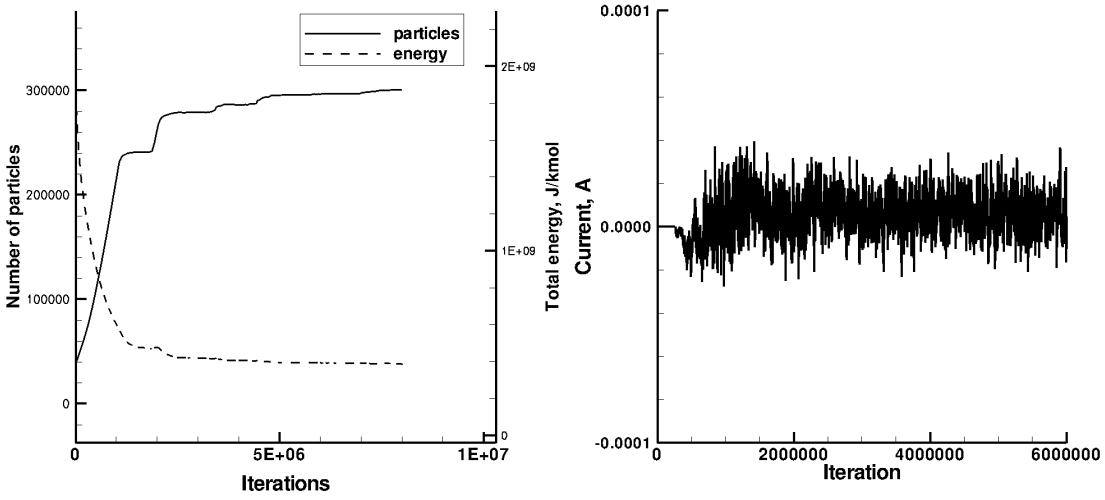

(a) Particle number and total energy. (b) Instantaneous current at stagnation point.

Figure 5.8: Convergence history for Case 1a.

to the ideal obtained from Case 2a during 10 000 iterations in the middle of the transient period. Also shown on the figure is the speed up from a 2D simulation that utilizes the same free stream and boundary conditions as Case 2a, using the distribution version of the MONACO code. The computational performance of both the 1D DSMC and the DSMC-PIC codes falls off quickly at about 15 processors, however the performance of MONACO does as well. This is due to the computational overhead inherent in passing simulator particles between cells located on different processors, and there is clearly an optimum number of simulator particles per processor after which the performance degrades. The difference between the speed up of the MONACO, 1D DSMC and DSMC-PIC results is a measure of the computational overhead associated with the particle removal routine and the PIC routines.

5.5.1 Results for a Lunar return trajectory (Case 1a and 2a)

The general character of the shock layer plasma is illustrated in Figures 5.10 and 5.11. These figures show the distribution of species mole fractions computed using

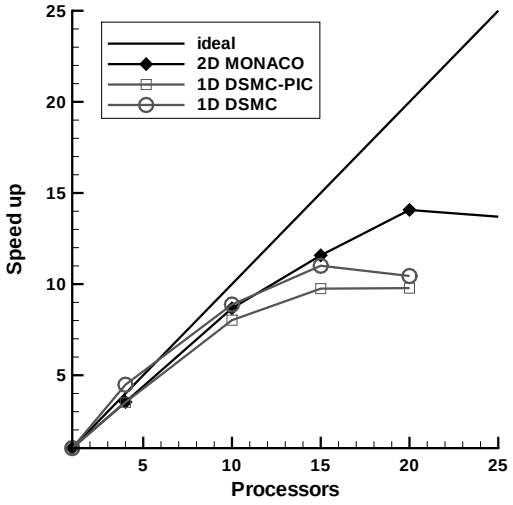

Figure 5.9: Computational performance of the 1D DSMC and DSMC-PIC codes.

the DSMC technique with the baseline electric field model for both Case 1a and the actual FIRE II 85 km flight condition from Section 3.6.1. The concentrations of NO, O_2^+ and O^+ are very small and these species are omitted from Figures 5.10 and 5.11 for clarity. The flow direction is from left to right and the stagnation point of the flow at the vehicle surface is located at z = 0 m. For Case 1a, the air begins to rapidly dissociate at a distance of approximately 0.07 m from the stagnation point, indicating the location of the shock and the start of the shock layer. Beyond this point the flow is composed predominantly of atomic nitrogen and oxygen. The degree of ionization reaches a maximum of 1.5% at approximately 0.04 m from the stagnation point, and then decreases towards the vehicle surface.

The location of the shock in Case 1a is closer to the vehicle than that predicted for the FIRE II, 85 km case, as indicated by the relative shift in the profiles of species mole fractions shown in Figures 5.10 and 5.11 for the two cases. However, the similarity of the shock layer structure between Case 1a and the FIRE II results indicates that the shock layer plasma examined in this study is representative of that

formed during the reentry of the FIRE II vehicle into the Earth's atmosphere.

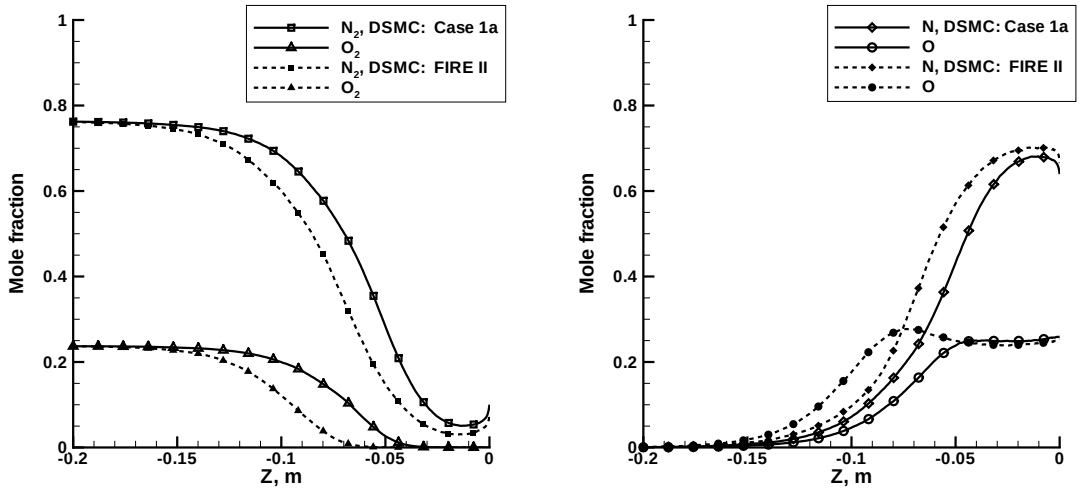

(a) Neutral molecules (b) Neutral atoms

Figure 5.10: Mole fractions of neutral species along the stagnation streamline for Case 1a and for actual FIRE II 85 km conditions.

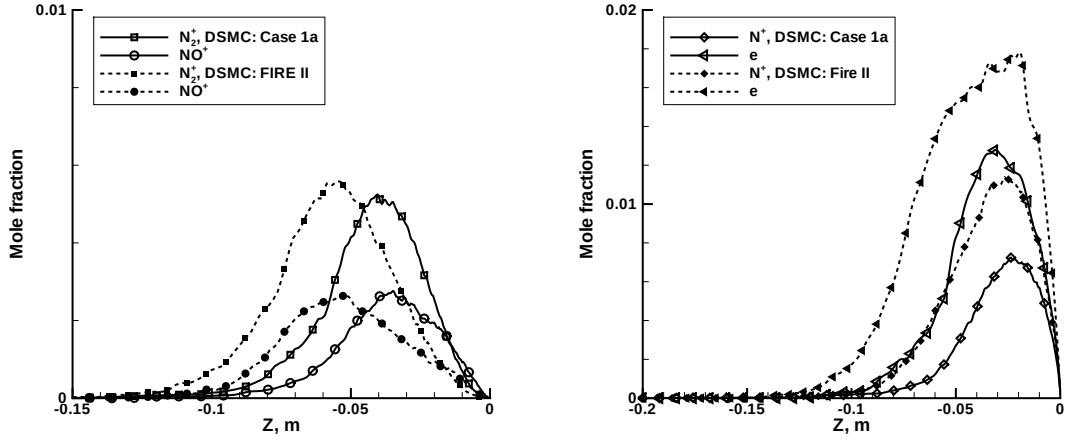

(a) Molecular ions (b) Atomic nitrogen ions and electrons

Figure 5.11: Mole fractions of charged species along the stagnation streamline for Case 1a and for actual FIRE II 85 km conditions.

Structure of the electric field

Figure 5.12(a) shows the electric and potential fields from the DSMC-PIC simulation of the shock layer for Case 1a. The ambipolar electric field in the bulk plasma region is of negative polarity with a peak magnitude of approximately 130 V/m. The strong electric field near the vehicle surface in the plasma sheath reaches a peak value of approximately 1700 V/m. As the plasma density decreases, the charge separation is insufficient to maintain the electric field. It gradually decreases from the peak negative magnitude in the bulk plasma region to a value of zero at the free stream boundary of the simulation. The electric field is negative in the bulk plasma region to restrain the electrons and maintain plasma quasi-neutrality. Near the vehicle surface, the role of the strong positive electric field is to moderate the flux of electrons to the vehicle surface.

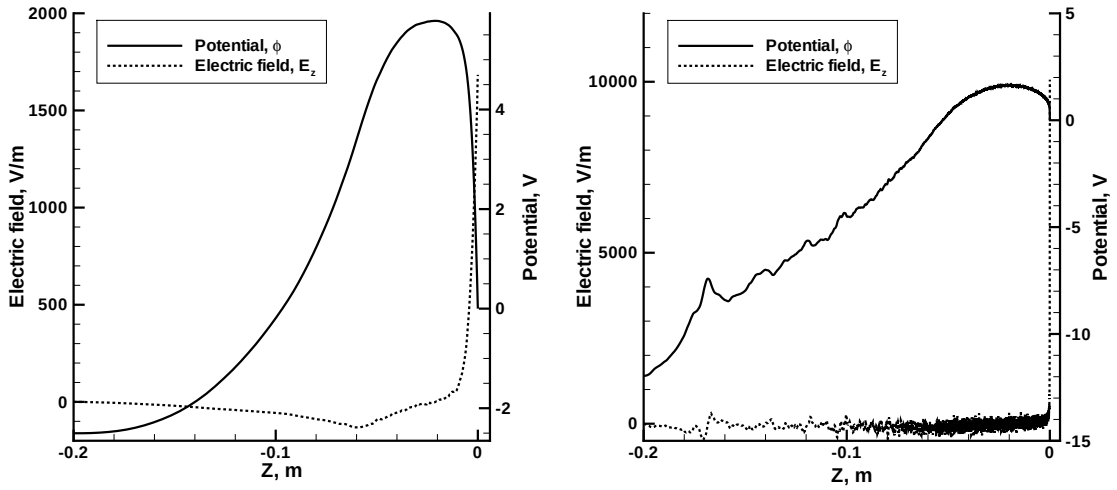

(a) Case 1a.

(b) Case 2a.

Figure 5.12: Electric and potential fields for a Lunar return entry.

Figure 5.12(b) shows the electric and potential fields from the DSMC-PIC simulation of the shock layer for Case 2a. Here, the mass of the electrons is increased so

that $m_{N^+}/m_e = 25$. The electric field data has substantially more statistical scatter in this case. While the mean free path of the plasma remains the same in both Cases, the ambient density has increased in Case 2a. This means that the simulator particles must be assigned larger weight factors in Case 2a; that is, each simulator particle represents more real particles. This fact leads to the increased level of scatter in the plasma potential calculation, as small fluctuations of charge density are magnified by a larger particle weight factor. This scatter is further amplified by differentiating the plasma potential to obtain the electric field on a finer grid than that for the Case 1a simulation.

The mean of the electric field in the bulk plasma region in Case 2a is approximately -130 V/m, not substantially different from the previous result. An approximate expression for the ambipolar electric field is found by differentiating the Boltzmann relation for the electrons[67]

$$E_{z,ambipolar} = -\frac{kT_e}{e}\frac{d[\,ln(n_e)]}{dz} \tag{5.11}$$

where, for convenience, the electrons are assumed to be isothermal. Neglected in this equation are the electron inertial force and frictional drag terms. These assumptions become weaker in Case 2a because these terms are proportional to the particle mass, and the mass of the electron particle is artificially increased in Case 2a. However, the qualitative character of the electric field in the ambipolar region can still be assessed using this expression. Equation 5.11 shows that the ambipolar electric field varies with the gradient of the natural logarithm of electron density and thus has only a weak dependence on the plasma density. This explains the small difference in the magnitude of the electric field in the bulk plasma regions of the two Cases. Near the surface, however, the electric field in the plasma sheath is substantially larger in

Case 2a, reaching a peak value of just over 10 000V/m. The use of artificially heavy electrons in this simulation results in a smaller potential gradient in the sheath. However, the Debye length and therefore the sheath width, has also decreased in this case. The result is an overall increase in the magnitude of the electric field at the vehicle surface.

The electric field in the free stream region is non-zero in this Case because there is sufficient charge separation to maintain the field. Unfortunately, it is not possible to comment on any additional structure in the electric field in this region due to the large amount of statistical scatter in the results.

Velocity and temperature distributions

The strongest assumption made when using the standard ambipolar diffusion model is that the electrons move with the same average velocity as the ions. Figure 5.13 shows the average velocities of the charged species along the stagnation streamline computed using both the DSMC-PIC approach and the baseline DSMC approach for Case 1a. The DSMC-PIC results show that the average velocity of the electrons is negative in the region upstream of the shock and is not equal to the average velocity of the ions there. Electron particles are restricted to travel in the direction of the average ion velocity in the baseline electric field model, and the average ion velocity is positive throughout the domain. For this reason, the region upstream of the shock contains very few electron particles in the DSMC simulation, as the electrons that are created in the shock layer are constrained to travel towards the surface of the vehicle. This produces a large amount of statistical scatter in the DSMC result for electron velocity in the region upstream of the shock.

In the shock layer, the DSMC-PIC approach predicts a lower average ion velocity

than the standard DSMC approach because the ions are decelerated by the negative electric field in this region. The average velocity of the ions increases as they travel towards the wall and are accelerated by the strong positive electric field in the sheath. Very close to the vehicle surface, the ion velocity begins to decrease due to the collisionality of the sheath. Figure 5.6(a) shows the mean free path and Debye length throughout this shock layer. Near the vehicle surface, the mean free path is less than the Debye length, meaning that the sheath in this case is collisional. The average velocity of the electrons increases strongly near the vehicle surface for two reasons. The vehicle surface acts as a sink to electrons, so there are very few electrons in this region with negative velocity. Secondly, the majority of electrons do not possess sufficient energy to traverse the potential drop in the sheath. Those that do reach the vehicle surface are at the tail of the electron energy distribution function and have very high energies.

Similar trends are observed in Case 2a with the exception of the abrupt decrease in ion velocity in the sheath. The sheath in Case 2 is not in the collisional regime, as indicated by the separation of the mean free path and Debye length scales shown in Figure 5.6(b).

Figure 5.14(a) shows the translational, rotational, vibrational and electron translational temperatures along the stagnation streamline for Case 1a. The strong degree of thermal nonequilibrium in this flow field is illustrated by the differences in the mode temperatures. The electron temperature distribution throughout the shock layer is predicted to be nearly isothermal with the DSMC-PIC approach, in contrast to the results given by the baseline DSMC approach. The electron temperature obtained upstream of the shock with the DSMC-PIC approach is greater than that obtained with the baseline DSMC approach because the electrons are not constrained

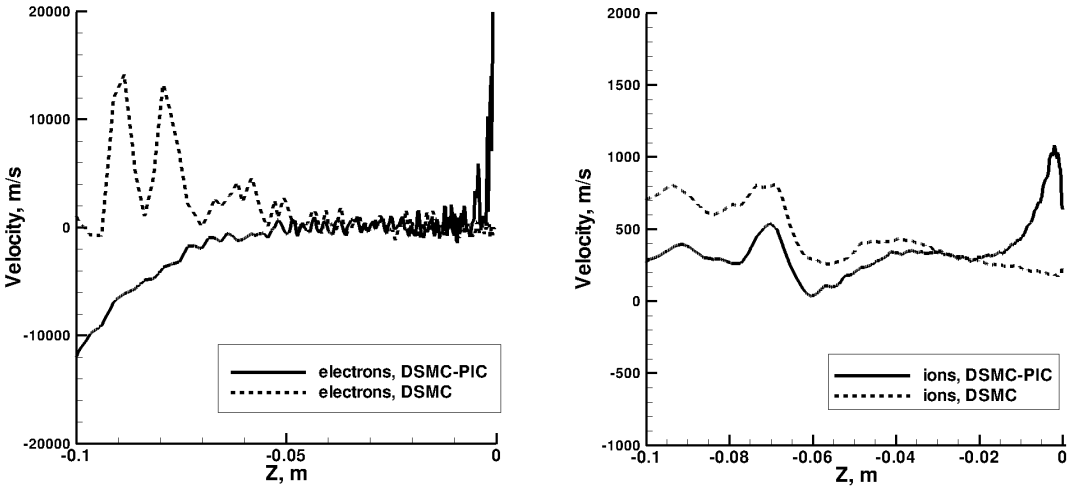

(a) Electrons

(b) Ions

Figure 5.13: Average velocity of charged species along the stagnation streamline for a Lunar return entry (Case 1a).

to move with the ions in the DSMC-PIC model, and can travel into this region. The electrons that manage to traverse the ambipolar electric field in this region without having their direction of travel reversed are those with large negative velocity components, however, the distribution function in the region upstream of the shock is still close to a Maxwellian, as shown in Figure 5.15. In the sheath region, the electrons are decelerated by the electric field and very few reach the vehicle surface to recombine. The majority of electrons have their direction of travel reversed, broadening the velocity distribution function and leading to a temperature that is again greater than that predicted by the baseline DSMC approach.

The mode temperatures along the stagnation streamline from Case 2a are shown in Figure 5.14(b). Due to the increased mass of the electrons in this simulation, their collisionality has decreased and the electron translational temperature does not equal the rotational and vibrational temperatures upstream of the shock in the DSMC results. Similarly, the translational temperature increases with increasing distance

from the shock front in the DSMC-PIC results, rather than becoming isothermal as in Case 1a. The broadening effect of the velocity distribution function in the sheath is not as significant. This is because the use of artificially heavy electrons in Case 2a results in a smaller potential drop in the sheath and fewer electrons are reflected.

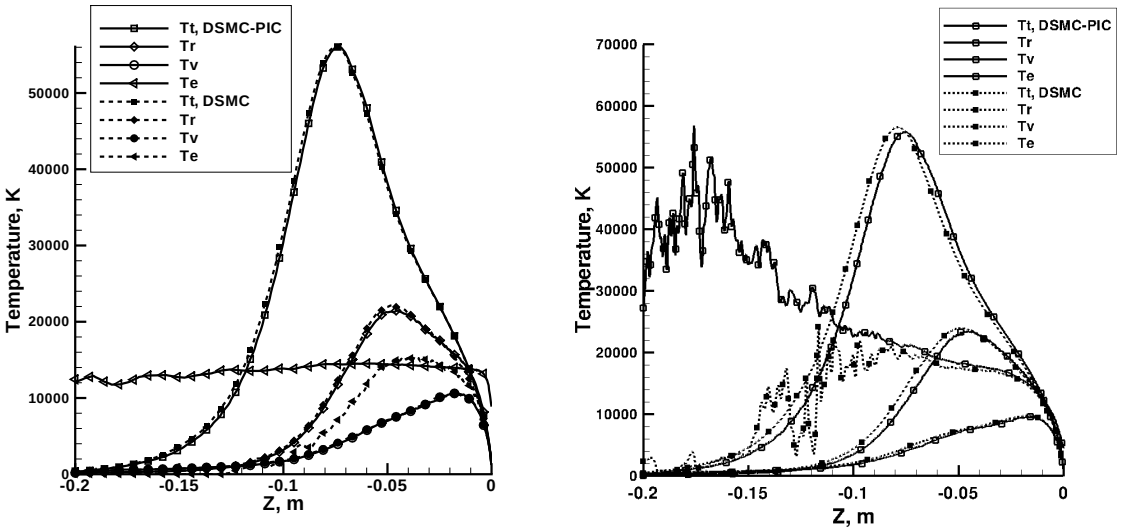

(a) Case 1a.

(b) Case 2a.

Figure 5.14: Temperatures along the stagnation streamline for a Lunar return entry.

Plasma density distribution

Figure 5.16 shows the number density of electrons and ions predicted by the rigorous DSMC-PIC and the baseline DSMC modeling approaches for Case 1a. In the region upstream of the shock layer, the DSMC-PIC approach predicts an increase relative to the results obtained with the baseline DSMC approach in both the ion and the electron number density. In this region, the charge separation, shown in Figure 5.17(a), is no longer large enough to create an electric field sufficient to restrain the electrons, and the flow transitions to free diffusion. The DSMC-PIC approach predicts a decrease in both the ion and electron number density in the sheath region as shown in Figure 5.16 and more clearly in Figure 5.17(b), except very near the wall

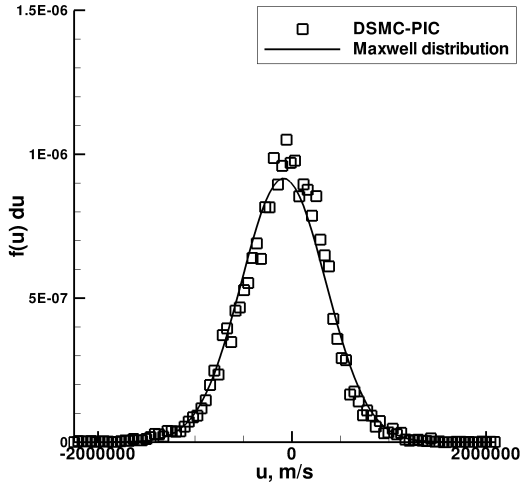

Figure 5.15: Velocity distribution function of electrons at z = -0.15 m for a Lunar return entry (Case 1a).

where the number density of the ions peaks abruptly. This phenomenon is due to the collisionality of the sheath. Ions at this point in the sheath have experienced at least one collision, which causes a decrease in the macroscopic average ion velocity, as shown in Figure 5.13. In order to enforce species continuity, the number density of ions correspondingly increases in this region.

The density of charged particles and charge separation in the shock layer obtained for Case 2a are shown in Figures 5.18 and 5.19(a). Figure 5.19(b) shows the distribution of charged particles in the plasma sheath for this case. The trends in particle density seen in these results are similar to those observed in Case 1. In this Case, however, the charge separation is sufficiently large to produce a non-zero electric field in the free stream region. The sheath region in this model is thinner and is not collisional, due to the decrease in the Debye length. Additionally, the magnitude of charge separation in the sheath is only 4% of the free stream density, whereas for Case 1a it is 15% of the free stream density. Again this is because the

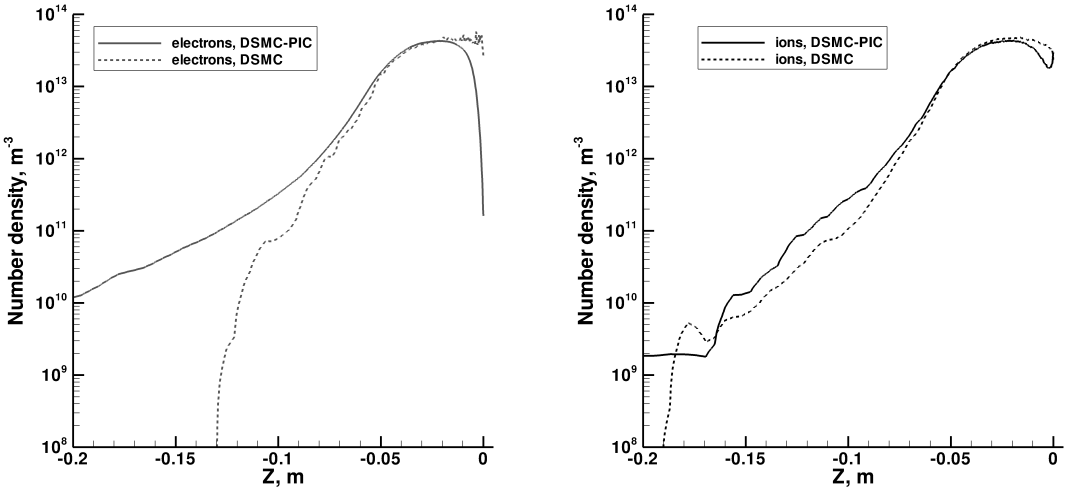

(a) Electrons (b) Ions

Figure 5.16: Number density of charged species along the stagnation streamline for a Lunar return entry (Case 1a).

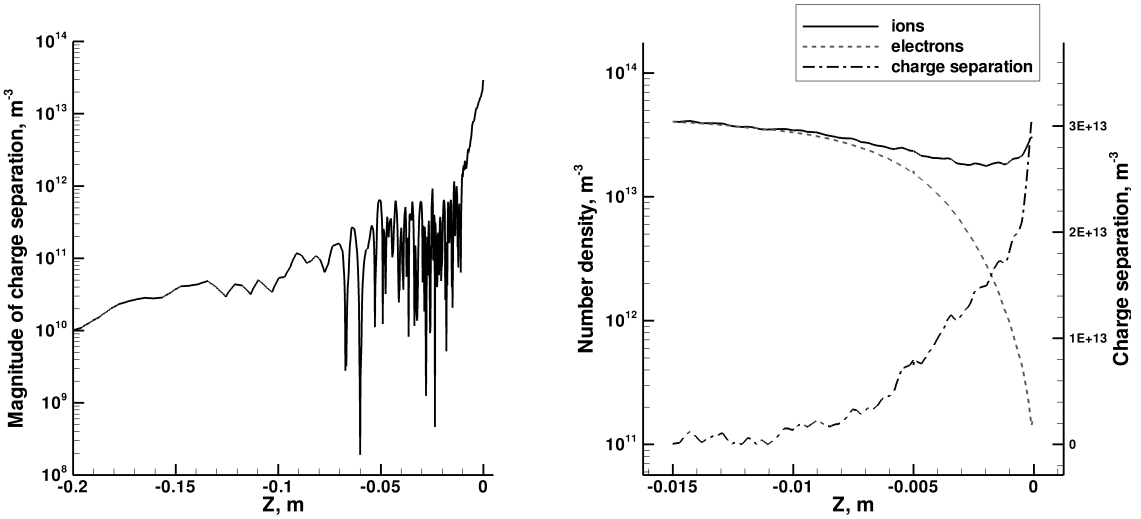

(a) Charge separation along the stagnation streamline. (b) Magnified view of the sheath region.

Figure 5.17: Number density of charged species and charge separation for a Lunar return entry (Case 1a).

potential drop in the sheath in Case 2a is much smaller than that of Case 1a, due to the larger mass of the electrons.

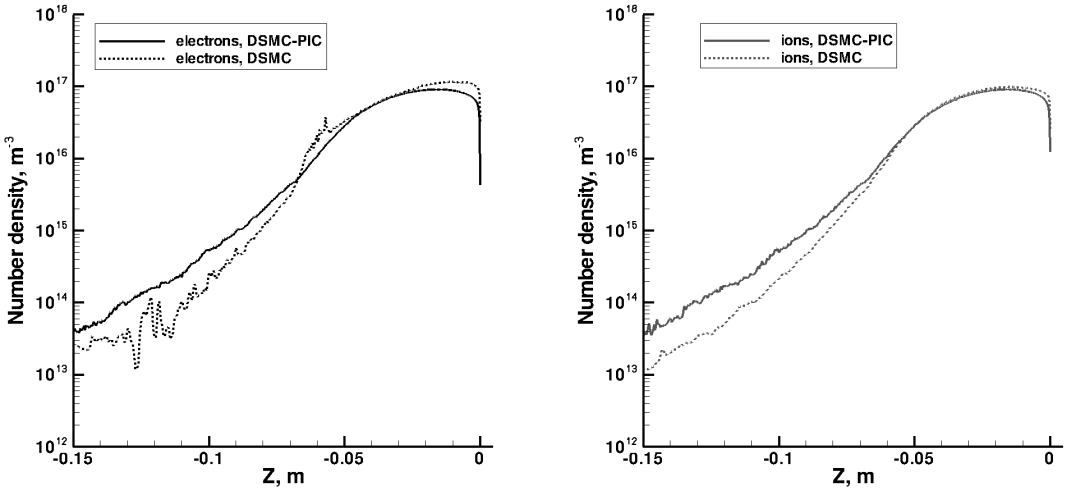

(a) Electrons (b) Ions

Figure 5.18: Number density of charged species along the stagnation streamline for a Lunar return entry (Case 2a).

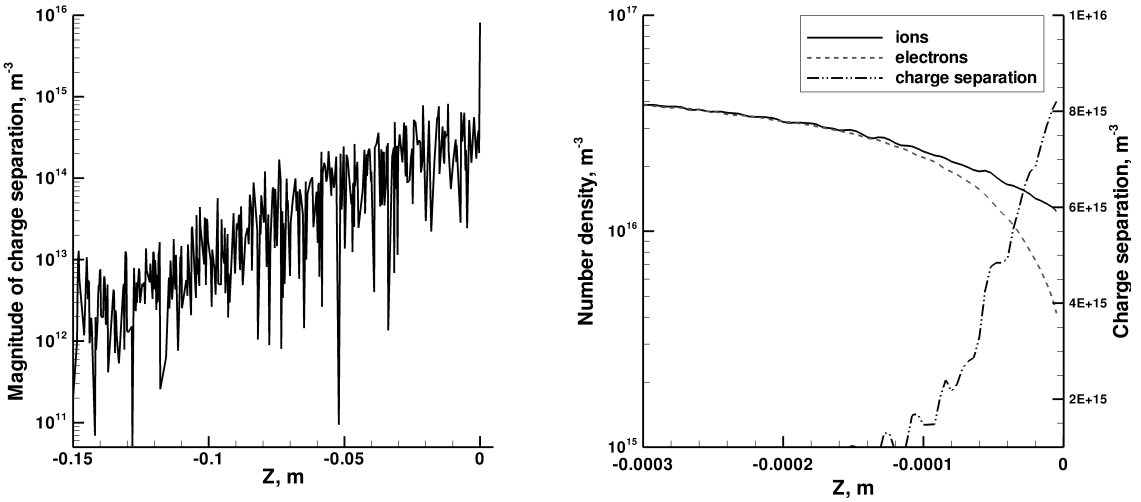

(a) Charge separation along the stagnation streamline. (b) Magnified view of the sheath region.

Figure 5.19: Number density of charged species and charge separation for a Lunar return entry (Case 2a).

Surface heat flux results

The most useful way to examine the convective heat flux results from these simulations is to directly compare the contributions from individual species. Figures

5.20(a) and 5.20(b) give the contribution of convective heat flux computed using the DSMC-PIC and baseline DSMC approaches for the following species: N_2, N, O, NO^+, N^+ and O^+. These species comprise the majority of the total convective heat flux at the vehicle surface. The total convective heat flux computed using each approach is also shown on these figures. The predicted convective heat flux is much lower in these Cases than the values for the actual FIRE II flight conditions presented in Chapter III. This is because the free stream number density used in these Cases is significantly lower than the actual value in the Earth's atmosphere at an altitude of 85 km. The error bars on Figure 5.20(a) represent the 1σ statistical error on the heat flux calculation. The statistical error on the total heat flux result is $\pm 3\%$. Since approximately the same number of heat flux samples are collected during the simulations of the other Cases, one can expect a similar level of relative statistical error on the heat flux calculation in those results as well.

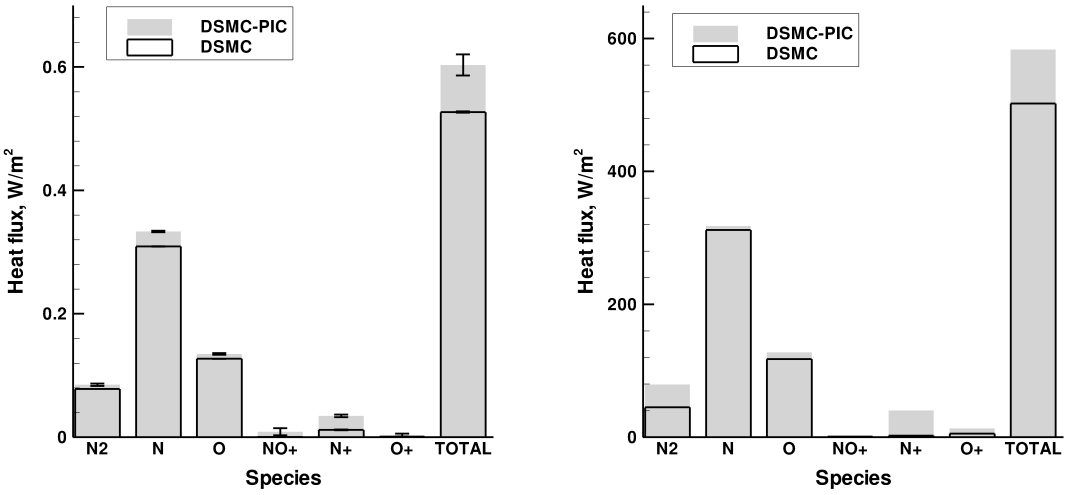

(a) Case 1a.

(b) Case 2a.

Figure 5.20: Convective heat flux at the vehicle surface, separated by species, for a Lunar return entry.

The baseline DSMC approach under-predicts the convective heat transfer at the

vehicle surface by 14% for Case 1a and by 16% for Case 2a. This difference is due in part to an increase in the contribution from the dominant atomic nitrogen ion in both shock layers when the rigorous DSMC-PIC approach is used. The increase in ion heat flux is larger than would be predicted by merely including the electric potential energy, $e\phi$, gained by each ion as it traverses the potential drop in the sheath. Because the ions are accelerated in the shock layer by the electric field, their residence time in the shock layer decreases. This leads to an increase in the flux of ions that reach the vehicle surface, as fewer ions are transported radially away from the stagnation region. This phenomenon is illustrated in Figure 5.21, which shows the ion flux along the shock layer predicted by the DSMC-PIC approach as well as the baseline DSMC result for Case 1a and Case 2a. The effect of the increase in ion flux on the heat transfer to the vehicle surface is magnified due to the recombination of ions on the surface, resulting in an additional heat release. The increased contributions to convective heating by the N_2, N and O atoms is also related to acceleration of ions in the electric field, as these neutral species are gaining energy in collisions with the accelerating ions as they travel toward the vehicle surface.

5.5.2 Results for a Mars return trajectory (Case 1b and 2b)

The increase in the free stream velocity in these cases means that more translational energy is available to be transferred to the internal energy modes of the molecules, and to be used in chemical reactions downstream of the bow shock. Thus, a larger percentage of the gas in the shock layer is ionized than in the previous Cases. This is illustrated in Figure 5.22, which shows a comparison of the mole fraction of electrons from the DSMC-PIC result for both the 1a and 1b Cases. The degree of ionization of the flow is almost doubled in the Case 1b.

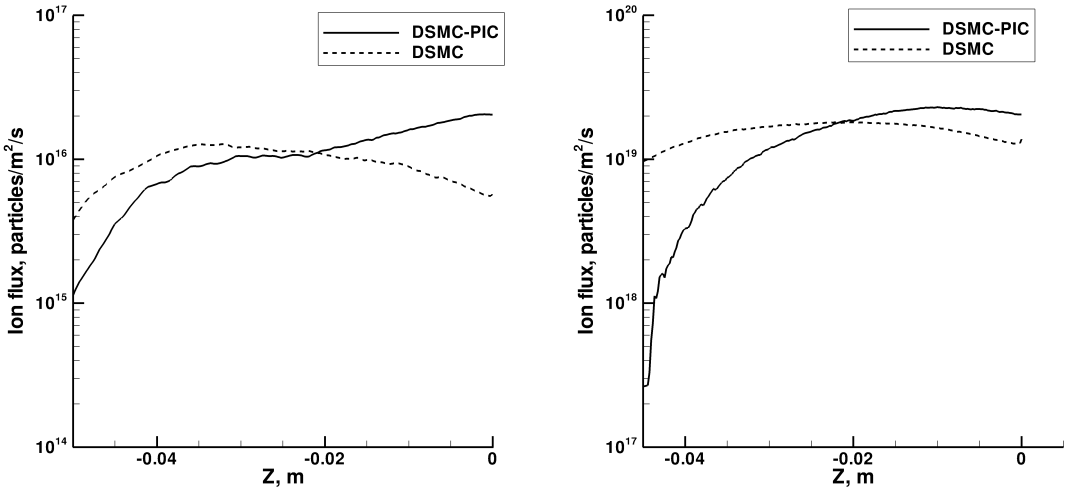

(a) Case 1a.

(b) Case 2a.

Figure 5.21: Ion flux in the shock layer near the vehicle surface for a Lunar return entry.

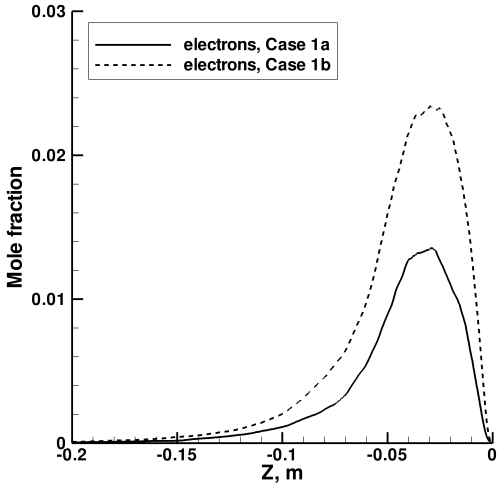

Figure 5.22: Mole fraction of electrons along the stagnation streamline predicted by DSMC-PIC for a Mars return entry.

Figure 5.23(a) shows the temperatures along the stagnation streamline from the baseline DSMC results and the DSMC-PIC results. The peak translational temperature has increased to approximately 70 000 K in these simulations, and the use of

the DSMC-PIC technique results in the same trends in electron temperature that are seen in Case 1a. The electron translational temperature is increased to approximately 16 000 K in the bulk plasma region, which causes an increase in the potential drop across the sheath relative to Case 1a. This is illustrated in Figure 5.23(b), which compares the electric and potential fields for Case 1a and Case 1b.

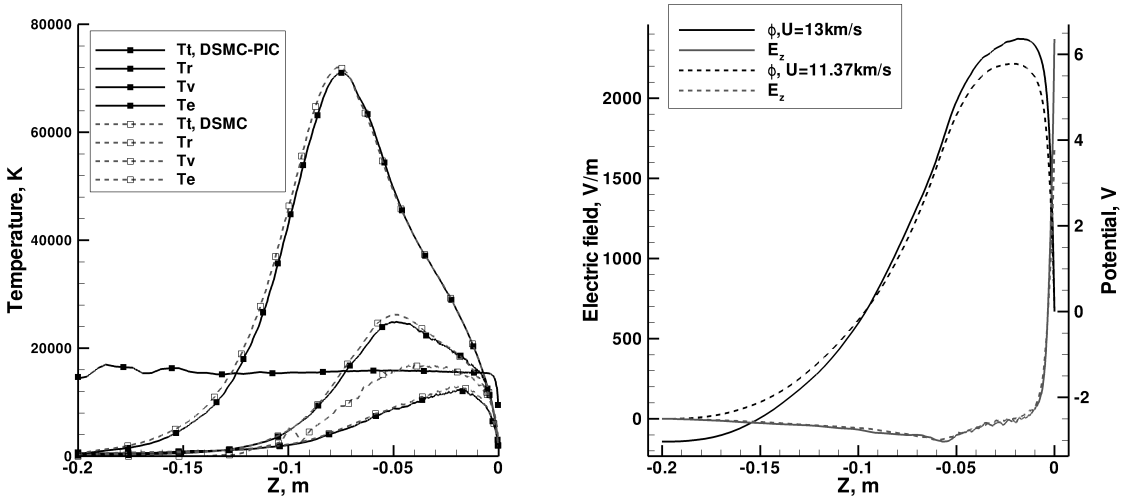

(a) Mode temperatures along the stagnation streamline.

(b) Electric and potential fields along the stagnation streamline.

Figure 5.23: Flow field results for a Mars return entry (Case 1b).

The results for Case 1b produced using the DSMC-PIC method predict a 14% increase in the convective heat flux to the vehicle surface relative to the baseline DSMC result; those for Case 2b predict a 28% increase. On first glance, one might expect that the DSMC-PIC simulations would predict a larger increase in the heat flux in Cases 1b and 2b relative to that predicted in Cases 1a and 2a, because the flow fields in the former Cases contain a larger number of charged particles that are acted on by the electric field. However, the results presented here indicate that this is at least not universally the case, a testament to the complex nature of the interactions between charged and neutral particles in these types of flows.

Rather than repeat all of the results for flow field parameters that have already been presented from the simulations of Cases 1a and 2a, it suffices to say that the trends observed in those Cases when the DSMC-PIC method is used are repeated in Cases 1b and 2b. These trends are:

- an increase in electron translational temperature in the sheath and free diffusion regions,
- a decrease in both the electron and ion densities in the sheath region, and an increase in both the electron and ion densities in the free diffusion region,
- an increase in convective heat flux to the vehicle surface.

Table 5.2 summarizes the convective heating results for each of the four Cases presented in this chapter. The DSMC-PIC results from the simulations of Cases 1a and 1b are used in the following chapter to develop an improved approximate electric field model for the simulation of rarefied reentry flows.

Table 5.2: Summary of heat flux results for Cases 1 and 2.

Case	Heat flux, DSMC	Heat flux, DSMC-PIC	Increase
1a	0.527 W/m^2	0.603 W/m^2	14%
1b	0.995 W/m^2	1.14 W/m^2	14%
2a	5.02×10^2 W/m^2	5.83×10^2 W/m^2	16%
2b	8.69×10^2 W/m^2	11.2×10^2 W/m^2	28%

5.6 DSMC-PIC Simulation of the Actual FIRE II 85 km Flight Condition

The computational expense of completing a simulation of the actual FIRE II, 85 km flight condition is estimated from the computational expense of the Case 2a

simulation at $U_\infty = 11.37\ km/s, n_\infty = 2 \times 10^{17} m^{-3}$. A threefold increase in free stream density is required to reach the necessary flight condition, which in turn requires a decrease in cell size by a factor of $\sqrt{1000}$ in order to scale the mesh on the Debye length of the flow. As a result, the cell transit time for an electron decreases by a factor of $\sqrt{1000}$, resulting in an overall factor of 1000 increase in computing time from that of the $2{\times}10^{17} m^{-3}$ free stream simulation. Lastly, the restoration of the electron mass from the artificial value of $m_e = 1000 \times m_e$ used in Case 2a results in an increase in the electron thermal velocities by a factor of $\sqrt{1000}$, therefore introducing an additional factor of $\sqrt{1000}$ increase in computational time. The Case 2a simulation presented here required 345 wall hours on 15 processors, or approximately 5000 CPU hours. Based on this and the aforementioned analysis, an estimate of the computational burden of a DSMC-PIC simulation of the FIRE II 85 km flight condition is approximately 6 600 000 CPU days. Implicit in this estimate is that the overhead associated with parallel processing is the same as that in the Case 2a simulation, stated another way, that the number of particles per processor remains the same. Since the number of cells in the domain will increase by a factor of $\sqrt{1000}$ for the actual FIRE II computation, the number of simulator particles will as well. Thus, the above estimate assumes that $15 \times \sqrt{1000} = 475$ processors are used for the calculation, giving a wall time of approximately 14 000 days, or 38 years.

The computational requirements could be reduced by parallelizing the code for use with a shared memory system. This would increase the parallel efficiency of the particle removal algorithm used to compute the 1D simulation. Additionally, the efficiency of the matrix inversion algorithm used to solve the electrostatic potential equation could be improved. Lastly, using smaller particle weight factors for the trace charged species would decrease the computational requirements by as much

as an order of magnitude. The use of individual weight factors for trace species in simulations involving chemical reactions is a current area of research in the DSMC community. However, none of these improvements would reduce the computational expense enough to allow the DSMC-PIC technique to be a viable modeling tool for the analysis of problems involving hypersonic flight through the Earth's atmosphere.

CHAPTER VI

Towards an Improved Electric Field Model

The PIC method provides a self-consistent way of computing the self-induced electric field in the shock layer, however it is too computationally expensive to use for the analysis of real atmospheric flight conditions. Thus, approximate methods of including the effects of the electric field in a DSMC simulation are needed. In this chapter, a new approximate electric field model is developed for use with the DSMC method, based on the DSMC-PIC results obtained in the previous chapter. The flow field predictions provided by the new model are shown to better approximate the self-consistent DSMC-PIC results than the baseline electric field model described in Chapter III.

6.1 Description and Implementation

This model combines some of the components of previous DSMC electric field models. The primary goal is to reproduce the increase in convective heat flux seen in the DSMC-PIC results, without significantly increasing the computational resources required for a DSMC calculation.

The model has two discrete components. In the bulk plasma region, where the DSMC-PIC results indicate that the plasma is quasi-neutral, a solution of the Boltz-

mann relation is used to obtain the plasma potential at each grid node, using the CIC procedure outlined in Section 5.4 to form a charge density at the grid nodes. The Boltzmann relation is derived from a form of the macroscopic electron momentum equation[67]:

$$m_e n_e \left[\frac{\partial \mathbf{u}_e}{\partial t} + \mathbf{u}_e \cdot \nabla \mathbf{u}_e \right] = -e n_e \mathbf{E} - \nabla p_e - m_e n_e \nu \mathbf{u}_e, \tag{6.1}$$

where ν is a collision frequency between electrons and other particles. To derive the Boltzmann relation, one makes the assumption of steady flow, negligible inertial effects, and negligible momentum transfer due to collisions with other species. These assumptions allow the first, second and fifth terms to be eliminated, and the resulting Boltzmann relation can be written as in Equation 6.2

$$n_i = n_{i,o} exp \left[\frac{e\phi(z)_{bulk}}{kT_e} \right], \tag{6.2}$$

where n_i is the ion number density and $n_{i,o}$ is a reference density. In writing the Boltzmann relation, it is further assumed that the electron pressure is given by the perfect gas equation of state $p_e = n_e k T_e$. The ion number density is used in Equation 6.2 in place of the electron number density, owing to the fact that the plasma is quasi-neutral in the bulk region. The ion number density is averaged for use in this equation using the sub-relaxation technique described in Section 3.4 with parameter $\theta = 0.0001$. The plasma potential obtained using Equation 6.2 is differentiated to obtain the electric field at the grid nodes as outlined in Section 5.4.

Work by Tomme et al.[68] showed that the potential variation in the sheath of a variety of plasmas can be predicted to very good accuracy using an expression that is quadratic in distance from the electrode. They successfully used their model to predict the charging of dust particles levitated in a plasma sheath[69]. In this work,

the Boltzmann relation is coupled to a quadratic expression for the potential drop in the plasma sheath given by Equation 6.3. In that equation, T_i is the ion translational temperature, m_e and m_i are the electron and ion masses, z_s is the sheath width given by Equation 6.4 with the Debye length λ_D also defined, and $\Delta\phi_w$ is the potential drop at the vehicle surface given by Equation 6.6. The form of Equation 6.6 implies the assumption of one-dimensional, collisionless plasma dynamics in the sheath, and zero net current to the vehicle surface.

$$\phi(z)_{sheath} = -\frac{\Delta\phi_w}{z_s^2}z^2 + \frac{2\Delta\phi_w}{z_s}z + (\phi(z_s)_{bulk} - \Delta\phi_w) \tag{6.3}$$

$$z_s = C\lambda_D \tag{6.4}$$

$$\lambda_D = \sqrt{\frac{\varepsilon_o kT_e}{n_e e^2}} \tag{6.5}$$

$$\Delta\phi_w = \frac{kT_e}{e} ln\left[\frac{T_e}{T_i}\frac{m_i}{m_e}\right] \tag{6.6}$$

During the simulation, when an ion particle moves into the sheath such that its axial coordinate z < z_s, the electric field used to accelerate the ion is computed using the plasma potential given by Equation 6.3.

Both Equations 6.2 and 6.6 require the assumption that the electrons can be described by a Maxwellian velocity distribution in the bulk plasma region[67]. Figure 6.1 shows the axial velocity distribution function of the electrons at two different locations along the axis of the shock layer in the FIRE II, 85 km case presented in Section 3.6.1. The location z = - 0.075 m is just downstream of the shock, and z = - 0.025 m is in the bulk plasma region. Also plotted on this figure are the Maxwellian velocity distribution functions, computed using the macroscopic temperature and

axial velocities in the cells at the two reference locations. Near the shock, the electron velocity distribution function is not Maxwellian, but in the bulk plasma region it has relaxed to be very close to a Maxwellian distribution. Thus, the assumption of a Maxwellian velocity distribution implicit in the form of Equations 6.2 and 6.6 is a good one.

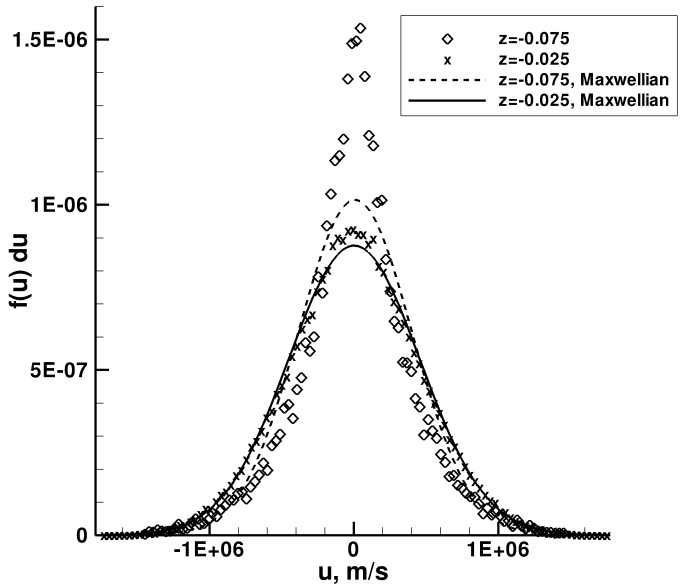

Figure 6.1: Electron velocity distribution functions along the stagnation streamline at z = -0.075m and z = -0.025m for the FIRE II, 85 km fore body DSMC simulation.

In the new electric field model, the electrons are constrained to move throughout the grid with the average ion velocity, and only the ions are accelerated by the computed electric field. The model is called the Boltzmann Quadratic Sheath (BQS) Model. The physical limitations of the model are that it cannot accurately predict i) the region of charge separation upstream of the shock layer seen in Figure 5.16, ii) the electron temperature in the sheath and free stream regions, and iii) the electron density in the sheath region. However, it contains the physics necessary to model

the important heat flux augmentation predicted by the DSMC-PIC results at the stagnation point of the flow.

The BQS model is implemented in this work by obtaining the values T_e, T_i and n_e from the DSMC-PIC flow field solutions. The value of T_e is a constant, as the electrons are approximately isothermal. The value of n_e used in Equation 6.4 is obtained from the bulk plasma region, in order to compute the Debye length in the bulk plasma region. In Equation 6.6, the value of T_i at the start of the sheath region is used. For the DSMC-PIC simulations of Case 1a and 1b presented in the previous chapter, this value is approximately equal to the value of T_e and so the condition $T_e = T_i$ is used. The average ion mass is set to the mass of atomic nitrogen ions in this work, as they are the predominant ionic species in the sheath region. In practice, the values of T_e, T_i and n_e needed to use the BQS model could either be obtained from a previous DSMC calculation utilizing the ambipolar diffusion assumption to move the electrons, or they may be computed in real-time during the DSMC-BQS calculation. There is some ambiguity in the choice of the multiplier C for the sheath width z_s, as the definition of a sheath width is fundamentally arbitrary. For the calculations presented in this work, the value of the multiplier is obtained from the location at which charge separation first occurs in the DSMC-PIC results, and the sheath width in both cases is approximately $z_s = 8\lambda_D$. In practice, this value could be varied to obtain the 'worst-case' estimate of heat flux augmentation between some suitable range of sheath width, for example $2\lambda_D \leq z_s \leq 10\lambda_D$, since the width of a plasma sheath is typically on the order of a 'few' Debye lengths[67].

While the DSMC-PIC method must be used on a grid scaled on the local Debye length of the flow, with a computational time step scaled on the electron transit time through a cell, this is not the case with the BQS model. When a standard

DSMC grid is used, in which the cell sizes are scaled on the local mean free path of the flow, the BQS model contains the physics necessary to reproduce the heat flux augmentation seen in the DSMC-PIC results. However, because the plasma sheath will be contained entirely inside one computational cell, the ion density profile in the sheath will not be resolved. The computational savings provided by the use of the BQS method are due to the ability to use grids that are scaled on the mean free path, a computational time step scaled on the mean collision or ion cell transit time, and the elimination of the need to invert a matrix to obtain the plasma potential at the grid nodes.

6.2 Comparison to PIC Results

In this section, DSMC simulations using the BQS electric field model are presented for Cases 1a and 1b described in Chapter V. The results are compared with the self-consistent DSMC-PIC results presented in that Chapter. For consistency, the length of the simulation transient period, number of sampling iterations, particle weight factor and computational grid are unchanged from those used for the one-dimensional DSMC-PIC and DSMC simulations presented in Chapter V. The simulation time step is increased to the value used in the DSMC simulations, that is, it is limited by the minimum of the local mean collision time and the ion cell transit time. The simulations of Case 1a and 1b require approximately 17 wall hours on 2 processors, which is approximately the same computational expense of the simulations computed using the baseline DSMC electric field model for these Cases.

The assumption of Boltzmann electrons is not applicable to Cases 2a and 2b since the mass of the electron particles is much larger in those simulations, making the inertial and friction terms in Equation 6.1 non-negligible. Thus, results obtained

using the BQS model for Cases 2a and 2b are not presented in this work.

6.2.1 Case 1a and Case 1b

Table 6.1 summarizes the values of flow field parameters T_e, T_i, n_e and C used in the BQS model, as well as the outputs z_s and $\Delta\phi_w$ given by the BQS model for Cases 1a and 1b. All of these parameters were obtained from the DSMC-PIC solutions for the specified Cases in the manner described in Section 6.1.

Table 6.1: Values of parameters used in BQS electric field model for Case 1a and Case 1b.

Parameter	Case 1a	Case 1b
T_e	14 000 K	16 000 K
T_i	14 000 K	16 000 K
n_e	$4.0\times10^{13}\mathrm{m}^{-3}$	$7.7\times10^{13}\mathrm{m}^{-3}$
C	8	8
z_s	0.01 m	0.008 m
$\Delta\phi_w$	5.3 V	6.1 V

Figures 6.2(a) and 6.2(b) show the ion number densities predicted using the BQS model, those given by the DSMC-PIC results, and those given by the DSMC results for both cases. The BQS model captures the trends of the ion density profiles from the DSMC-PIC results well.

Figure 6.3 shows a comparison of the electric and potential fields given by the BQS model to those predicted by the DSMC-PIC technique for both Case 1a and Case 1b. The agreement is generally quite good, although very near the wall, the quadratic form of the potential used in the BQS model does under-predict the electric field in both cases.

Figures 6.4(a) and 6.4(b) show the ion flux near the vehicle surface predicted by

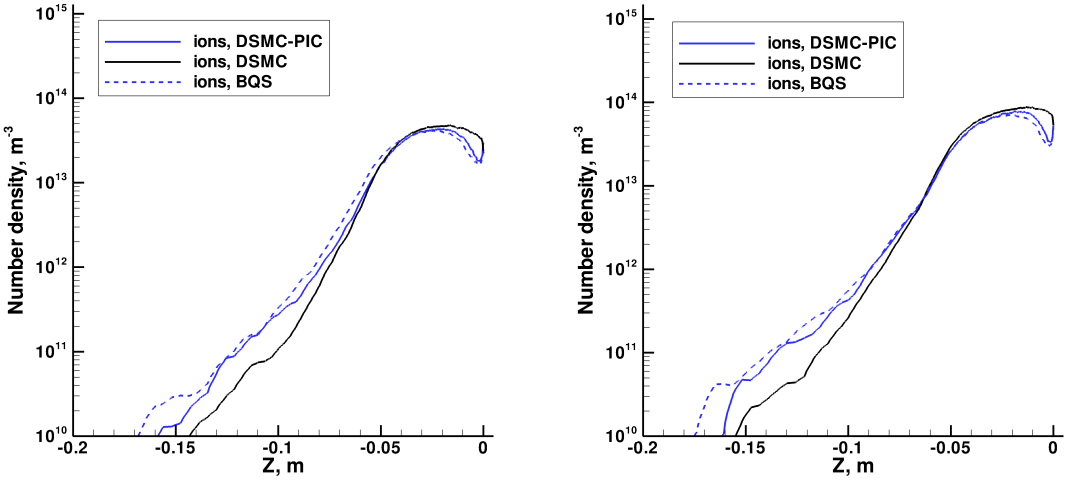

(a) 11.37 km/s case. (b) 13 km/s case.

Figure 6.2: Ion number density along the stagnation streamline predicted using the BQS model.

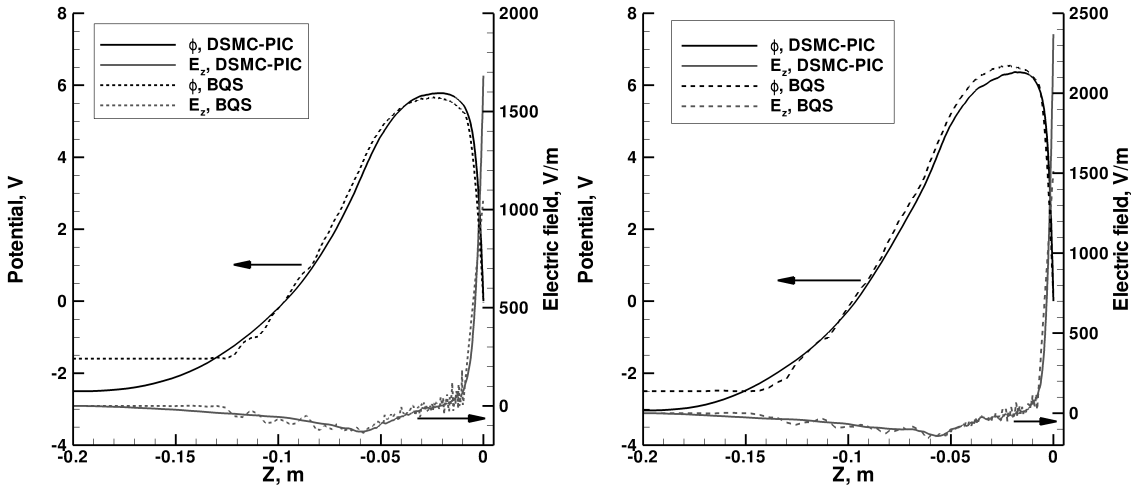

(a) Case 1a, 11.37 km/s. (b) Case 1b, 13 km/s.

Figure 6.3: Electric and potential fields predicted using the BQS model for Cases 1a and 1b.

the BQS model, and the DSMC and DSMC-PIC results for both cases. Again, the BQS model captures the character of the ion flux better than the baseline ambipolar diffusion model did, however it does under-predict the net ion flux reaching the

surface in comparison to the DSMC-PIC results. This is because the electric field is under-predicted near the vehicle surface.

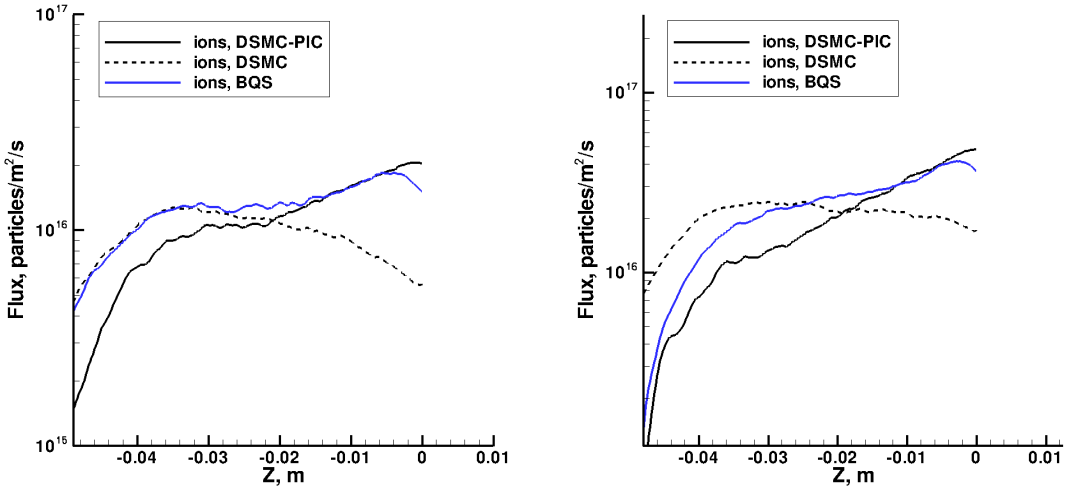

(a) 11.37 km/s case.

(b) 13 km/s case.

Figure 6.4: Ion flux along the stagnation streamline predicted using the BQS model.

Lastly, Figure 6.5 shows the heat flux prediction obtained using the BQS model, as well as the DSMC and DSMC-PIC techniques, for Case 1a and 1b. Although the BQS model does not capture all of the heat flux increase predicted by the DSMC-PIC results for Case 1a, it does predict an increase of 12% relative to the DSMC results, which for this case is within the error associated with the statistical uncertainty of the DSMC-PIC simulation. The heat flux results for the Mars return case at 13 km/s are not quite as encouraging. The BQS model in combination with the DSMC method only predicts an 8% increase in the convective heat flux for Case 1b, lower than the 13% increase predicted by the rigorous DSMC-PIC technique.

Cases 1a and 1b are also simulated using only the Boltzmann relation given by Equation 6.2 to compute the electric field, neglecting the potential variation in the sheath given by Equation 6.3. Table 6.2 provides a summary of the increase in surface

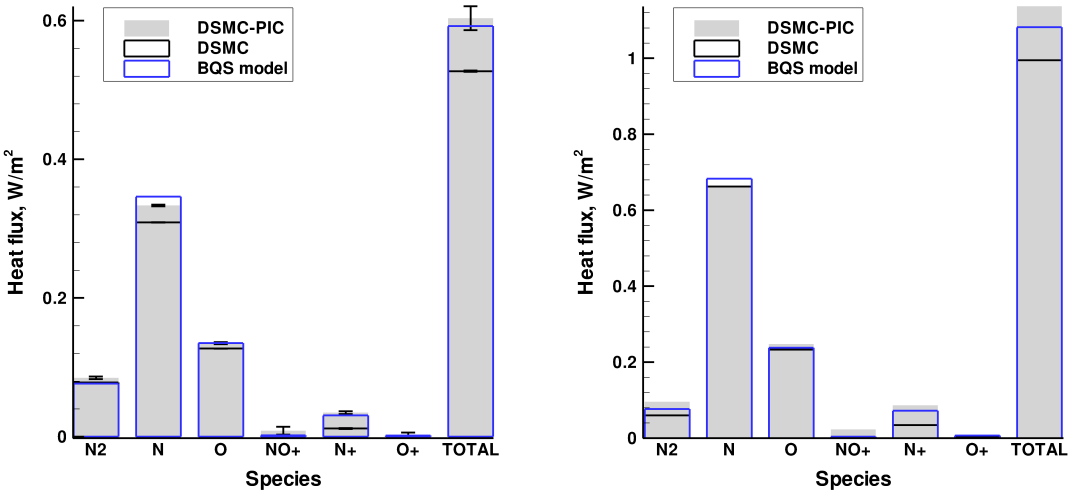

(a) Case 1a.

(b) Case 1b.

Figure 6.5: Surface heat flux results for Case 1a and 1b predicted using the BQS model.

heat flux predicted for each Case using the DSMC-PIC technique, the BQS model, and finally using only the Boltzmann relation to compute the plasma potential. The use of the quadratic sheath relation given by Equation 6.3 in addition to the Boltzmann relation results in an increase relative to the Boltzmann only results of approximately 4% in Case 1a and 7% in Case 1b. The added complication of modeling the potential variation in the sheath is warranted, as it produces improved heat flux predictions for both Cases.

Table 6.2: Summary of increase in heat flux predicted by the DSMC-PIC method and BQS model relative to the baseline DSMC results for Cases 1a and 1b.

Case	DSMC-PIC	BQS model	Boltzmann relation only
1a	14%	12%	8%
1b	14%	8%	1%

6.3 FIRE II 85 km Flight Condition

Results of a one-dimensional simulation of the stagnation streamline at the FIRE II, 85 km flight condition described in Section 3.6.1 are given in this section. The BQS model is used in lieu of the baseline electric field model to account for electrostatic effects. The computational grid is scaled on the local mean free path of the flow field, and has 230 cells. The time step used in the simulation is determined by the minimum of the mean collision time in the domain and the minimum cell crossing time of the ions in the sheath, and is 9×10^{-10} s. The simulation transient period is 500 000 time steps, and 100 000 sampling iterations are performed. There are a maximum of 5 electron particles in the cells along the stagnation streamline, a total of 55 000 particles in the simulation, and the simulation takes approximately 5.5 wall hours on 2 processors to complete. The DSMC simulation computed using the baseline electric field model requires 10 hours on 1 processor to complete, so the computational expense associated with the use of the new BQS electric field model is negligible.

Table 6.3 summarizes the values of flow field parameters T_e, T_i, n_e and C used in the BQS model, as well as the value of the parameters z_s and $\Delta\phi_w$ output from the BQS model for the simulation of the FIRE II, 85 km flight condition in one dimension. All parameters are obtained from the DSMC solution of this flight condition using the baseline electric field model, following the methodology described in Section 6.1.

Figure 6.6 shows the electric field and the potential field in the domain. The magnitude of the electric field in the sheath is truncated on this Figure, in order to show the detail in the bulk plasma region. The electric field in the sheath given by the relation in Equation 6.3 reaches a peak value of 1.2×10^{6} V/m at the vehicle

Table 6.3: Values of parameters used in BQS electric field model for the FIRE II, 85 km simulation.

Parameter	Value
T_e	13 000 K
T_i	13 000 K
n_e	$6.0\times10^{19}\mathrm{m}^{-3}$
C	8
z_s	8.1×10^{-6} m
$\Delta\phi_w$	4.9 V

surface at z = 0.0 m. The magnitude of the ambipolar field in the bulk region is approximately 150 V/m, similar to the values predicted for Case 1a and Case 1b.

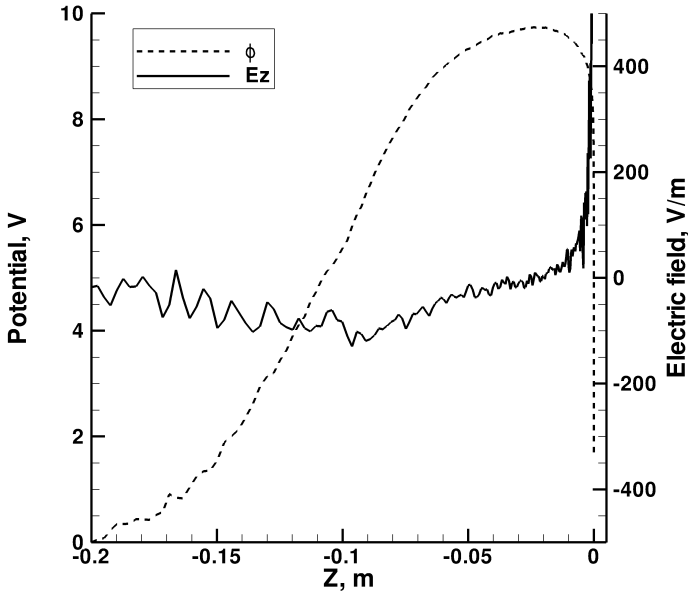

Figure 6.6: Electric and potential fields predicted using the BQS model for the FIRE II, 85 km flight condition.

Figure 6.7 shows predictions made using the baseline electric field model and the new BQS model for the ion density along the stagnation streamline, and the ion flux along the stagnation streamline. Recall that because the sheath is contained entirely

in the first computational cell next to the vehicle surface, the ion density profile in the sheath is not resolved. Thus, the decrease in ion density in the sheath predicted by the BQS model appears as a linear gradient across the first computational cell. As shown in Figure 6.7(b), the BQS model produces an ion flux profile in the bulk plasma that is similar to those produced for the simplified shock layer model of Cases 1a and 1b. In general, the net ion flux to the vehicle surface increases relative to the baseline DSMC results when the BQS model is used, and the ion density in the near wall region decreases.

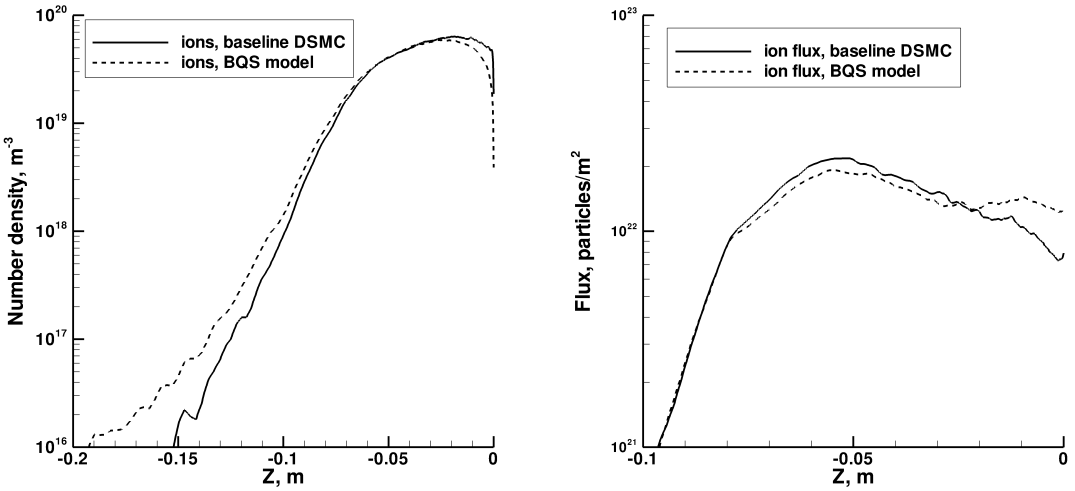

(a) Ion number density.

(b) Ion flux.

Figure 6.7: Ion quantities for the FIRE II, 85 km flight condition, predicted using the BQS model.

Table 6.4 lists the increase in surface heat flux predicted by the DSMC method when the Boltzmann relation alone is used to model the electric field effects, and when the BQS model is used. Again, the use of the BQS model results in the largest increase in predicted surface heat flux, yielding an increase in convective heat flux of 12% relative to the baseline DSMC results.

Table 6.4: Increase in heat flux predicted by the BQS model relative to the baseline DSMC results for the FIRE II, 85 km simulation.

Case	BQS model	Boltzmann relation only
FIRE II, 85 km, stagnation line	12%	6%

Note about the use of the BQS model on a DSMC grid

When the BQS electric field model is used on a DSMC grid, the sheath is contained entirely in the computational cell closest to the vehicle surface. For example, in the FIRE II simulations of Section 6.3, the sheath width is 8.1×10^{-6} m, and the width of the grid cell closest to the surface is 2×10^{-5} m. Generally, the mean collision time is the limiting time scale that determines the size of a computational time step when performing a DSMC calculation. However, if one is using the BQS model, one must ensure that the ion particles are acted on by the electric field in the sheath region at least once before they arrive at the wall. In practice, this generally means that the ion particles will be in the cell that contains the sheath for more than one time step. The accuracy of the BQS model will scale with the number of times the electric field of each ion is updated in the sheath, so that in the limit of zero computational time step, the acceleration prescribed by the potential given in Equation 6.3 will be exactly reproduced. As the size of the time step increases, the BQS model will generally under-predict the convective heat flux.

In the FIRE II simulations presented above, the minimum ion cell transit time in the sheath is estimated by dividing the cell width, 2×10^{-5} m, by the maximum mean ion velocity achieved in the sheath of near 4000 m/s. This gives a minimum ion cell crossing time of 5×10^{-9} s. The mean collision time in the sheath region is 1×10^{-8} s, and the sheath width is slightly less than one half the width of the first cell

at the wall. Thus, the simulation time step of 9×10^{-10} s is scaled so that on average, each ion spends a minimum of two iterations in the sheath region. This is viewed as a sufficient compromise between the accuracy of the BQS model and computational expense of the DSMC-BQS simulation.

6.4 Parameter Sensitivity Study

The constant parameter, C, used to set the sheath width in the BQS model is undefined when computing a flow field for which a DSMC-PIC solution is not available. Additionally, the computation of $\Delta\phi_w$ is approximate. Thus, it is useful to perform a sensitivity study using the BQS model, in which the model parameters z_s and T_e are varied and the effect on the flow field parameters is documented.

Additional DSMC simulations of Case 1b using the BQS model are run, in which the parameters are varied such that 15 000 $K \leq T_e \leq$ 16 000 K and 0.006 $m \leq z_s \leq 0.01$ m, corresponding to values of 5.7 $V \leq \Delta\phi_w \leq 6.1$ V and $6 \leq C \leq 10$ respectively. The electron temperature is varied over a smaller range than the sheath width because in practice, this parameter can be much more accurately estimated from the peak in the electron temperature predicted by the baseline DSMC simulation than the sheath width can. Thus, one expects a larger variation in the sheath width values obtained from the baseline solution for input to the BQS model. As in the previous cases, the assumption that $T_e = T_i$ at the start of the sheath is made, and the ion mass in Equation 6.6 is set equal to the mass of the nitrogen atomic ion. The selection of ion temperature and average ion mass does not have a significant effect on the value of $\Delta\phi_w$, because these parameters appear in the logarithm of Equation 6.6 only.

Figures 6.8(a) and 6.8(b) show the sensitivity of the flow field solution for the

ion flux to the electron temperature and sheath width used in the BQS model. On these figures, the results of the baseline DSMC and DSMC-PIC simulations are labeled, and not included in the legend for clarity. While the results appear to be relatively insensitive to electron temperature, it is clear that the ion flux is much more sensitive to the specified sheath width. For this Case, the simulation that utilizes $T_e = 15\,500\ K$ and $z_s = 0.01\ m$ gives the best agreement with the DSMC-PIC results for the ion flux.

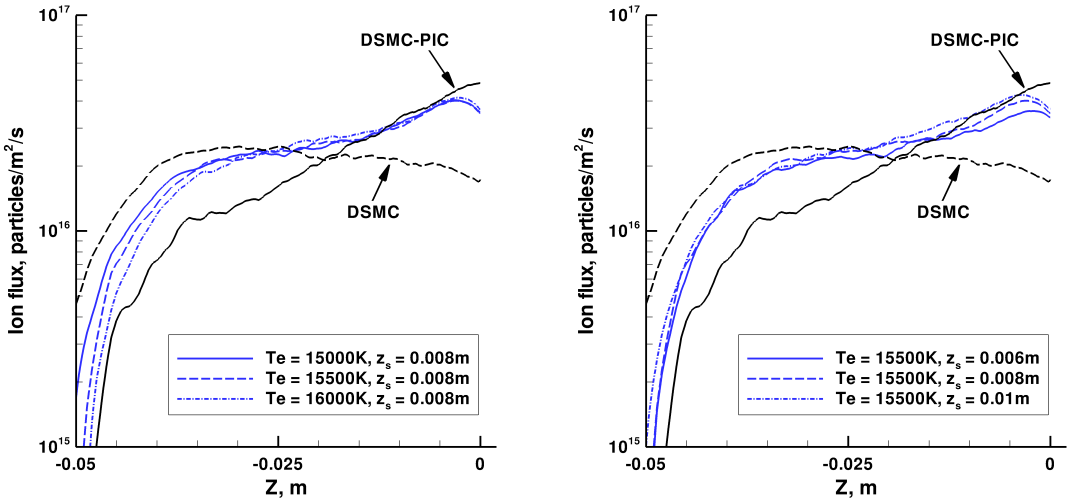

(a) Sensitivity to T_e.

(b) Sensitivity to z_s.

Figure 6.8: Sensitivity of the prediction of ion flux to the BQS model parameters T_e and z_s.

Figures 6.9(a) and 6.9(b) show the sensitivity of the ion number density result to changes in electron temperature and sheath width used in the BQS model. Again, varying the sheath width has a larger effect on the ion number density profiles than does varying the electron temperature.

Table 6.5 summarizes the convective heat flux predicted using the BQS model with each set of model parameters. Based on the number of heat flux samples collected during these computations, the statistical error on the results in Table 6.5

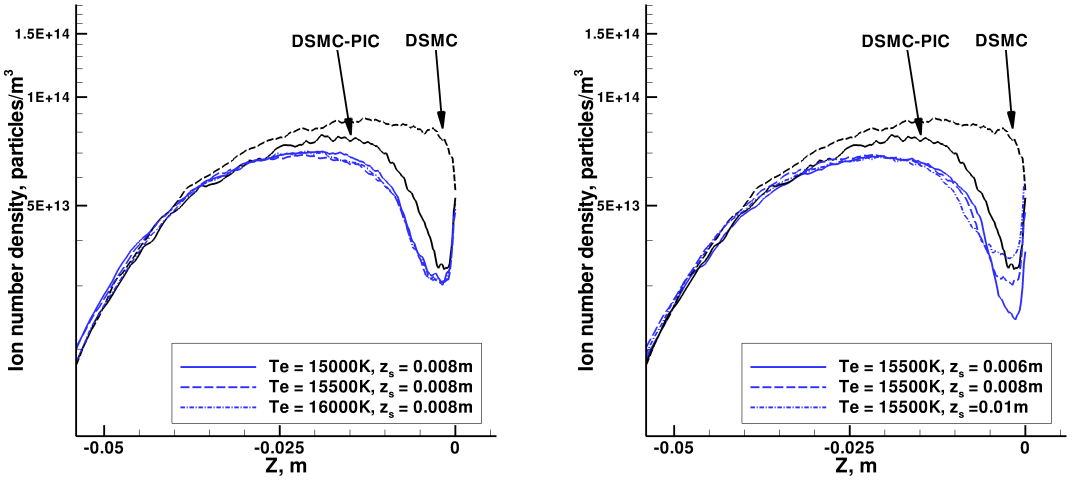

(a) Sensitivity to T_e.

(b) Sensitivity to z_s.

Figure 6.9: Sensitivity of the prediction of ion number density to the BQS model parameters T_e and z_s.

is expected to be approximately equal to the error on the DSMC calculations of Case 1a presented in Chapter V, which was $\pm 0.4\%$. The heat flux results are more sensitive to electron temperature. This is probably because heat flux due to neutral particle impact comprises the majority of the total surface heat flux. Varying the electron temperature directly affects the electric field that is applied in the bulk plasma, through the Boltzmann relation given in Equation 6.2, and that field operates on a much larger region of plasma than the sheath. Ions that are accelerated by that field are able to transfer that energy to neutrals through collisions.

Table 6.5: Sensitivity of the increase in convective heat flux predicted by the BQS model relative to the baseline DSMC results for various values of T_e and z_s.

T_e	z_s	% increase relative to DSMC result
15 000 K	0.008 m	4.5%
15 500 K	0.008 m	4.4%
16 000 K	0.008 m	7.7%
15 500 K	0.006 m	4.5%
15 500 K	0.008 m	4.4%
15 500 K	0.01 m	4.0%

CHAPTER VII

Conclusions

This chapter contains a summary of the results of this thesis and the original contributions made to the field, and identifies future research directions.

7.1 Summary of Results

Chapter I discussed the structure of the plasma formed behind a strong bow shock during the reentry of a vehicle into the Earth's atmosphere. The behavior of this plasma is coupled to the behavior of the neutral portion of the flow field, and its presence interferes with the transmission of radio waves to the vehicle. Additionally, the presence of the plasma modifies the structure of the neutral portion of the flow field through this coupling, and affects the rate of heat transfer to the surface of the vehicle. These latter effects can be important for the design of the vehicle TPS. The unique physical phenomena that occur in the plasma are discussed: collisions involving charged particles, efficient vibrational and electronic mode excitation, ionization and charge exchange reactions, charging of vehicle surfaces and the self-induced electric field. At the end of this chapter, the RAM-C, FIRE and Stardust flight experiments are discussed, illustrating the sparsity of measured data for reentry plasma parameters and the need for a DSMC modeling capability for

weakly ionized reentry flow fields.

In Chapter II, the Boltzmann equation for an ionized gas is derived from the canonical Liouville equation using the assumption of molecular chaos and short collision times. The form of the electrostatic body force used in the Boltzmann equation is given, using the assumptions of an unmagnetized plasma and a large number of plasma particles in a Debye sphere. The difficulty of solving this equation due to its high dimensionality is discussed, and the concepts of Debye length and Knudsen number are introduced. The regime of applicability of the macroscopic Navier-Stokes equations is quantified using both the global Knudsen number and the local gradient length Knudsen number. An outline of the DSMC algorithm is given, including the basic physical models for particle collisions, internal energy exchange and chemical reactions used within the algorithm. Lastly, an overview of related work involving DSMC calculations of weakly ionized, hypersonic flow fields is given. The lack of a systematic assessment in the literature of the physical models used to predict the plasma behavior is highlighted.

In Chapter III, baseline models for collisions and reactions between charged particles and the self-induced electric field are introduced, and the implementation of these models in the MONACO code is described. Next, axisymmetric DSMC flow field calculations for both the 85 km and 76 km flight conditions of the FIRE II vehicle are presented, in which only the fore body of the flow is modeled. These calculations are carried out using a neutral species air model, as well as an air model that includes charged species. The inclusion of charged species in the DSMC calculation results in a reduction in shock stand-off distance, a reduction in rotational and vibrational temperatures, and a slight decrease in the predicted convective heat flux to the vehicle surface at both flight conditions. The effects are more pronounced at

the 76 km flight condition. An axisymmetric calculation of the flow field around the entire FIRE II vehicle at the 85 km flight condition is presented next. The results of this calculation show that the baseline ambipolar diffusion model for the electric field does not perform as well in the wake region as it does in the fore body region of the flow field. Lastly, a three dimensional calculation of the fore body for the FIRE II, 85 km flight condition is completed. The results of the calculation show that the baseline ambipolar diffusion model for the electric field performs well in three dimensions.

In Chapter IV, the predictions of the baseline collision and chemistry models for the interaction of charged particles are compared to those obtained using specific cross section data. Using the FIRE II, 85 km flight condition as a test case, it is shown that the use of more accurate cross section data for elastic collisions between electrons and neutral particles has no appreciable effect on the flow field parameters. The use of experimentally determined cross section data for electron impact dissociation of molecular nitrogen results in a decrease in the level of nitrogen dissociation in the flow field. This is turn increases the amount of atomic nitrogen and oxygen ionized by electron impact, due to the increase in the number of energetic electrons in the flow. However, when cross section data is also used to model the electron impact ionization of these species from their ground electronic states, their concentrations return to the values predicted using the baseline chemistry model. The use of both theoretically and experimentally determined reaction cross section data for the associative ionization of atomic nitrogen and oxygen results in very little change in the flow field parameters, although this result is limited to the case where the electronic modes of the colliding atoms are in equilibrium at the electron translational temperature. Based on the results presented in this chapter, it is recommended that

future modeling efforts use the reaction cross section data of Cosby with the total cross section data of Itikawa to model electron impact dissociation of nitrogen. If the electronic excitation of atomic species is not included in the flow field calculation, then the cross section data of Bell et al. should be used to model electron impact ionization of nitrogen and oxygen, unless a reaction rate coefficient that includes the ground electronic state and is mathematically compatible with the TCE model becomes available. If reaction rates for the ionization of atoms solely from the excited electronic levels are used with the TCE model, the reduction in flow field energy caused by these events is under-predicted. This may result in an over-prediction of the degree of ionization in the flow field.

In Chapter V, the difficulties associated with the use of the PIC method to compute shock layer plasmas are identified. The computational grid must be scaled on the local Debye length of the flow, and the time step scaled on the electron transit time, in order to obtain a stable solution. Additionally, a reduction in the particle weight factor relative to the value used for a neutral flow field simulation is required to ensure that a sufficient number of ion and electron simulator particles are present in each cell. A one-dimensional, reduced order shock layer model is developed to simulate the structure of the shock layer formed in front of the FIRE II vehicle at the 85 km trajectory point at reasonable computational expense. The self-consistent DSMC-PIC method is used to produce flow field solutions for the shock layer model, and those are compared to baseline DSMC solutions. Compared to the baseline flow field predictions, the DSMC-PIC method yields an increase in both the electron and ion number densities in the flow upstream of the shock layer, and a decrease in those densities in the sheath region. The predicted electron translational temperature is larger in both the upstream and sheath regions with the use of the DSMC-PIC

method, and approximately isothermal. Lastly, the DSMC-PIC method predicts a significant increase in convective heat flux to the vehicle surface relative to the base line DSMC results. The computational resources required for a one-dimensional DSMC-PIC calculation of the stagnation streamline of the FIRE II, 85 km flight condition are estimated to be too great for the DSMC-PIC method to be used to provide flow field solutions for reentry vehicle design and mission analysis.

Chapter VI presents an approximate electric field model for use in rarefied reentry flow field calculations. The model incorporates portions of previously proposed electric field models, namely the technique used to move the electron particles, and the use of the Boltzmann relation in the bulk plasma to obtain the plasma potential. An expression for the quadratic variation of the plasma potential in the sheath is formulated using bulk plasma parameters, and this is patched to the Boltzmann solution in the bulk region. The new model is used to simulate the flow fields from the reduced order shock layer model presented in Chapter V, and the results are compared to the DSMC-PIC results of that chapter. The profile of ion number density and the increase in convective heat flux relative to the baseline DSMC results are successfully predicted by the new electric field model. The new model is used to simulate the flow along the stagnation streamline at the FIRE II, 85 km flight condition, and predicts an increase in the stagnation point convective heat transfer of 12% relative to the baseline DSMC prediction.

7.2 Contributions

A list of the original contributions of this thesis to the state of the art in computational hypersonic, rarefied flow field prediction is given here. These contributions are contained in Refs. [70, 71, 72, 73, 74].

1. Surface heat flux predictions for both the FIRE II 85 km and 76 km flight conditions, including ionization phenomena, are produced that are in better overall agreement with measured flight data than previous computations by other researchers.

2. For the first time in the literature, the baseline VHS particle interaction model is shown to be adequate for the treatment of collisions between neutral particles and electrons in rarefied hypersonic flow fields.

3. The predictions of the baseline chemistry model for reactions involving charged particles in air are compared to experimentally and theoretically obtained cross section data for the first time in the literature. Although the use of cross section data in a complicated DSMC calculation proves challenging, it is shown that the use of experimental cross section data for modeling the electron impact dissociation of N_2 produces a large increase in the degree of ionization, and in the temperatures of the internal modes of the flow field, at the FIRE II 85 km flight condition. It is also shown that it is important to adequately treat the electronic mode of the N and O atoms, that is, to use reaction cross section or rate data for electron impact ionization from the ground electronic state if electronic excitation is not explicitly modeled in the simulation. Failure to do so results in the over-prediction of the degree of ionization in the shock layer.

4. Self-consistent DSMC-PIC simulations of the flow field and the electric field generated in a rarefied hypersonic shock layer are presented for the first time in the literature. The inclusion of the electric field in the simulation in a self-consistent manner results in an increase in the electron temperature in the sheath and free diffusion regions, a decrease in the plasma density in the

sheath, an increase in the plasma density in the free diffusion region, and a significant increase in the convective heat flux to the vehicle surface. In the bulk plasma region, the flow field results from the DSMC-PIC simulations agree well with those obtained using the baseline electric field model. Additionally, the plasma potential obtained from the DSMC-PIC simulations agrees well with that computed using the simple Boltzmann relation for the electrons in the bulk plasma region. These results represent the first ever evaluation of the limitations of the baseline electric field model derived from the ambipolar diffusion assumption.

5. A new approximate electric field model is proposed that employs the Boltzmann relation to calculate the plasma potential in the bulk plasma region, and a relation describing a quadratic variation of the plasma potential in the sheath region. The model is able to reproduce the decrease in ion density in the sheath region and the increase in the free diffusion region. It is also able to partially reproduce the increase in convective heat flux seen in the DSMC-PIC results for both an Earth and a Mars-return reentry case. The new model does not require significantly more computational resources than a baseline DSMC calculation, and therefore can be used to provide predictions of the flow field and plasma potential at realistic flight conditions.

In summary, physical models for the treatment of charged particles using the DSMC method have been implemented into the MONACO solver. The use of the Variable Hard Sphere model is shown to be sufficient for modeling weakly ionized, reentry flow fields. The use of reaction cross section data is recommended for modeling the dissociation of nitrogen due to collisions with electrons, and for modeling

the electron impact ionization of nitrogen and oxygen from the ground electronic state. Modeling the self-induced electric field in the shock layer is shown to produce a non-negligible increase in the predicted convective heat flux at the vehicle stagnation point relative to calculations that do not model this field. An improved electric field model for use in DSMC calculations is suggested that reproduces the increase in stagnation point heat flux in rarefied, hypersonic shock layers.

As a direct result of this thesis, a computational tool now exists at the University of Michigan to predict the properties of the weakly ionized plasma formed during hypersonic flight of a vehicle through the rarefied portion of the Earth's atmosphere. This is significant since knowledge of the plasma properties is necessary to accurately predict radio signal attenuation and black out for a given mission, and to design mitigation schemes to prevent the loss of radio communication with the vehicle. Additionally, this thesis shows that the self-induced electric field generated by this plasma can have a significant effect on the level of convective heating experienced by a hypersonic vehicle traveling in the Earth's atmosphere. The heat flux results and the improved electric field model presented in this thesis can be used to better quantify the error associated with computational heat flux predictions used to design thermal protection systems for hypersonic vehicles. Lastly, the results of this thesis indicate a need to investigate the effect of the self-induced electric field on the heating rate experienced by a vehicle during flight through the continuum portion of the Earth's atmosphere, as the peak heating rate and the majority of the heat load is typically experienced in this flight regime.

7.3 Future Directions

The ionization models included in MONACO as a result of this thesis provide a solid foundation on which to further investigate the physics of nonequilibrium reentry flow fields. For the calculation of flow fields that are not one-dimensional, the BQS electric field model will need to be extended. It is clear that the treatment of chemical reactions taking place in the shock layer, and the interaction of the flow with the surface of the vehicle, are of fundamental importance to obtaining high quality flow field results.

Automation of the electric field calculation and extension to 2D/3D

The new BQS electric field model requires macroscopic flow field parameters to be generated as model inputs. This requires the user to first complete a DSMC calculation of a given flow field without the electric field, before computing the solution using the BQS model. It may be possible to compute the temperatures and electron number density that are needed for the BQS model in real time during the DSMC calculation. Because the trace ionized species are needed for the calculation, some type of averaging technique will need to be applied in order to reduce the level of statistical scatter in the quantities before using them in the calculation of the plasma potential. For the simulation of full vehicle geometries, and vehicles at an angle of attack, the dimensionality of the BQS model would need to be increased. This task should be relatively straightforward for the solution of the Boltzmann relation, as it is computed using the existing DSMC grid structure. In fact, the existing hybrid MONACO-PIC solver that treats the electrons as a fluid already contains this functionality.

The implementation of the quadratic relation for the variation of plasma potential

in the sheath will require careful thought. In the current form, this relation is valid only as long as one-dimensional flow in the sheath can be assumed. This is a good approximation along the stagnation streamline, but will break down in the rest of the flow field. In the mean time, the Boltzmann relation alone can be used to provide an estimate of the electric field everywhere in the flow, as it partially reproduces the augmentation of convective heat flux caused by the acceleration of ions in the electric field.

Individual species weighting

The computational burden of including ionization in the DSMC calculation could be reduced by using individual weights for the ion and electron species since they are present in small quantities in the flow field. In the FIRE II, 85 km simulation that had a degree of ionization of 2%, a total of 500 particles were simulated in each cell in order to have 10 electron particles in the cell. Since the recommended minimum number of particles per cell in a DSMC calculation of this nature is 20, significant computational savings could be realized if the electrons and ions were assigned a smaller weight factor than the neutral particles. Currently, the MONACO solver has an individual species weighting capability for simulating elastic collisions, and inelastic collisions involving only internal energy exchange. Individual species weighting is not implemented for modeling chemical reactions, and methods of doing this effectively are the subject of research in the DSMC community. Additionally, the implementation of individual species weighting in the chemistry routines would allow higher free stream densities to be reached in the DSMC-PIC calculations, as well as enable more efficient simulation of other types of rarefied flows that involve reacting trace species. Examples of such rarefied flows include plasma processing

type problems[75] and the modeling of the radiative glow of orbiting spacecraft[76].

Electronic excitation

Accurate cross section data for the reaction of particles in a given translation and ro-vibrational state is most often determined either through crossed beam type experiments or theoretical methods. For cross sections involving electron impact, swarm type experiments can also be used. As more of this data becomes available, either via experiments or theoretical techniques such as Quasi-Classical Trajectory (QCT) calculations (see Ref. [77] for example), a method of utilizing it effectively in a DSMC solver will become more desirable. The results presented in this thesis point to the need for a consistent electronic excitation model in order to implement some of this state-to-state cross section data for chemical reactions. In addition, modeling the excitation of the electronic mode is a necessary step before radiative heat transfer can be included in a fully self-consistent manner in the DSMC solver.

Treatment of the vehicle surface

During the computation of all of the flow fields presented in this thesis, the surface of the vehicle is assumed to be fully catalytic to ions and electrons and not catalytic to the recombination of atoms. Additionally, the emission of secondary electrons from the vehicle surface, as well as surface charging effects, are neglected. The treatment of the interaction of flow with the vehicle surface can play a large role in the prediction of the convective heating rate. This is illustrated by the difference between the heat transfer predictions presented in this thesis and those presented by previous researchers for the FIRE II 85 km flight condition. Theoretical techniques like Molecular Dynamics (MD) simulation are showing promise for providing information that can be used in flow field solvers to accurately predict the surface

behaviour of typical Thermal Protection System (TPS) materials during reentry (see Ref. [78] for example). In order to use this data in a DSMC simulation, the treatment of particles that reach wall boundaries needs to be modified to allow for finite rate atom recombination, or even chemical reactions, to occur at the surface.

Regarding secondary electron emission, although the emission coefficient for typical TPS materials is not well understood, representative values can be used to deduce the impact of including secondary emission on the DSMC-PIC flow field predictions. Additionally, rather than letting a current flow to the surface, the vehicle could be modeled as a dielectric. To do so, the computational grid would be extended past the surface, charge would be collected at the surface grid node, and a zero electric field boundary condition would be applied inside the vehicle. In this way, an estimate of the expected level of surface charging at steady state could be obtained at the stagnation point.

APPENDICES

APPENDIX A

Species and Chemistry Data

The following tables provide the values for the collision, rotational and vibrational relaxation, and chemistry models used in the MONACO solver during the course of this thesis. Additional details about these parameters and the structure of the input files are found in the MONACO user manual that is distributed with the code.

Table A.1: Baseline parameters used in the VHS molecular model.

Parameter	Baseline value
ω	0.20
T_{ref}	288 K
d_{N_2}	4.07×10^{-10} m
d_{O_2}	3.96×10^{-10} m
d_{NO}	4.00×10^{-10} m
d_N	3.00×10^{-10} m
d_O	3.00×10^{-10} m
$d_{N_2^+}$	4.07×10^{-10} m
$d_{O_2^+}$	3.96×10^{-10} m
d_{NO^+}	4.00×10^{-10} m
d_{N^+}	3.00×10^{-10} m
d_{O^+}	3.00×10^{-10} m
d_e	1.00×10^{-10} m

Table A.2: Baseline reaction rate coefficients (m^3/molecule/s) used in the TCE chemistry model for reactions involving neutral species.

Number	Reaction	Rate Coefficient
1Mf[a]	N_2+M→N+N+M	$1.162\times10^{-8}T^{-1.6}\exp(-113\ 200/T)$
1Mb	N + N + M → N_2 + M	$1.072\times10^{-39}T^{-1.6}$
1Af[b]	N_2+A→N+N+A	$4.980\times10^{-8}T^{-1.6}\exp(-113\ 200/T)$
1Ab	N + N + A → N_2 + A	$4.597\times10^{-39}T^{-1.6}$
1E[c]	N_2+e^-→N+N+e^-	$4.980\times10^{-6}T^{-1.6}\exp(-113\ 200/T)$
2Mf	O_2+M→O+O+M	$3.321\times10^{-9}T^{-1.5}\exp(-59\ 400/T)$
2Mb	O + O + M → O_2 + M	$4.597\times10^{-42}T^{-1.0}$
2Af	O_2+A →O+O+A	$1.660\times10^{-8}T^{-1.5}\exp(-59\ 400/T)$
2Ab	O + O + A → O_2 + A	$2.298\times10^{-41}T^{-1.0}$
3Mf	NO+M→N+O+M	$8.302\times10^{-15}\exp(-75\ 500/T)$
3Mb	N + O + M → NO + M	3.447×10^{-45}
3Af	NO+A→N+O+A	$1.826\times10^{-13}\exp(-75\ 500/T)$
3Ab	N + O + A → NO + A	7.583×10^{-44}
4f[d]	O+NO→N+O_2	$1.389\times10^{-17}\exp(-19\ 700/T)$
4b[e]	N+O_2 →O+NO	$4.601\times10^{-15}T^{-0.546}$
5f	O+N_2 →N+NO	$1.069\times10^{-12}T^{-1.000}\exp(-37\ 500/T)$
5b	N+NO→O+N_2	$4.059\times10^{-12}T^{-1.359}$

[a]Reaction involving a molecular collision partner.
[b]Reaction involving an atomic collision partner.
[c]Reaction involving an electron as the collision partner.
[d]Forward rate for reaction mechanism.
[e]Reverse rate for reaction mechanism.

Table A.3: Baseline reaction rate coefficients (m^3/molecule/s) used in the TCE chemistry model for reactions involving charged species.

Number	Reaction	Rate Coefficient
6f	$N+N \rightarrow N_2^+ + E^-$	$3.387\times10^{-17}\exp(-67\ 700/T)$
6b	$N_2^+ + E^- \rightarrow N+N$	$7.274\times10^{-12}T^{-0.650}$
7f	$O+O \rightarrow O_2^+ + E^-$	$1.859\times10^{-17}\exp(-81\ 200/T)$
7b	$O_2^+ + E^- \rightarrow O+O$	$1.453\times10^{-4}T^{-2.412}$
8f	$N+O \rightarrow NO^+ + E^-$	$8.766\times10^{-18}\exp(-32\ 000/T)$
8b	$NO^+ + E^- \rightarrow N+O$	$1.321\times10^{-9}T^{-1.187}$
9f	$N_2+O^+ \rightarrow O+N_2^+$	$1.511\times10^{-18}T^{0.360}\exp(-22\ 800/T)$
9b	$O+N_2^+ \rightarrow N_2+O^+$	$1.978\times10^{-18}T^{0.109}$
10f	$NO+O^+ \rightarrow O_2+N^+$	$2.324\times10^{-25}T^{1.900}\exp(-15\ 300/T)$
10b	$O_2+N^+ \rightarrow NO+O^+$	$2.443\times10^{-26}T^{2.102}$
11f	$O_2+NO^+ \rightarrow NO+O_2^+$	$3.985\times10^{-17}T^{0.410}\exp(-32\ 600/T)$
11b	$NO+O_2^+ \rightarrow O_2+NO^+$	$6.195\times10^{-16}T^{-0.050}$
12f	$N+NO^+ \rightarrow O+N_2^+$	$1.195\times10^{-16}\exp(-35\ 500/T)$
12b	$O+N_2^+ \rightarrow N+NO^+$	$1.744\times10^{-18}T^{0.302}$
13f	$O+NO^+ \rightarrow O_2+N^+$	$1.660\times10^{-18}T^{0.500}\exp(-77\ 2000/T)$
13b	$O_2+N^+ \rightarrow O+NO^+$	$2.192\times10^{-17}T^{0.114}$
14f	$N+O_2^+ \rightarrow O_2+N^+$	$1.444\times10^{-16}T^{0.140}\exp(-28\ 600/T)$
14b	$O_2+N^+ \rightarrow N+O_2^+$	$4.993\times10^{-18}T^{-0.004}$
15f	$N_2+O_2^+ \rightarrow O_2+N_2^+$	$1.644\times10^{-17}\exp(-40\ 700/T)$
15b	$O_2+N_2^+ \rightarrow N_2+O_2^+$	$4.589\times10^{-18}T^{-0.037}$
16f	$N+NO^+ \rightarrow N_2+O^+$	$5.645\times10^{-17}T^{-1.080}\exp(-12\ 800/T)$
16b	$N_2+O^+ \rightarrow N+NO^+$	$3.970\times10^{-18}T^{-0.710}$
17f	$O+NO^+ \rightarrow N+O_2^+$	$1.195\times10^{-17}T^{0.290}\exp(-48\ 600/T)$
17b	$N+O_2^+ \rightarrow O+NO^+$	$8.918\times10^{-13}T^{-0.969}$
18f	$O+O_2^+ \rightarrow O_2+O^+$	$6.641\times10^{-18}T^{-0.09}\exp(-18\ 600/T)$
18b	$O_2+O^+ \rightarrow O+O_2^+$	$4.993\times10^{-18}T^{-0.004}$
19f	$N_2+N^+ \rightarrow N+N_2^+$	$1.660\times10^{-18}T^{0.500}\exp(-12\ 100/T)$
19b	$N+N_2^+ \rightarrow N_2+N^+$	$2.343\times10^{-14}T^{-0.610}$
20	$N+E^- \rightarrow N^+ + 2E^-$	$8.434\times10^{-14}\exp(-121\ 000/T)$
21	$O+E^- \rightarrow O^+ + 2E^-$	$1.054\times10^{-14}\exp(-106\ 200/T)$

Table A.4: Species data contained in the spec.dat input file.

Species	Mass, kg/kmol	ζ_{rot} [a]	ζ_{vib} [b]	θ_{vib} [c], K	$T_{ref,rot}$ [d], K	$Z_{max,rot}$ [e]	P_{vib} [f]
N_2	28.0	2.0	1.8	3390	91.5	18.1	0.01
O_2	32.0	2.0	1.8	2270	113.5	16.5	0.05
NO	30.0	2.0	1.8	2740	119.0	7.5	0.05
N	14.0	0.0	0.0	1.0	1.0	1.0	0.0
O	16.0	0.0	0.0	1.0	1.0	1.0	0.0
N_2^+	28.0	2.0	1.8	3390	91.5	18.1	0.01
O_2^+	32.0	2.0	1.8	2270	113.5	16.5	0.05
NO^+	30.0	2.0	1.8	2740	119.0	7.5	0.05
N^+	14.0	0.0	0.0	1.0	1.0	1.0	0.0
O^+	16.0	0.0	0.0	1.0	1.0	1.0	0.0
e	5.5×10^{-4}	0.0	0.0	1.0	1.0	1.0	0.0

[a] Number of rotational degrees of freedom.
[b] Number of vibrational degrees of freedom.
[c] Characteristic temperature for vibration.
[d] Reference temperature for rotational energy exchange model.
[e] Maximum rotational collision number.
[f] Constant probability of vibrational energy exchange. Not used if vib.dat is present.

Table A.5: Parameters used for modeling vibrational relaxation contained in the vib.dat input file.

Reference temperature											10 000 K
Reference cross section											5.81×10^{-21} m^2
Species	N_2	O_2	NO	O	N	N_2^+	O_2^+	NO^+	N^+	O^+	e
Coefficient A											
N_2	220.00	115.10	101.20	180.47	31.06	220.00	115.10	101.20	180.47	31.06	1.39
O_2	115.10	129.00	136.16	108.00	43.56	115.10	129.00	136.16	108.00	43.56	0.81
NO	101.20	174.99	63.28	137.41	43.56	101.20	174.99	63.28	137.41	43.56	1.04
N	180.47	108.00	137.41	0.00	0.00	180.47	108.00	137.41	0.00	0.00	0.00
O	31.06	43.56	43.56	0.00	0.00	31.06	43.56	43.56	0.00	0.00	0.00
N_2^+	220.00	115.10	101.20	180.47	31.06	220.00	115.10	101.20	180.47	31.06	1.39
O_2^+	115.10	129.00	136.16	108.00	43.56	115.10	129.00	136.16	108.00	43.56	0.81
NO^+	101.20	174.99	63.28	137.41	43.56	101.20	174.99	63.28	137.41	43.56	1.04
N^+	180.47	108.00	137.41	0.00	0.00	180.47	108.00	137.41	0.00	0.00	0.00
O^+	31.06	43.56	43.56	0.00	0.00	31.06	43.56	43.56	0.00	0.00	0.00
e	1.39	0.81	1.04	0.00	0.00	1.39	0.81	1.04	0.00	0.00	0.00
Coefficient B											
N_2	-12.27	-6.92	-5.26	-10.62	-3.51	-12.27	-6.92	-5.26	-10.62	-3.51	-6.90
O_2	-6.92	-9.76	-9.93	-8.75	-8.50	-6.92	-9.76	-9.93	-8.75	-8.50	-6.90
NO	-5.26	-11.10	-9.50	-9.51	-8.50	-5.26	-11.10	-9.50	-9.51	-8.50	-6.90
N	-10.62	-8.75	-9.51	0.00	0.00	-10.62	-8.75	-9.51	0.00	0.00	0.00
O	-3.51	-8.50	-8.50	0.00	0.00	-3.51	-8.50	-8.50	0.00	0.00	0.00
N_2^+	-12.27	-6.92	-5.26	-10.62	-3.51	-12.27	-6.92	-5.26	-10.62	-3.51	-6.90
O_2^+	-6.92	-9.76	-9.93	-8.75	-8.50	-6.92	-9.76	-9.93	-8.75	-8.50	-6.90
NO^+	-5.26	-11.10	-9.50	-9.51	-8.50	-5.26	-11.10	-9.50	-9.51	-8.50	-6.90
N^+	-10.62	-8.75	-9.51	0.00	0.00	-10.62	-8.75	-9.51	0.00	0.00	0.00
O^+	-3.51	-8.50	-8.50	0.00	0.00	-3.51	-8.50	-8.50	0.00	0.00	0.00
e	-6.90	-6.90	-6.90	0.00	0.00	-6.90	-6.90	-6.90	0.00	0.00	0.00

APPENDIX B

Mathematical Basis for 1D DSMC Algorithm

The procedure for simulating the stagnation streamline of the flow field about a hypersonic vehicle using the DSMC technique in one dimension is introduced in Chapter V. A summary of the derivation of the criteria for particle removal presented in Refs. [7] and [33] is given here.

Since the gas composition changes across the shock, mass conservation is enforced on a per atom basis in the 1D DSMC implementation. The equation describing the conservation of mass along the stagnation streamline is written as

$$d\left(\rho u\right) = -\dot{m}dz, \tag{B.1}$$

where $\dot{m}$ is the rate of removal of molecular mass per unit volume. Defining $\overline{u}$ as the mean streamwise velocity of the removed particles, the equation of conservation of momentum is

$$dp = -d\left(\rho u^2\right) - \overline{u}\dot{m}dz. \tag{B.2}$$

and can also be written as

$$dp = -\rho u du - ud(\rho u) - \overline{u}\dot{m}dz. \tag{B.3}$$

Comparison of the last two terms in Equation B.3 with Equation B.1 shows that these final two terms cancel as long as $\overline{u} = u$. This means that the continuum momentum equation is satisfied as long as particles are removed with a probability independent of their streamwise velocity.

The energy conservation equation can be written as

$$d\left(\rho u h_o\right) = -\dot{m}\overline{e_o}dz, \tag{B.4}$$

where h_o is the stagnation enthalpy, and $\overline{e_o}$ is the mean stagnation energy of the removed particles. This equation can be rewritten as

$$\rho u dh_o + h_o d\left(\rho u\right) = -\dot{m}\overline{e_o}dz. \tag{B.5}$$

Equation B.1 can be used to reduce Equation B.5 to the continuum energy equation

$$dh_o = 0, \tag{B.6}$$

if particles are chosen for removal such that the selection criteria

$$\overline{e_o} = h_o \tag{B.7}$$

is statisfied.

Equation B.7 is satisfied when the average specific energy of the removed particles exceeds that averaged over all particles in the flow by the quantity RT. This is accomplished by removing particles with a probability proportional to a power, j, of their velocity component normal to the freestream. In this case, the mean translational energy of the removed molecules is

$$\overline{e_t} = (3 + j)\,\frac{RT}{2}, \tag{B.8}$$

and the required value is $j = 2$. Thus, particles are removed with a probability proportional to the square of their velocity components normal to the symmetry axis.

The derivation presented above is strictly valid only for the removal of particles at locations where the gas is in translational equilibrium due to the forms of the momentum and energy conservation equations that are used. However, the results presented in Section 5.3.1 show that it also produces good agreement with the macroscopic results from axisymmetric flow simulations where this translational equilibrium requirement is violated. This is because the length of the two regions in the flow field where the degree of translational nonequilibrium is the highest, in the shock and the boundary layer, are a relatively small portion of the overall length of the shock layer.

BIBLIOGRAPHY

BIBLIOGRAPHY

[1] Jones, W. L. and Cross, A. E., "Electrostatic Probe Measurements of Plasma Parameters for Two Reentry Flight Experiments at 25000 Feet Per Second," Tech. Rep. NASA Technical Note D-6617, Langley Research Center, 1972.

[2] Cornette, E. S., "Forebody Temperatures and Calorimeter Heating Rates Measured During Project FIRE II Reentry at 11.35 Kilometers Per Second," Tech. Rep. NASA TM X-1305, Langley Research Center, 1966.

[3] Jenniskens, P., "Observations of the STARDUST Sample Return Capsule Entry With a Slit-less Echelle Spectrograph," *AIAA Paper 2008-1210*, presented at the 46th AIAA Aerospace Sciences Meeting and Exhibit, Reno, NV, Jan. 2008.

[4] Boyd, I. D., Trumble, K., and Wright, M. J., "Nonequilibrium Particle and Continuum Analyses of Stardust Entry for Near-Continuum Conditions," *AIAA Paper 2007-4543*, presented at the 39th AIAA Thermophysics Conference, Miami, FL, June 2007.

[5] Vincenti, W. G. and Kruger, C. H., *Introduction to Physical Gas Dynamics*, Krieger Publishing Company, 1965.

[6] Krall, N. A. and Trivelpiece, A. W., *Principles of Plasma Physics*, McGraw-Hill Book Company, 1973.

[7] Bird, G. A., *Molecular Gas Dynamics and the Direct Simulation of Gas Flows*, Oxford Science Publications, 1994.

[8] Halliday, D., Resnick, R., and Walker, J., *Fundamentals of Physics*, John Wiley and Sons, Inc., 5th ed., 1997.

[9] Mitchner, M. and Kruger, C., *Partially Ionized Gases*, Wiley-Interscience, 1973.

[10] Wagner, W., "A Convergence Proof For Bird's Direct Simulation Monte Carlo Method For the Boltzmann Equation," *Journal of Statistical Physics*, Vol. 66, No. 3, 1992, pp. 1011–1044.

[11] Dietrich, S. and Boyd, I. D., "Scalar and Parallel Optimized Implementation of the Direct Simulation Monte Carlo Method," *Journal of Computational Physics*, Vol. 126, No. 0401, 1996, pp. 328–342.

[12] Haas, B. L. and Boyd, I. D., "Models for Direct Monte Carlo Simulation of Coupled Vibration-Dissociation," *Physics of Fluids*, Vol. 5, No. 2, 1993, pp. 478–489.

[13] Boyd, I. D., "Analysis of Rotational Nonequilibrium in Standing Shock Waves of Nitrogen," *AIAA Journal*, Vol. 28, No. 1, 1990, pp. 1997–1999.

[14] Vijayakumar, P., Sun, Q., and Boyd, I. D., "Vibrational-translational Energy Exchange Models for the Direct Simulation Monte Carlo Method," *Physics of Fluids*, Vol. 11, No. 8, 1999, pp. 2117–2126.

[15] Borgnakke, C. and Larsen, P. S., "Statistical Collision Model for Monte Carlo Simulation of Polyatomic Gas Mixture," *Journal of Computational Physics*, Vol. 18, 1975, pp. 405–420.

[16] Harvey, J. K. and Gallis, M. A., "Review of Code Validation Studies in High Speed Low Density Flows," *Journal of Spacecraft and Rockets*, Vol. 37, No. 1, 2000, pp. 8–20.

[17] Bird, G. A., "Monte Carlo Simulation in an Engineering Context," *Rarefied Gas Dynamics*, edited by S. S. Fisher, Vol. 74 of *Progress in Astronautics and Aeronautics*, AIAA, New York, 1981, pp. 239–255.

[18] Taylor, J. C., Carlson, A. B., and Hassan, H. A., "Monte Carlo Simulation of Radiating Re-entry Flows," *Journal of Thermophysics and Heat Transfer*, Vol. 8, No. 3, 1994, pp. 478–485.

[19] Ozawa, T., Nompelis, I., Levin, D. A., Barnhardt, M., and Candler, G. V., "DSMC-CFD Comparison of a High Altitude, Extreme-Mach Number Reentry Flow," *AIAA Paper 2008-1216*, presented at the 46th AIAA Aerospace Sciences Meeting and Exhibit, Reno, NV, Jan. 2008.

[20] Gallis, M. A., Prasad, R., and Harvey, J. K., "The Effect of Plasmas on the Aerodynamic Performance of Vehicles," *AIAA Paper 1998-2666*, presented at the 29th AIAA Plasmadynamics and Lasers Conference, Albuquerque, NM, June 1998.

[21] Jones, M. E., Lemons, D. S., Mason, R. J., Thomas, V. A., and Winkse, D., "A Grid Based Coulomb Collision Model for PIC Codes," *Journal of Computational Physics*, Vol. 123, No. 0014, 1996, pp. 169–181.

[22] Park, C., "Review of Chemical-Kinetic Problems of Future NASA Missions, I: Earth Entries," *Journal of Thermophysics and Heat Transfer*, Vol. 7, No. 3, 1993, pp. 385–398.

[23] Boyd, I. D., "Modeling of Associative Ionization Reactions in Hypersonic Rarefied Flows," *Physics of Fluids*, Vol. 19, 2007, pp. 096102.

[24] Boyd, I. D., Zhong, J., Levin, D. A., and Jenniskens, P., "Flow and Radiation Analysis for Stardust Reentry at High Altitude," *AIAA Paper 2008-1215*, presented at the 46th AIAA Aerospace Sciences Meeting and Exhibit, Reno, NV, Jan. 2008.

[25] Wilson, J., "Ionization Rate of Air Behind High-speed Shock Waves," *Physics of Fluids*, Vol. 9, No. 10, 1966, pp. 1913–1921.

[26] Ozawa, T., Zhong, J., Levin, D. A., and Boger, D., "Modeling of the Stardust Reentry Flows with Ionization in DSMC." *AIAA Paper 2007-0611*, presented at the 45th AIAA Aerospace Sciences Meeting and Exhibit, Reno, NV, Jan. 2007.

[27] Carlson, A. B. and Hassan, H. A., "Direct Simulation of Reentry Flows with Ionization," *Journal of Thermophysics and Heat Transfer*, Vol. 6, No. 3, 1992, pp. 401–404.

[28] Stone, E. J. and Zipf, E. C., "Excitation of Atomic Nitrogen by Electron Impact," *Journal of Chemical Physics*, Vol. 58, No. 10, 1973, pp. 4278–4284.

[29] Stone, E. J. and Zipf, E. C., "Electron Impact Excitation of the $^3S^0$ and $^5S^0$ States of Atomic Oxygen," *Journal of Chemical Physics*, Vol. 60, No. 11, 1974, pp. 4237–4243.

[30] Griem, H. R., *Plasma Spectroscopy*, McGraw-Hill, 1964.

[31] Lotz, W., "Electron-Impact Ionization Cross Sections and Ionization Rate Coefficients for Atoms and Ions from Hydrogen to Calcium," *Zeitschrift fur Physik*, Vol. 216, No. 3, 1968, pp. 241–247.

[32] Bird, G. A., "Low Density Aerothermodynamics," *AIAA Paper 1985-0994*, presented at the 20th AIAA Thermophysics and Heat Transfer Conference, Williamsburg, VA, June 1985.

[33] Bird, G. A., "Direct Simulation of Typical AOTV Entry Flows," *AIAA Paper 1986-1310*, presented at the 4th AIAA/ASME Joint Thermophysics and Heat Transfer Conference, Boston, MA, June 1986.

[34] Tonks, L. and Langmuir, I., "General Theory of a Plasma Arc," *Physical Review*, Vol. 34, No. 1, 1929, pp. 876–922.

[35] Gallis, M. A. and Harvey, J. K., "Ionization Reactions and Electric Fields in Plane Hypersonic Shock Waves," *Rarefied Gas Dynamics*, Vol. 160 of *Progress in Astronautics and Aeronautics*, AIAA, New York, 1992, pp. 234–244.

[36] Boyd, I. D., "Monte Carlo Simulation of Nonequilibrium Flow in a Low-power Hydrogen Arcjet," *Physics of Fluids*, Vol. 9, No. 10, 1997, pp. 4575–4584.

[37] Bartel, T. J. and Justiz, C. R., "DSMC Simulation of Ionized Rarefied Flows," *AIAA Paper 1993-3095*, presented at the 24th AIAA Fluid Dynamics Conference, Orlando, FL, July 1993.

[38] Justiz, C. R. and Dalton, C., "A Hybrid Flow Model for Charged and Neutral Particles Around Spacecraft in Low Earth Orbit," *AIAA Paper 1992-2935*, presented at the 27th AIAA Thermophysics Conference, Nashville, TN, July 1992.

[39] Bose, D. and Candler, G., "Thermal Rate Constants of the N_2+O $\rightarrow$ NO + N Reaction Using Ab Initio ^{3}A" and ^{3}A' Potential Energy Surfaces," *Journal of Chemical Physics*, Vol. 104, No. 8, 1996, pp. 2825–2833.

[40] Ralchenko, Y., Kramida, A. E., Reader, J., and NIST ASD Team, "NIST Atomic Spectra Database (version 3.1.5), [Online]," National Institute of Standards and Technology, Gaithersburg, MD. Available: http://physics.nist.gov/asd3 [2010 June 23].

[41] Sun, Q. and Boyd, I. D., "Evaluation of Macroscopic Properties in the Direct Simulation Monte Carlo Method," *Journal of Thermophysics and Heat Transfer*, Vol. 19, No. 3, 2005, pp. 329–335.

[42] Schulz, G. J., "Measurement of Excitation of N_2, CO and He by Electron Impact," *Physical Review*, Vol. 116, No. 5, 1959, pp. 1141–1147.

[43] Lee, J., "Electron-impact Vibrational Relaxation in High-temperature Nitrogen." *Journal of Thermophysics and Heat Transfer*, Vol. 7, No. 3, 1993, pp. 399–405.

[44] Whiting, E., Park, C., Liu, Y., Arnold, J. O., and Paterson, J. A., "NEQAIR96, Nonequilibrium and Equilibrium Radiative Transport and Spectra Program: User's Manual," Tech. Rep. NASA RP-1389, 1996.

[45] Taylor, J. C., Carlson, A. B., and Hassan, H. A., "Monte Carlo Simulation of Reentry Flows with Ionization," *AIAA Paper 1992-0483*, presented at the 30th AIAA Aerospace Sciences Meeting and Exhibit, Reno, NV, Jan. 1992.

[46] Mahan, B. H., "Microscopic Reversibility and Detailed Balance: an analysis," *Journal of Chemical Education*, Vol. 52, No. 5, 1975, pp. 299–302.

[47] Park, C., Jaffe, R. L., and Partridge, H., "Chemical-Kinetic Parameters of Hyperbolic Earth Entry," *Journal of Thermophysics and Heat Transfer*, Vol. 15, No. 1, 2001, pp. 76–90.

[48] Thomas, L. D. and Nesbet, R. K., "Low-energy Electron Scattering by Atomic Nitrogen," *Physical Review A*, Vol. 12, No. 6, 1975, pp. 2369–2377.

[49] Blaha, M. and Davis, J., "Elastic Scattering of Electrons by Oxygen and Nitrogen at Intermediate Energies," *Physical Review A*, Vol. 12, No. 6, 1975, pp. 2319–2324.

[50] Itikawa, Y. and Ichimura, A., "Cross Sections for Collisions of Electrons and Photons with Atomic Oxygen," *Journal of Physical Chemistry Reference Data*, Vol. 19, No. 3, 1990, pp. 637–651.

[51] Sunshine, G., Aubrey, B. B., and Bederson, B., "Absolute Measurements of Total Cross Sections for the Scattering of Low-Energy Electrons by Atomic and Molecular Oxygen," *Physical Review*, Vol. 154, No. 1, 1967, pp. 1–8.

[52] Itikawa, Y., "Cross Sections for Electron Collisions with Nitrogen Molecules," *Journal of Physical Chemistry Reference Data*, Vol. 35, No. 1, 2006, pp. 31–53.

[53] Cosby, P. C., "Electron Impact Dissociation of Nitrogen," *Journal of Chemical Physics*, Vol. 98, No. 12, 1993, pp. 9544 – 9553.

[54] Park, C., *Nonequilibrium Hypersonic Aerothermodynamics*, John Wiley and Sons, 1990.

[55] Bell, K. L., Gilbody, H. B., Hughes, J. G., Kingston, A. E., and Smith, F. J., "Recommended Data on the Electron Impact Ionization of Light Atoms and Ions," *Journal of Physical and Chemical Reference Data*, Vol. 12, No. 4, 1983, pp. 891–917.

[56] Nielson, S. E. and Dahler, J. S., "Endoergic Chemi-ionization in N-O Collisions," *Journal of Chemical Physics*, Vol. 71, No. 4, 1979, pp. 1910–1925.

[57] Padellec, A. L., "Partial Near Threshold Cross Sections for the Associative Ionization to form CO^+, NO^+ and O_2^+," *Physica Scripta*, Vol. 71, 2005, pp. 621–626.

[58] Ringer, G. and Gentry, W. R., "A Merged Molecular Beam Study of the Endoergic Associative Ionization Reaction $N(^2D)+O(^3P) \rightarrow NO^+ + e^-$," *Journal of Chemical Physics*, Vol. 71, No. 4, 1979, pp. 1902–1909.

[59] Vejby-Christensen, L., Kella, D., Pedersen, H. B., and Andersen, L. H., "Dissociative Recombination of NO^+," *Physical Review A*, Vol. 57, No. 5, 1998, pp. 3627–3634.

[60] Boyd, I. D., "Modeling Backward Chemical Rate Processes in the Direct Simulation Monte Carlo Method," *Physics of Fluids*, Vol. 19, 2007, Article 126103.

[61] Johnston, C. O., "Nonequilibrium Shock-Layer Radiative Heating for Earth and Titan Entry," *Ph.D. Dissertation, Virginia Tech*, November 2006.

[62] Hockney, R. W. and Eastwood, J. W., *Computer Simulation Using Particles*, McGraw-Hill Inc., 1981.

[63] Serikov, V. V. and Nanbu, K., "3D Monte Carlo Simulation of DC Glow Discharge for Plasma-assisted Materials Processing," *in Proceedings of the 20th International Symposium on Rarefied Gas Dynamics*, Beijing University Press, New York, 1996, pp. 829–834.

[64] Kawamura, E., Lichtenberg, A. J., Lieberman, M. A., and Verboncoeur, J. P., "Double Layer Formation in a Two-region Electronegative Plasma," *Physics of Plasmas*, Vol. 16, No. 1, 2009, pp. 122114.

[65] Hirsch, C., *Numerical Computation of Internal and External Flows*, Vol. 1, Elsevier, 2nd ed., 2007.

[66] J. D. Anderson, J., *Computational Fluid Dynamics: The basics with applications*, McGraw-Hill, 1995.

[67] Lieberman, M. A. and Litchenberg, A. J., *Principles of Plasma Discharges and Materials Processing*, Wiley-Interscience, 2005.

[68] Tomme, E. B., Annaratone, B. M., and Allen, J. E., "Damped Dust Oscillations as a Plasma Sheath Diagnostic," *Plasma Sources Science and Technology*, Vol. 9, No. 12, 2000, pp. 87–96.

[69] Tomme, E. B., Law, D. A., Annaratone, B. M., and Allen, J. E., "Parabolic Plasma Sheath Potentials and their Implications for the Charge of Levitated Dust Particles," *Physical Review Letters*, Vol. 85, No. 12, 2000, pp. 2518–2521.

[70] Farbar, E. D. and Boyd, I. D., "Simulation of FIRE II Reentry Flow Using the Direct Simulation Monte Carlo Method," *AIAA Paper 2008-4103*, presented at the 40th AIAA Thermophysics Conference, Seattle, WA, June 2008.

[71] Farbar, E. D. and Boyd, I. D., "Simulations of Reactions Involving Charged Particles in Hypersonic Rarefied Flows," *AIAA Paper 2009-0267*, presented at the 47th AIAA Aerospace Sciences Meeting, Orlando, FL, January 2009.

[72] Farbar, E. D. and Boyd, I. D., "Self-Consistent Simulation of the Electric Field in a Rarefied Hypersonic Shock Layer," *AIAA Paper 2009-4309*, presented at the 41st AIAA Thermophysics Conference, San Antonio, TX, June 2009.

[73] Farbar, E. D. and Boyd, I. D., "Modeling of the Electric Field in a Rarefied Hypersonic Flow," *AIAA Paper 2010-0635*, presented at the 48th AIAA Aerospace Sciences Meeting, Orlando, FL, January 2010.

[74] Farbar, E. D. and Boyd, I. D., "Simulation of Shock Layer Plasmas," *Paper 125*, presented at the 27th International Symposium on Rarefied Gas Dynamics, Monterey, CA, July 2010.

[75] Galitzine, C. and Boyd, I. D., "Simulation of the Interaction Between Two Counterflowing and Rarefied Jets," *Paper 129*, presented at the 27th International Rarefied Gas Dynamics Symposium, Monterey, CA, July 2010.

[76] Gimelshein, S. F., Levin, D. A., and Collins, R. J., "Modeling of Glow Radiation in the Rarefied Flow About an Orbiting Spacecraft," *Journal of Thermophysics and Heat Transfer*, Vol. 14, No. 4, 2000, pp. 471–479.

[77] Chaban, G., Jaffe, R., Schwenke, D. W., and Huo, W., "Dissociation Cross Sections and Rate Coefficients for Nitrogen from Accurate Theoretical Calculations," *AIAA Paper 2008-1209*, presented at the 46th AIAA Aerosciences Meeting and Exhibit, Reno, NV, January 2008.

[78] Norman, P. and Schwarztentruber, T., "Modeling Air-SiO_2 Surface Catalysis under Hypersonic Conditions with ReaxFF Molecular Dynamics," *AIAA Paper 2010-4320*, presented at the 10th AIAA/ASME Joint Thermophysics and Heat Transfer Conference, Chicago, IL, June 2010.

ABSTRACT

KINETIC SIMULATION OF RAREFIED AND WEAKLY IONIZED HYPERSONIC FLOW FIELDS

by

Erin D. Farbar

Chair: Iain D. Boyd

When a vehicle enters the Earth's atmosphere at the very large velocities associated with Lunar and Mars return, a strong bow shock is formed in front of the vehicle. The shock heats the air to very high temperatures, causing collisions that are sufficiently energetic to produce ionized particles. As a result, a weakly ionized plasma is formed in the region between the bow shock and the vehicle surface. The presence of this plasma impedes the transport of radio frequency waves to the vehicle, causing the phenomenon known as "communications black out". The plasma also interacts with the neutral particles in the flow field, and contributes to the heat flux at the vehicle surface. Since it is difficult to characterize these flow fields using flight or ground based experiments, computational tools play an important role in the design of reentry vehicles. It is important to include the physical phenomena associated with the presence of the plasma in the computational analysis of the flow fields about these vehicles.

Physical models for the plasma phenomena are investigated using a state of the art, Direct Simulation Monte Carlo (DSMC) code. Models for collisions between charged particles, plasma chemistry, and the self-induced electric field that currently exist in the literature are implemented. Using these baseline models, steady state flow field solutions are computed for the FIRE II reentry vehicle at two different trajectory points.

The accuracy of each baseline plasma model is assessed in a systematic fashion, using one flight condition of the FIRE II vehicle as the test case. Experimental collision cross section data is implemented to model collisions of electrons with neutral particles. Theoretical and experimental reaction cross section data are implemented to model chemical reactions that involve electron impact, and an associative ionization reaction. One-dimensional Particle-In-Cell (PIC) routines are developed and coupled to the DSMC code, to assess the limitations of the baseline electric field model. Interpretation of the DSMC-PIC results leads to the development of an improved electric field model that does not require the substantial computational resources needed to obtain DSMC-PIC solutions.